UiT The Arctic University of Norway

Faculty of Science and Technology
Department of Geosciences

Snowdrift Analysis using FlowCapt FC4 and LiDAR Data at Fv. 53 Tyin-Årdal

Mikael Jay Strand Ovesen

Master's Thesis in Geosciences, GEO-3900, May 2024

Abstract

The wind is essential in distribution of snow and the degree of avalanche danger. There are a lot of uncertainties regarding quantification of wind-transported snow, which is of importance for local avalanche warning and Remote Avalanche Control Systems (RACS) - which is conducted by Skred AS along Fv. 53 (County Road 53) Tyin-Årdal. A snowdrift sensor, FlowCapt 4 (FC4), is installed along this weather-exposed mountain road to function as an additional tool in the decision-making of the avalanche risk assessment - helping determine snowdrift occurrences. In addition, the sensor can provide a basis in forming an empirical relationship between measured snowdrift and snowdrift deposition in the Potential Release Areas (PRAs) for avalanches towards the road.

The objective of this study is to look into a method uncovering the correlation between measured snowdrift from the FC4, weather data, and deposited snowdrift in the PRAs - measured from consecutive LiDAR-scans. Fieldwork on the snow cover was conducted to monitor available snow for transport.

This study proposes an empirical relationship between measured snowdrift from the FC4 and mean snow surface change measured from LiDAR-scans, and recommends building on this relationship with more measurements with the newly installed snow depth sensor and verifications with fracture heights from future avalanche controls. Snowfall during snowdrift events were not found to have a significant role in determining snow depth deposition as corrections weakened the correlational trend.

This study underlines the importance of keeping measurements simple to avoid additional layers of uncertainty when building an empirical relationship. It might be sufficient with point-observations on the measured snowdrift and snow depth deposition given that the locations are representative and chosen for the purpose of collecting conservative data. Focusing on keeping the uncertainties down at the expense of quantitative accuracy can be considered essential in the application of FC4-data, as its role will continue to be an additional tool in the risk assessment, with the role of reducing the uncertainties regarding snowdrift occurences.

D

Preface

This thesis concludes my Master of Science degree in Geosciences at the Department of Geosciences at UiT (The Arctic University of Norway). The work has been conducted in collaboration with Skred AS - whom I would like to thank for being my external supervisor and giving me the opportunity to work on a very interesting issue in local avalanche warning.

Hallvard, thank you for giving me good professional input and guidance. Louise, thank you for the good feedback, follow-up and arranging logistics around the master's thesis despite the fact that there has been a lot of logistics with a newborn. Chris, thank you for your expertise, good guidance and feedback - both in the field and in the office. Jens, thank you for letting me stay at your second home at Tyinkrysset and for the helpfulness and availability. Emil, thank you for your invaluable contribution with LiDAR-scans to this Master's Thesis, and your time spent driving between Bergen and Tyin for most of them. Vilde and Fabrice, thank you for being my field assistants and good friends during fieldwork. Pål, thank you for letting me participate in two avalanche controls, what an experience.

Contents

List of Figures

List of Tables

List of Abbreviations

DEM Digital Elevation Model

DF Decomposing and Fragmented precipitation particles

DH Depth Hoar

DRR Daily Rain Rate

EAWS European Avalanche Warning Services

ECT Extended Compression Test

FC Faceted Crystals

FC4 FlowCapt 4

FSW Fresh Snow Water Equivalent

GEOSFAIR Geohazard Survey from Air

GIS Geographic Information System

GND Ground

GPS Global Positioning System

IF Ice Formation

LİDAR Light Detection and Ranging

LWC Liquid Water Content

MET Norwegian Meteorological Institute

MF Melt Forms

NGI The Norwegian Geotechnical Institute

NPRA Norwegian Public Road Administration

NVE The Norwegian Water Resources and Energy Directorate

PP Precipitation Particles

PRA Potential Release Area

PWL Persistent Weak Layer

RACS Remote Avalanche Control System

RADAR Radio Detection and Ranging

RG Rounded Grains

RPAS Remotely Piloted Aircraft System

RTK Real-Time Kinematics

SfM Structure-from-Motion

SH Surface Hoar

SWE Snow Water Equivalent

UAS Unmanned Aircraft System

UAV Unmanned Aerial Vehicle

1 Introduction

Snow avalanches, hereafter referred to as avalanches, are a natural consequence of the ever-changing and variable snow cover in steep mountainous regions. Avalanches pose a significant risk towards humans and infrastructure, and is the cause of the majority of winter-related fatalities and infrastructure damage globally [Schweizer et al., 2003; Boyd et al., 2009; McClung, 2016; Jekich et al., 2016].

Wind-transport of snow, hereafter referred to as snowdrift, is a key factor in triggering of snow avalanches [Tabler et al., 1990], especially in high mountain areas above the tree line. The wind can transport significant amounts of snow into slopes, increasing the avalanche risk locally, and often leads to road closures as a preventative measure to secure the road. Adapting to snowdrift is a resource- and cost-intensive process in the operation of winter roads [Norem, 1974, 1975a,b; Tabler et al., 1990; Tabler, 1994, 2003; Thordarson, 2002; Margreth, 2007; Statens Vegvesen, 2014a].

Skred AS has carried out site-specific local avalanche warning and operates a Remote Avalanche Control System (RACS) on parts of the Fv. (County Road) 53 Tyin-Årdal on behalf of Innlandet County since the winter season 2021/22 [Skred AS, 2024a]. The avalanche control is carried out using blasting towers supplied by Wyssen [Wyssen Norge AS, 2023]. Critical avalanche sizes that can reach the roads and surrounding cabins have been assessed using numerical modeling calibrated based on earlier avalanche events [Skred AS, 2022].

Skred AS has, in collaboration with the Norwegian Public Road Administration (NPRA) and Innlandet County, installed a snowdrift sensor - FlowCapt 4 (FC4) - along the County Road 53 Tyin-Årdal during winter season 2022/23 as a part of a Research & Development project. The purpose of the project was to gain practical experience with installation and operation throughout the winter season, and to see how measured snowdrift data can contribute to a more precise local avalanche warning and a more cost-effective road operation.

The experiences from the first winter season (2022-2023) were that the sensor gave the forecasting group useful information about the duration of periods of snowdrift - helping to qualitatively assess the total amount of snow deposition from snowdrift. Skred AS' analysis on the first year of usage concluded with that a more in-depth analysis of the snowdrift data as well as installation of snow depth gauges could make it possible to establish threshold values for critical amounts of snowdrift - the amounts that, when deposited in Potential Release Areas (PRAs), could initiate avalanches large enough to affect the infrastructure of focus.

For this master's thesis, Light Detection and Ranging (LiDAR)-data from field-work was derived, giving a foundation for analysis looking into patterns in the relationship between weather data, measured snowdrift from the FC4-sensor, and the measured snow deposition from snowdrift by LiDAR-scans. Snow avalanche forecasting is largely about reducing uncertainty linked to risk management, and a motivation for this study is to contribute to reducing this uncertainty, first and foremost at this specific area.

2

Theoretical Background

2.1 Snow Physics

This section covers the theory behind snow physics, snow metamorphism, snow cover development, and the development of avalanche problems.

2.1.1 Snow Cover and Snow Metamorphism

A snow crystal forms when an extremely cold water droplet freezes on to a pollen or dust particle suspended in the atmosphere [Mason, 1961]. During descent towards the Earth's surface, additional water vapor freezes onto this core crystal, gradually augmenting its structure to include branches – the six arms of a fully formed snow flake [Libbrecht, 2005, 2007].

When there is little wind, snow flakes fall calmly - as individual flakes when it is cold, or in bundles when temperature is closer to 0°C, due to the increased humidity [N. Sato & Kikuchi, 1985]. Thus, in cold and still weather the snow becomes loose and light. In such conditions, the snow can contain up to 99% air and only 1% ice of which the crystals are made up [Lied & Kristensen, 2003]. The study of Judson & Doesken [2000] showed that the average density of snow were 72 - 103 kg/m^3 based on a four year observation from six measurement sites in the mountains of Colorado and Wyoming. When snow is 100 kg/m^3, it is 10% of the density of water - which has a density of 1000 kg /m^3 at 4°C [Bigg, 1967; Tanaka et al., 2001].

The most common way to measure precipitation is in mm of water. When it is stated that a certain number of mm of precipitation has come as snow, the number refers to the snow in a melted state - the Snow Water Equivalent (SWE), or the Fresh Snow Water Equivalent (FSW). For this study, the average density of fresh snow is set to be 100 kg/m^3 - which means that 1 cm of snow will correspond to 1 mm of precipitation/Fresh Snow Water Equivalent (FSW).

Snow Metamorphism

Snow metamorphism refers to the process by which snow undergoes physical and chemical changes over time due to various factors such as temperature, pressure, and humidity [Sommerfeld & LaChapelle, 1970; Colbeck, 1982, 1983, 1997, 1998; Lied & Kristensen, 2003; McClung & Schaerer, 2006]. It involves the transformation of snow crystals and the reorganization of the snowpack structure.

The snow cover is built up in layers. A layer of snow is a horizontal area in the snow cover of similar grain shape (Snow types summarized in Tab. 2.1.1) and hardness. For every snowfall at least one new snow layer forms. If wind and temperature conditions changes significantly during snowfall, several layers can occur in a short time. A typical example is low wind at the start of a precipitation period providing loose fresh snow, that gets followed by increased wind which causes rounding due to erosion of snow crystals. This often forms a weak layer of loose **Precipitation Particles (PP)** under an overlying layer of packed snow; a slab.

Table 2.1.1: Main classes (and some subclasses used in this study) of snow types. Extract from The International classification for seasonal snow on the ground [Fierz et al., 2009].

Code & Symbol	Underclass	Shape
PP, +	Precipitation Particles	
DF, /	Decomposing and Fragmented precipitation particles	
RG, ●	Rounded Grains	
FC, □	Faceted Crystals	
FCxr, ⍓	Rounding faceted particles	Faceted crystals with rounded edges and corners
DH, ∧	Depth Hoar	
SH, ∨	Surface Hoar	
MF, ◯	Melt Forms	
MFcl, ⚇	Clustered rounded grains	Merged rounded grains united by large ice-to-ice bonds; Free water in cavities
MFpc, ⚘	Rounded Polycrystals	Single crystals frozen together to massive polycrystals; may be either wet or frozen
MFpc, ◎	Melt-freeze crust	Cluster of recognizable melt-frozen polycrystals
IF, ▬	Ice Formation	

Destructive Metamorphism The snow continues to transform when on the ground, and is the result of thermodynamic instability [Powers et al., 1985a; Colbeck, 1980, 1998]. Snow is always relative close to its melting point, and can be considered a "warm" and dynamic material. When a hexagonal snow crystal settles on the ground, it begins to restructure the water molecules to get the best possible relationship between surface and volume turning into an ice ball [Colbeck, 1998], as seen in Figure 2.1.1. The settlement is fastest in the early phase as well as when the temperature is close to 0°C [Colbeck, 1997, 1998]. In cold weather, the snow cover will stay light and loose for a longer time.

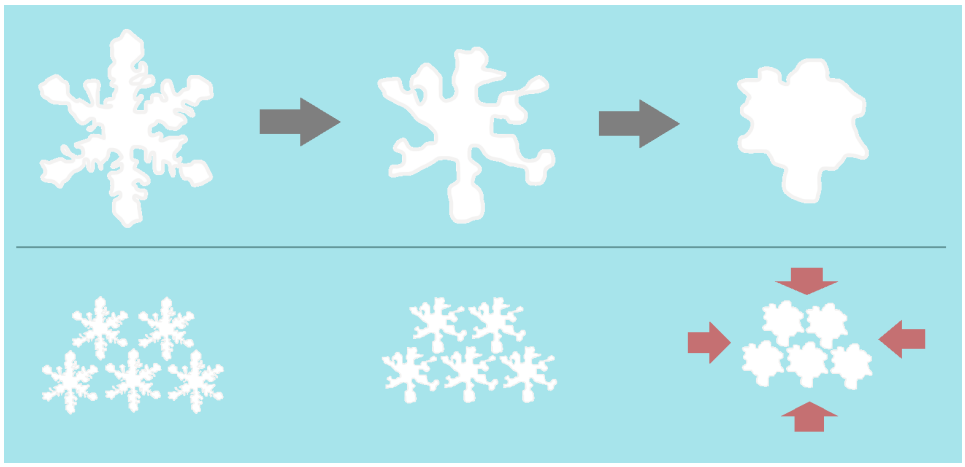

Figure 2.1.1: Schematic sketch of evaporation and condensation of water vapor towards concave areas of less saturation pressure, and creation of inter-grain ice connections. This increases snowpack density. Figure by author.

Decomposing and Fragmented precipitation particles (DF) and **Rounded Grains (RG)** are formed through destructive metamorphism. The water molecules in the crystal restructures itself breaking down complex structures to gain the smallest possible surface [Colbeck, 1998]. This leads to smaller rounded grains with several bonds between each other per volume unit. The water molecules move from areas on the snow crystal with high water vapor pressure (convex forms) to areas with lower water vapor pressure (concave shapes) [Klever, 1985; Powers et al., 1985a,b; Colbeck, 1993]. The speed on the restructuring is dependent on temperature. At temperatures close to 0°C it may take a few hours, while at extremely cold temperatures it takes days [Van Herwijnen & Miller, 2013].

Upon contact between crystals, they start to "grow together". This is a process called sintering [Colbeck, 1998], where water molecules migrate towards the contact points between the crystals. Sintering contributes to good bonds in the snow, thus increasing the stability, and is the process that forms slabs [Ramseier & Keeler, 1966; Colbeck, 1997, 1998; Van Herwijnen & Miller, 2013].

Constructive Metamorphism **Faceted Crystals (FC)** and its extreme form; **Depth Hoar (DH)** form through constructive metamorphism. This is due to a difference in vapor pressure (pressure gradient). The difference in pressure are caused by variations in temperature, shape and size of the crystals (Fig. 2.1.2).

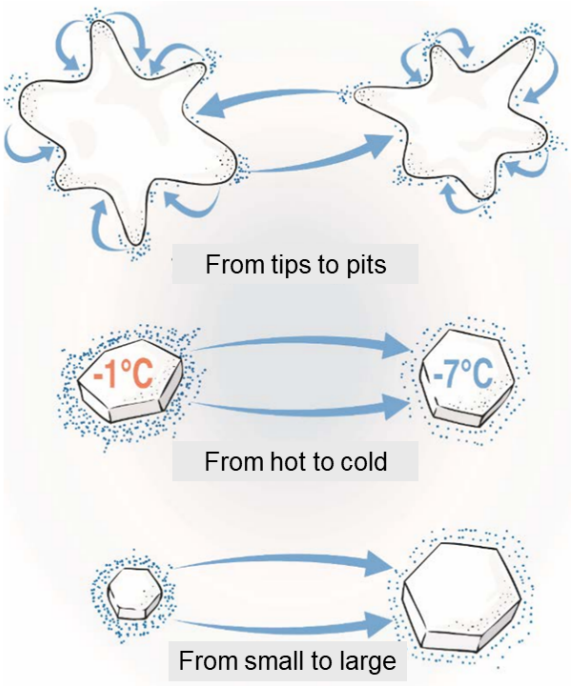

Figure 2.1.2: The water molecules move from areas of higher pressure to areas of lower pressure. Edited figure from NVE [2020b].

In general, the movement of water vapor happens through diffusion and convection. Diffusion happens when water vapor molecules moves away from areas with a high water vapor content to places with less water vapor [Colbeck, 1993]. Movement of water vapor can also be initiated by convection in that the warm air flows from below and upwards in the snow cover, especially when the snow cover has high porosity [Powers et al., 1985a,b; Klever, 1985].

Water molecules prefer to bond to places with the most neighboring molecules, such as on edges and corners rather than on smoothed round surfaces [Colbeck, 1998]. Over time, during high temperature gradients (>10°C/m [Lied & Kristensen, 2003; McClung & Schaerer, 2006; NVE, 2020b]) - this causes movement of vapor pressure upwards in the snow cover - snow crystals will grow straight surfaces and sharp edges on the underside of the crystal, while sublimation creates a round shape on the upper part of the grains (Fig. 2.1.3) [Colbeck, 1980].

On such faceted crystals one can then see the crystals sparkle when held up to the light. Faceted crystals can grow up to 2-3mm, and under circumstances of greater temperature gradients and porosity, the snow crystals can grow even larger and form depth hoar crystals with sizes up to 4-8mm [Lied & Kristensen, 2003; McClung & Schaerer, 2006], these are recognized by hexagonal cross-

section and striped surface.

Under circumstances where constructive metamorphism dominates over destructive metamorphism, such as under high pressure- and temperature gradients (examples of weather circumstances are visualized in Figures 2.1.4 and 2.1.5), crystals growth cause contact points to disappear, and the number of bindings per volume unit is reduced. This can cause the shear strength of the layer to weaken, and increases the probability of a fracture under load [Lied, 1998; Lied & Kristensen, 2003].

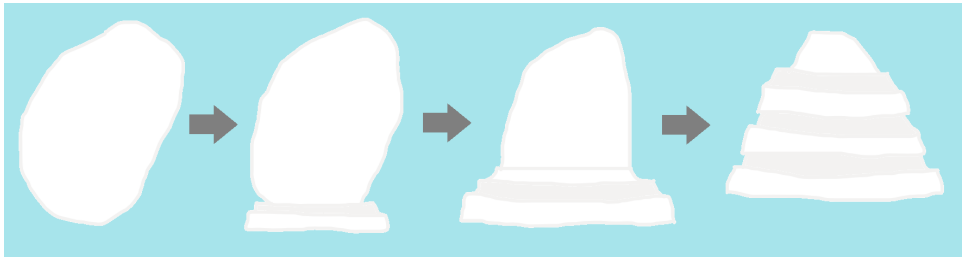

Figure 2.1.3: Schematic sketch of the growth of a faceted crystal, where water vapor condensates from below. A faceted crystal created from atmospheric moisture from above is called surface hoar. Figure by author.

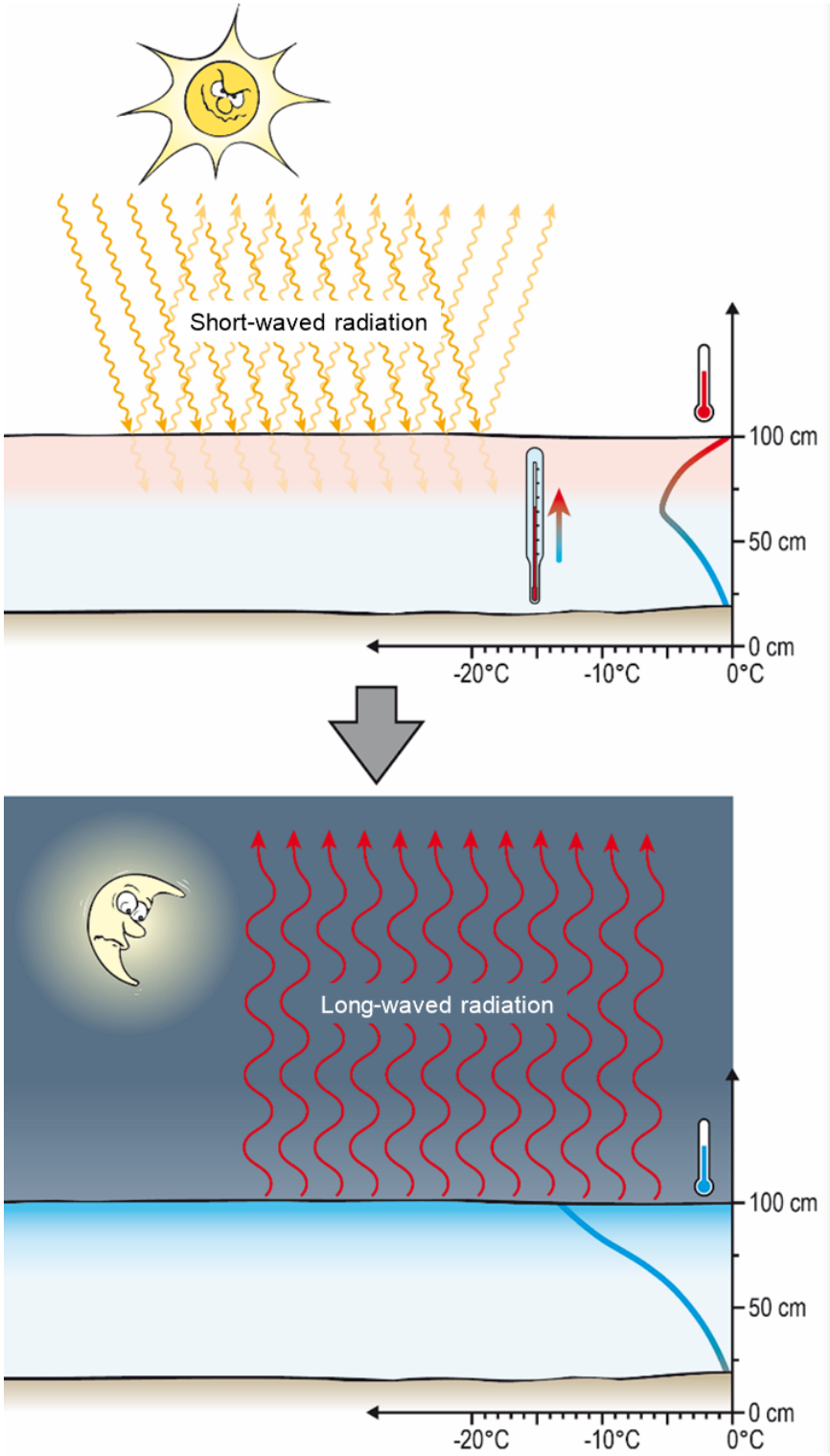

Figure 2.1.4: Temperature fluctuations throughout the day can form a high temperature gradient (>10°C/m) near the snow surface. This can lead to rapid growth of faceted grains [Lied & Kristensen, 2003; McClung & Schaerer, 2006; NVE, 2020b]. Edited figure from NVE [2020b].

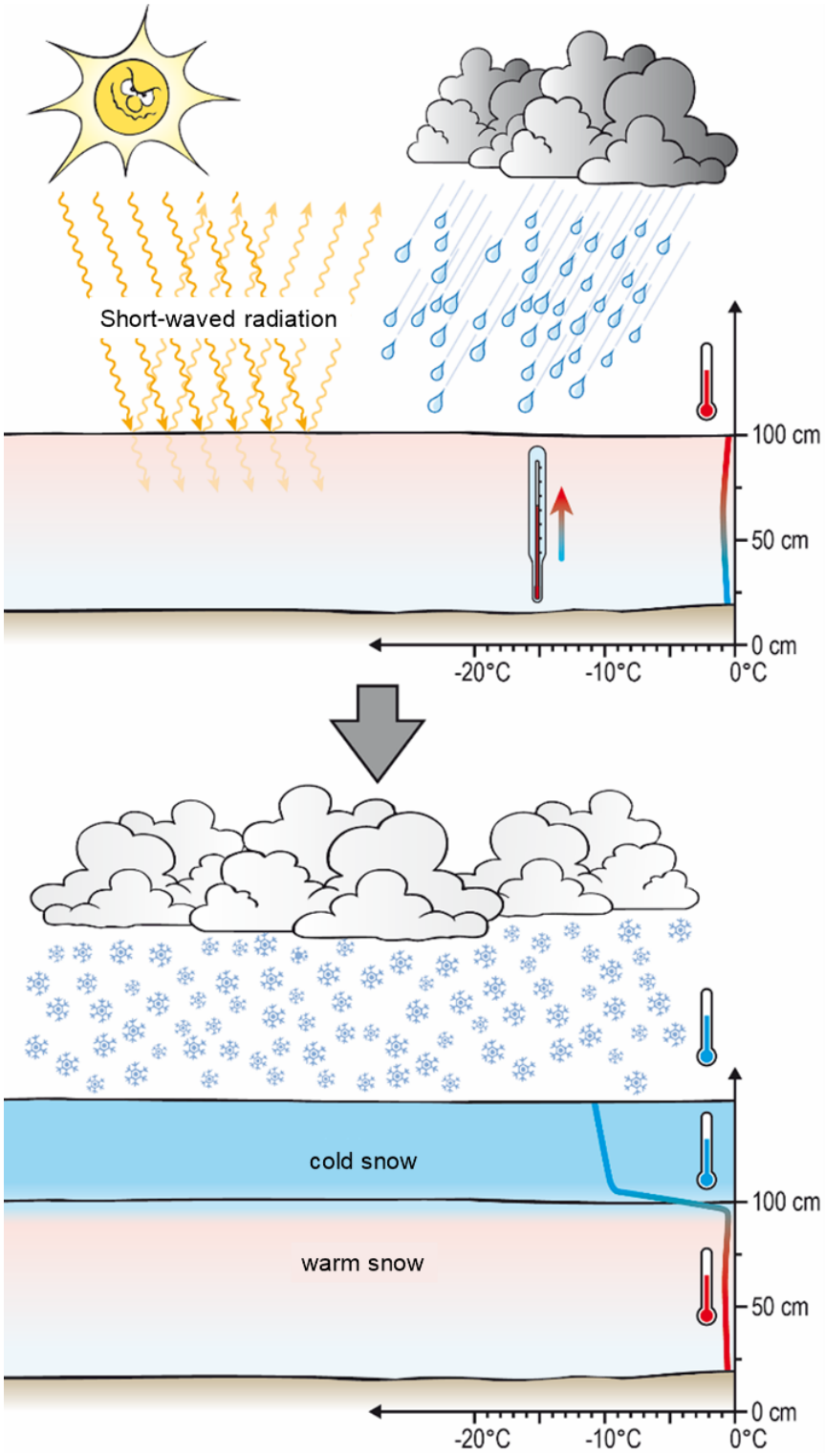

Figure 2.1.5: Cold fresh snow on a damp snow surface facilitates rapid growth of faceted grains, due to the available moisture [Klever, 1985; Powers et al., 1985a,b; Colbeck, 1993] and high temperature gradients [Lied & Kristensen, 2003; McClung & Schaerer, 2006; NVE, 2020b]. Edited figure from NVE [2020b].

When the temperature gradient is low over a long period of time, then faceted grains can break down into **Rounding Faceted Particles (FCxr)** and subsequently into rounded grains (this grain will be much larger and glossier than normal rounded grains) [Lied & Kristensen, 2003; McClung & Schaerer, 2006]. Figure 2.1.7 in the next subsection shows a schematic overview of snow metamorphism and the direction of metamorphism each snow crystal can transform into, through both constructive, destructive, and melt metamorphism.

Surface Hoar (SH) is another type of crystal formed by constructive metamorphism when there is a large difference between the temperature of the air compared to the snow surface. Such conditions are often under cold, clear nights with light wind to add moisture [Lang et al., 1984; Lied & Kristensen, 2003].The snow surface then loses much of its heat through long-wave radiation which escapes due to clear skies [Swinbank, 1963]. The snow surface therefore cools faster than the air, and when water vapor hits the cold snow surface, it condensates and crystals on the surface grow [Lang et al., 1984]. These crystals are feather-shaped (Fig. 2.1.6).

Figure 2.1.6: Surface hoar. Picture: Rustad, B. / The Norwegian Water Resources and Energy Directorate (NVE).

Melt Metamorhpism The snow can be heated through air temperature, wind, sun radiation or rain. When the temperature in the snow cover reaches o°C, the energy is used to melt the snow crystals and produce water in the snow cover instead of increasing the temperature further [Colbeck, 1980]. Under these circumstances, **Melt Forms (MF)** are created.

Small amounts of water form a thin film around the snow grains due to cohesion. When the water amount increases, the pore space fills with water, and will in the end begin to flow through the snow cover, melting away the bonds between each individual snow grain [Colbeck, 1980, 1997, 1998]. If the snowpack refreezes, it can form very strong bonds (ice bridges) between the crystals. **Melt-freeze crust (MFpc)** and **Ice Formation (IF)** are typical signs that it has occured melt-freeze processes in the snowpack [Lied & Kristensen, 2003; McClung & Schaerer, 2006].

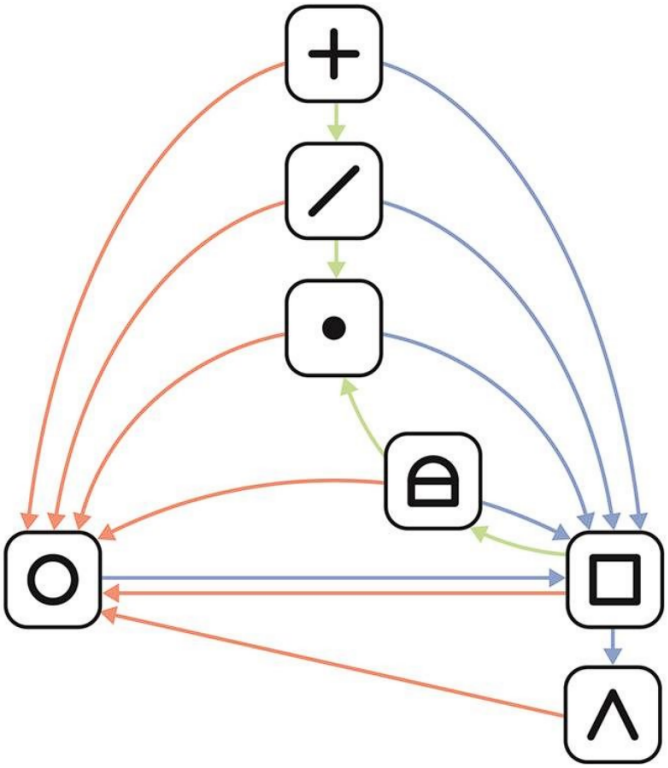

Figure 2.1.7: Schematic overview of the three types of snow metamorphism and their possible chronological orders. Constructive metamorphism marked with blue arrows, destructive metamorphism marked with green arrows, melt metamorphism marked with orange arrows. Snow type symbols are earlier summarized in Table 2.1.1. Figure from NVE [2020b].

The Influence of Temperature Gradient The water molecules move the quickest under mild conditions because of high temperature gradients [Colbeck, 1997, 1998]. Snow metamorphism processes will therefore be quicker in a snow cover at -2°C rather than one at -20°C - provided that the temperature gradient is equal. If the temperature gradient is small - less than 10°C/m - then the destructive metamorphism will dominate, and the crystals get rounded [NVE, 2020b]. This will happen faster at areas closer to 0°C than areas at -20°C. Therefore, a weak layer of fresh snow can be very unstable for longer

when it is very cold compared to under milder temperatures [Van Herwijnen & Miller, 2013]. A rule of thumb is that if the temperature gradient is greater than 10°C/m, then constructive metamorphism dominates [Lied & Kristensen, 2003; McClung & Schaerer, 2006; NVE, 2020b].

Both the snowfall intensity, the temperature during the snowfall, and the wind speed- and direction determine how the snow cover builds up. Because these conditions vary with each snowfall and because the snow changes between each snowfall, the snow cover is often composed of layers with different structures. Some layers are thick and homogeneous as a result of long-term snowfall with fairly constant wind- and temperature conditions. In other parts there can be thin layers of different hardness, because the wind speed has varied during the snowfall [Lied & Kristensen, 2003].

2.1.2 Development of Avalanche Problems

Where Does Avalanches Occur?

Terrain slope is the single factor that has the greatest significance for the degree of avalanche danger [Lied & Kristensen, 2003]. The rule of thumb is that slopes between 30-60° give rise to avalanches [Lied, 1976; Schweizer & Jamieson, 2001; Schweizer et al., 2003], as presented in Figure 2.1.8. The roughness of the slope must be small enough such that the unevenness in the release area is covered by snow. When the slope includes forest or other unevenness in the area, the snow will be easier kept in place and the risk of avalanches is reduced [Issler et al., 2023]. Terrain slopes down towards 30° usually cause large, but rare avalanches, whereas slopes over 45° cause more frequent avalanches, and are therefore usually smaller [Lied & Kristensen, 2003; McClung & Schaerer, 2006].

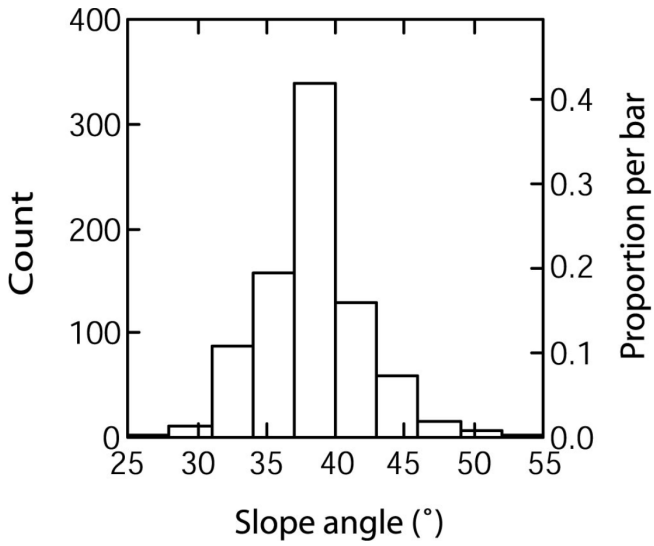

Figure 2.1.8: Slope angles in the starting zone of human-triggered avalanches (N = 809). The mean thickness of the sampled slabs was 0.49 ± 0.22 m. Data and figure from [Schweizer & Jamieson, 2001; Schweizer et al., 2003]

Stress Conditions

The stress conditions of a snow cover are very complex and cannot be quantitatively measured, and can therefore only be understood based on simplifications. In horizontal terrain, the snow will undergo a vertical settling movement [Bergen, 1978]. This effect is most prominent in new snow with temperatures close to 0°C [Conway & Raymond, 1993]. In inclined terrain, the component of gravity parallel to the slope will cause a slow creeping movement and the snow will deform plastically [Mellor, 1974; Larsen, 1998]. The movement is greatest near the snow surface and decreases towards the ground. Varying terrain slope, ground roughness, and snow depths lead to varying creeping rates due to gliding. For this reason, the stress conditions of the snow cover will vary from place to place, and create zones of tensile, shear and compressive stresses [Mellor, 1974; Lied, 1976; Larsen, 1998; Margreth, 2007].

Avalanche Types

Avalanches are usually divided into two main types [Lied & Kristensen, 2003; McClung & Schaerer, 2006]:

- Loose snow avalanches: Starts at a point where little snow is initially put in motion. Spreads slowly while the volume gradually increases. Occurs

most often in either loose fresh snow or in wet snow. The connections (cohesion) between the crystals are small, and thus needs little influence to initiate. Often triggered during or shortly after intense snowfall in steep terrain.

- Slab avalanches: Consists of larger or smaller slabs where the snow as a unit slides out. It is characterized by a slab gliding along a weaker layer down in the snowpack or along the ground (Fig. 2.1.9). Slab avalanches are the largest and the most dangerous, and are mainly the type that cause the most damage to people, nature, and infrastructure [Schweizer et al., 2003; Lied & Kristensen, 2003; Boyd et al., 2009; McClung, 2016; Jekich et al., 2016].

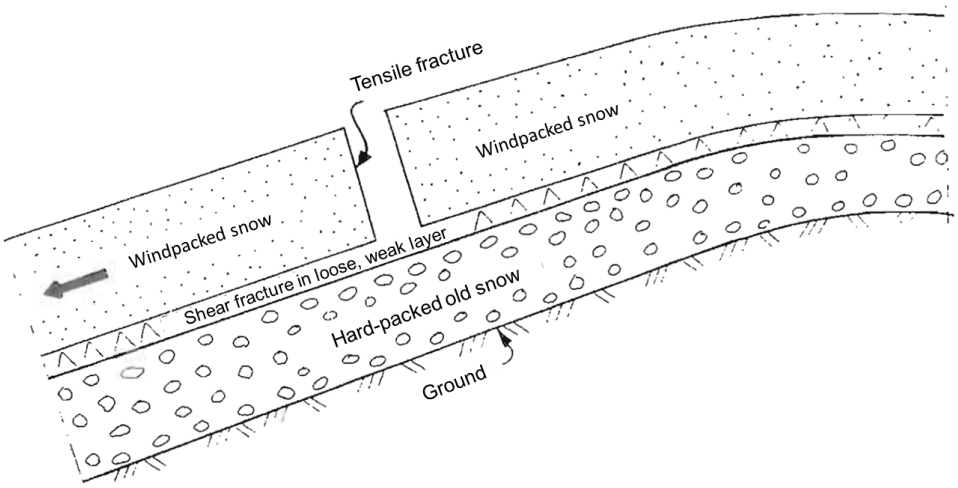

Figure 2.1.9: Components of a slab avalanche. Edited figure from Lied [1976]

Weak Snow Layers

A weak snow layer is the most important snow cover property in terms of avalanche issues - mainly related to slab avalanches. They function as horizontal layers that are prone to collapsing due to the weak structure and bonding between the snow crystals. If overlaid by snow, this gives a basis for avalanches. In a single layer of snow, properties such as strength and thickness may vary from place to place, and thereby the stability and possibility of avalanches can vary within short distances [Lied & Kristensen, 2003]. Some types of weak layers that give a temporarily increased risk of avalanches include:

- Buried weak layer of new snow: When fallen new snow crystals retain

their structure in whole or partially, and are additionally buried by more densely packed snow, e.g. due to wind transport, it can act as a weak layer because the bonds between the snow crystals are weak, and can collapse and act as a gliding layer for the overlying more densely packed snow. The avalanche danger is relevant typically during snowfall and up to a few days after. Stabilizes often fast, depending on temperature and radiation [Lied & Kristensen, 2003; Varsom, 2024].

- Poor bonding between crust and overlying snow: A hard crust will act as a gliding surface for the overlying snow as the new snow crystals do not bond to the older snowpack due to it's hardness.

- Persistent Weak Layer (PWL): These layers have a persistent effect on the avalanche hazard as they do not disappear either until the snow cover becomes isothermal(equal temperature throughout the snow cover), is affected by rainfall, or compacted mechanically [Lied & Kristensen, 2003]. Persistent Weak Layer (PWL)s can consist of either surface hoar, faceted grains, or depth hoar.

Avalanche Motion

For the rest of this study, slab avalanches are of focus, because of relevance to the study area. When a slab avalanche releases, an almost spontaneous fracture occurs over a larger area initiating movement of significant amounts of snow [Schweizer, 1999]. Knowledge of the actual avalanche movement, i.e. what speeds, range, and pressure effects an avalanche can achieve is important to assess the degree of avalanche danger and is helpful in designing of safety measures and other constructions that must withstand the pressure from avalanches [Norem, 1975b; Margreth, 2007; Lied & Kristensen, 2003; Naaim et al., 2008; Statens Vegvesen, 2014b; Eckert et al., 2012].

A moving avalanche is a complicated and complex process. When a slab avalanche initiates, the movement is first characterized by sliding. It eventually breaks up into smaller or larger blocks depending on the snow hardness [Schweizer, 1999; McClung & Schaerer, 2006]. In smaller avalanches where the runout length is below 10-20m, the sliding movement is dominant - resulting in smaller or larger angular blocks in the avalanche deposits [Lied & Kristensen, 2003]. In larger avalanches where the masses move further down, the speed increases rapidly and the snow becomes more and more pulverized with particles rolling, sliding, and jumping [Lied & Kristensen, 2003; McClung & Schaerer, 2006; Bartelt et al., 2016].

When the speed reaches a certain speed, the core of the avalanche starts to expand, taking in air that mixes with the particles, and provides for intermittent powder snow blowouts due to frequent phases of compression [Bartelt et al., 2016]. This makes for the familiar plume structures with lobe (blow-out) and cleft (no blow-out) features, as seen in Figure 2.1.10. The powder cloud moves ahead of the avalanche core because it experiences less drag [Hopfinger & Tochon-Danguy, 1977; Bartelt et al., 2016; Ito et al., 2017].

Based on this complex form of movement, the avalanche behaves partly as a solid substance (avalanche core), partly as a liquid flow, and partly as a gas in motion [Ancey, 2001; McClung & Schaerer, 2006], as showed in a schematic sketch in Figure 2.1.11. This kind of motion is most relevant for dry avalanches. Wet avalanches will normally last longer in the sliding phase but retards faster due to higher cohesion in the avalanche mass [Upadhyay et al., 2010; Sovilla, Kern, & Schaer, 2010; Vera Valero et al., 2018].

Figure 2.1.10: The powder cloud of a mixed flowing/powder snow avalanche released from avalanche tower Langø 21.02.23. Picture taken by Falkeblikk AS, as commissioned by NVE.

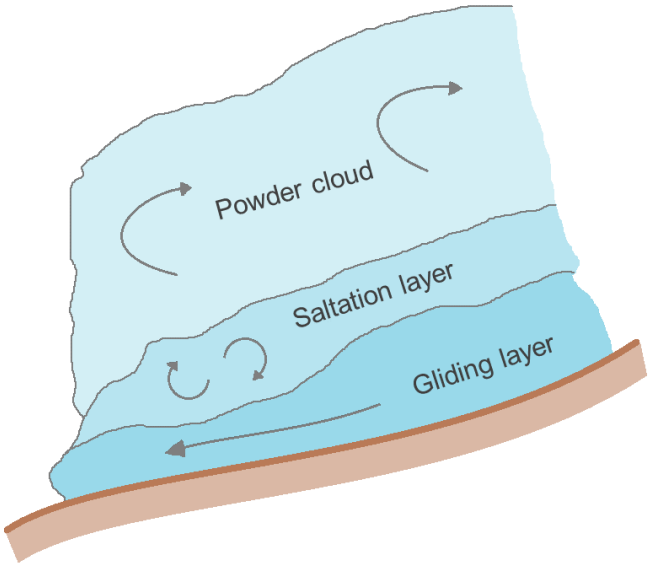

Figure 2.1.11: The general components of an avalanche in motion. The gliding layer (avalanche core) consists of the heaviest avalanche debris in a layer up to 3-5 m thickness. The saltation layer includes particles that jump and bounce, in a layer of few meters thickness - depending on the speed and avalanche content. The powder cloud is the turbulent flow of the avalanche debris suspended in air. Figure by author.

Several theoretical models have been developed to describe the movement of avalanches. Through many years of research, dynamic and statistical models have been developed to sufficiently describe the movement of an avalanche, although they do not explain the exact physical phenomenon to detail. With careful use, approximations can be calculated on the travel speeds, pressure, and the runout distances.

The RAMMS::Ext model [Christen et al., 2010] simulates both the avalanche core and the powder cloud. The core is physically treated as a gravitationally driven granular shear flow, and the powder cloud is modeled as an inertial turbulent suspension of ice-dust. The RAMMS model divides the core and cloud into two separate but overlapping flow layers. The densities and speeds of the avalanche core and powder cloud vary in the streamwise direction.

It is normal that the powder cloud and avalanche debris flow together towards the bottom of the valley. During deceleration in the transition to flatter terrain, the avalanche core brakes first [Hopfinger & Tochon-Danguy, 1977; Ito et al., 2017]. The powder cloud can continue to flow over long stretches as it has no friction against the ground, but will stop because it will no longer be propelled by the avalanche core [Bartelt et al., 2016].

The European Avalanche Warning Services [EAWS, 2024] have classified the avalanche sizes and given them definitions as summarized in Table 2.1.2. These classifications are used by the local avalanche warning service at County Road 53 Tyin-Årdal for describing both the potential sizes as well as the observed sizes from avalanche controls in the area.

Table 2.1.2: Avalanche size standards, classification from EAWS [2024].

Size	Typical length & typical volume	Damage	Runout
1 Small	10-30 m, 100 m^3	Unlikely to bury a person, except in run out zones with unfavourable terrain features (e.g. terrain traps)	Stops within steep slopes
2 Medium	50 - 200 m, 1 000 m^3	May bury, injure, or kill a person	May reach the end of the relevant slope
3 Large	Several 100 m, 10 000 m^3	Can bury and destroy cars, damage trucks, destroy small buildings and break a few trees	May cross flat terrain (well below 30°) over a distance of less than 50 m
4 Very large	1 - 2 km, 100 000 m^3	May bury and destroy trucks and trains. May destroy fairly large buildings and small areas of forest	Can cross flat terrain (well below 30°) over a distance of more than 50 m. May reach valley floor
5 Extremely large	>2 km, >100 000 m^3	May devastate the landscape and has catastrophic destructive potential	Reaches the valley floor. Largest known avalanche

2.1.3 Snowdrift

The wind is essential for distribution of snow and the degree of avalanche danger [Tabler, 1994; Margreth, 2007; Statens Vegvesen, 2014b]. Avalanches are often triggered in places that collects a lot of snow, i.e. terrain that is sheltered from the wind (lee-areas) [Lehning & Fierz, 2008]. The wind can be described as the builder of avalanches, in that it transports, redistributes and packs the snow - strengthening the bonds in cohesive slabs [Lied & Kristensen, 2003]. Such lee-areas are various terrain depressions of different sizes and designs, such as bowl-shapes, gullies, and stream valleys on the mountain side.

Plateaus within an avalanche-prone area can cause relative large amounts of snowdrift into the mountainside and cause larger avalanches than the formations in the mountainside, in isolation, give the impression of [Tabler, 1994]. Because the danger of avalanches is primarily related to how quickly the snow settles on a mountainside or in a slope, a full storm in the mountains will mean that the avalanche danger increases faster than at lower wind speeds - due to hard packing of the snow, making for stronger cohesive slabs that might release as units when laying on top of a potential weaker layer of snow [Lied, 1976; Lied & Kristensen, 2003].

The movement of snowdrift is explained by the terms; creep, saltation, and turbulent diffusion [Mellor, 1965; Tabler, 1994] (Fig. 2.1.12):

- Creeping particles happen in dry snow, rolling along the surface, and can form snow ripples and sastrugis (snow shapes that resemble sand dunes) [Kobayashi, 1972].

- Saltating particles are more influenced by the wind, causing them to bounce against the surface and rebound into each other. Snowdrift happens mainly within 80 centimeter above the snow surface, accounting for 97.73% of the overall snow mass transport [Zhang et al., 2022].

- In a turbulent diffusion, the particles are suspended meters up in the air by turbulent eddies, causing them to travel long distances without touching the ground. This is visually the most dominant mechanism in snow storms [Mellor, 1965]. Research shows that wind speed increases with height above the surface due to the diminishing drag of the earth's surface [Mellor, 1965; Tabler, 1994; Statens Vegvesen, 2014a].

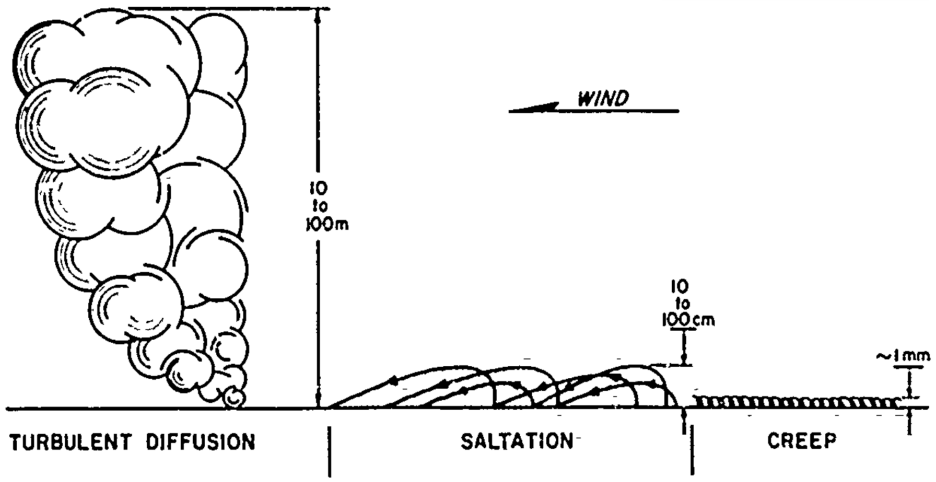

Figure 2.1.12: The three modes of snowdrift. [Mellor, 1965].

Although snowdrift can happen 10s of meters above the surface, the concentration of snow particles >5 meters above ground is negligible for purposes of snowdrift control [Tabler, 1994]. In addition to initiating snowdrift, the wind also contributes to snow loss via sublimation [Nemoto & Nishimura, 2004; Zhou et al., 2014; Huang & Shi, 2017]. Whenever relative humidity is less than 100%, over half of the snowdrift can evaporate over a transport distance of 3 km - even when temperatures are well below freezing [Tabler, 1994].

This means, there are a lot of uncertainties regarding quantification of snowdrift due to abundance of factors affecting the spatio-temporal variation of it. This includes high local wind variations [Mellor, 1965; Tabler et al., 1990; Lehning et al., 2002; Nemoto & Nishimura, 2004], meteorological conditions affecting the snow properties and therefore the threshold conditions for erosion and transport [Colbeck, 1983; L. Li & Pomeroy, 1997; Birkeland et al., 2001; Schauer et al., 2021; Hancock et al., 2021], as well as the spatial heterogenity of the snowpack [Colbeck, 1982, 1997; Schweizer et al., 2008; Clark et al., 2011].

Due to several physical processes affecting the threshold conditions for snowdrift, reported threshold wind speed values vary between studies:

According to Tabler [1994], fresh snow starts to drift when winds are approx. 5.6 m/s, whereas harder snow - affected by winds and/or thaw-freeze processes - can withstand erosion at speeds exceeding 23.6 m/s. Snowdrift usually stops when the wind speed goes below approx. 6.7 m/s.

The study by L. Li & Pomeroy [1997] recorded most of the snowdrift in the wind speed interval 7-14 m/s for dry snow, averaging at 9.9 m/s, and that the mean threshold wind speed for transport of fresh snow was 7.5 m/s, and 8.0 m/s for aged snow.

Figure 2.1.13 shows the results from the study of Kotlyakov [1961] assessing the relationship between snow hardness and the wind speed necessary for erosion of the dry snow in Antarctica.

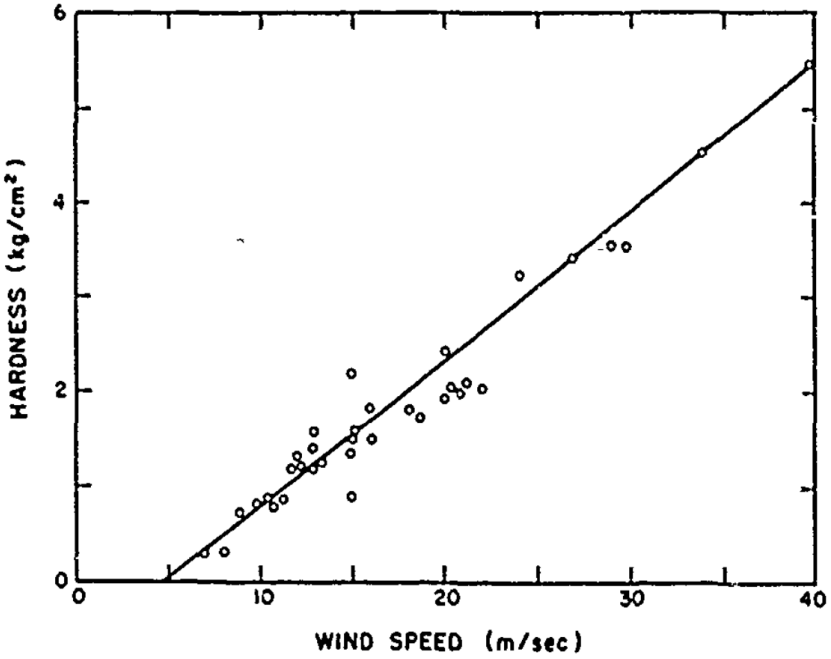

Figure 2.1.13: Relationship between snow hardness and the windspeed necessary for erosion of the snow. [Kotlyakov, 1961; Mellor, 1965].

Estimation of snowdrift mass flux and the occurency of it is considered important for construction and operation of winter roads [Norem, 1974, 1975b,a; Thordarson, 2002; Tabler et al., 1990; Tabler, 1994, 2003; Margreth, 2007; Statens Vegvesen, 2014a] as well as for avalanche forecasting [Chritin et al., 1999; Lehning & Fierz, 2008; Vionnet et al., 2018; Baron et al., 2023; Skred AS, 2023b].

2.2 Site-Specific Avalanche Forecasting and Avalanche Control

Local avalanche warning has the benefit to adapt to local climate, topography, avalanche dynamics, avalanche paths, and other local conditions. Choosing the best type of security measurement for a specific avalanche danger is deemed important, and a system determining critical avalanche size and new snow height, as well as the type of expected avalanche dynamic is considered very

useful for this purpose.

While regional avalanche warning is somewhat standardized in Europe by European Avalanche Warning Services (EAWS) [Müller et al., 2023, 2024], that is not the case for local avalanche warning [Jaedicke et al., 2018; Øien & Albrechtsen, 2022]. There are also no specific Norwegian guidelines [Engeset et al., 2020] although there are several different practices around Norway delivering local avalanche warnings. Most of them are related to the avalanche warning service Nordnorsk Skredovervåkning (NNSO), which is a cooperation between several municipalities in northern Norway, together with Norwegian Meteorological Institute (MET), The Norwegian Geotechnical Institute (NGI), the Norwegian Public Road Administration (NPRA), and The Norwegian Water Resources and Energy Directorate (NVE). The area of responsibility stretches over an area of 22 300 km^2 and consisted of 130 avalanche paths in 2014 [Jaedicke et al., 2014]. There are mainly three companies who undertake tasks related to avalanche path warning: Skred AS, NGI, and Wyssen Avalanche Control Norway [NVE, 2021].

A survey by Jaedicke et al. [2018] showed that different local avalanche warning practices throughout Europe use a great variety of methods and tools both in the avalanche hazard assessment and in the communication of the results, but that most of the practices adhere to the standards and routines from EAWS [2024] through using the European avalanche danger scale, but adopted for the local conditions.

There is however a departure from using the current European avalanche danger scale, as Müller et al. [2023] presented revised definitions, workflow, and EAWS Matrix which were accepted at the EAWS general assembly in 2022. The current European avalanche danger scale is considered to be updated based on further discussions and data from the matrix usage in the future - incorporating the defined terms.

The revisions from Müller et al. [2024] present definitions of terms to be used in a workflow (Tab. 2.2.1) to describe the snowpack stability, frequency of the snowpack stability, and the avalanche size. This provides the basis for choosing the corresponding danger level from the look-up table EAWS Matrix (Fig. 2.2.1), which then helps determine the necessary measurements for the region [Müller et al., 2023].

Table 2.2.1: Workflow to determine the avalanche danger. Extracted from Müller et al. [2023].

Task		Explanation and remarks		
1	**Assess which avalanche problems are present**	Choose from the avalanche problems defined by European Avalanche Warning Services [2022]		
	If no avalanche problem exists, the avalanche danger level is 1-low.			
2	**For each of these problems, assess the locations (elevation, aspect) where and time of the day when the problem is present.**			
3	**For these locations/times assess the classes of snowpack stability.**	Snowpack stability is related to the question: "What does it take to trigger an avalanche?" Often, the locations with the lowest snowpack stability are decisive.	***Stability class*** Very poor Poor Fair Good	***How easy is it to trigger an avalanche?*** Natural/very easy to trigger Easy to trigger (e.g., a single skier) Difficult to trigger (e.g., explosives) Stable conditions
4	**For these stability classes, assess the frequency.**	The frequency is related to the question "How frequent are points where avalanches can release by the trigger specified in step 3?"	***Frequency class*** Many Some A few None	***Description*** Points are abundant Related to specific terrain features Points with this stability class are rare. Points do not exist / are not relevant
5	**Assess the avalanche sizes**	Avalanche size is related to the question: "How large can avalanches become?" Often, the largest avalanche size you consider likely is decisive.	***Size - name*** 1 - Small 2 - Medium 3 - Large 4 - Very large 5 - Extreme	***Destructive potential*** Unlikely to bury a person May bury, injure, or kill a person. May bury and destroy cars May bury and destroy trucks May devastate the landscape
	In case the snowpack stability, frequency and/or avalanche size vary considerably between aspects and/or elevations and/or during the forecast period, repeat steps 3 to 5 to identify the locations/times with the most severe combination of these three factors.			
6	**Refer to the EAWS Matrix and obtain the danger level for the combination of snowpack stability, frequency and avalanche size selected in steps 3-5.**			
	Repeat steps 2 to 6 for other avalanche problems that are present.			
7	**Choose the highest danger level obtained in step 6.**			

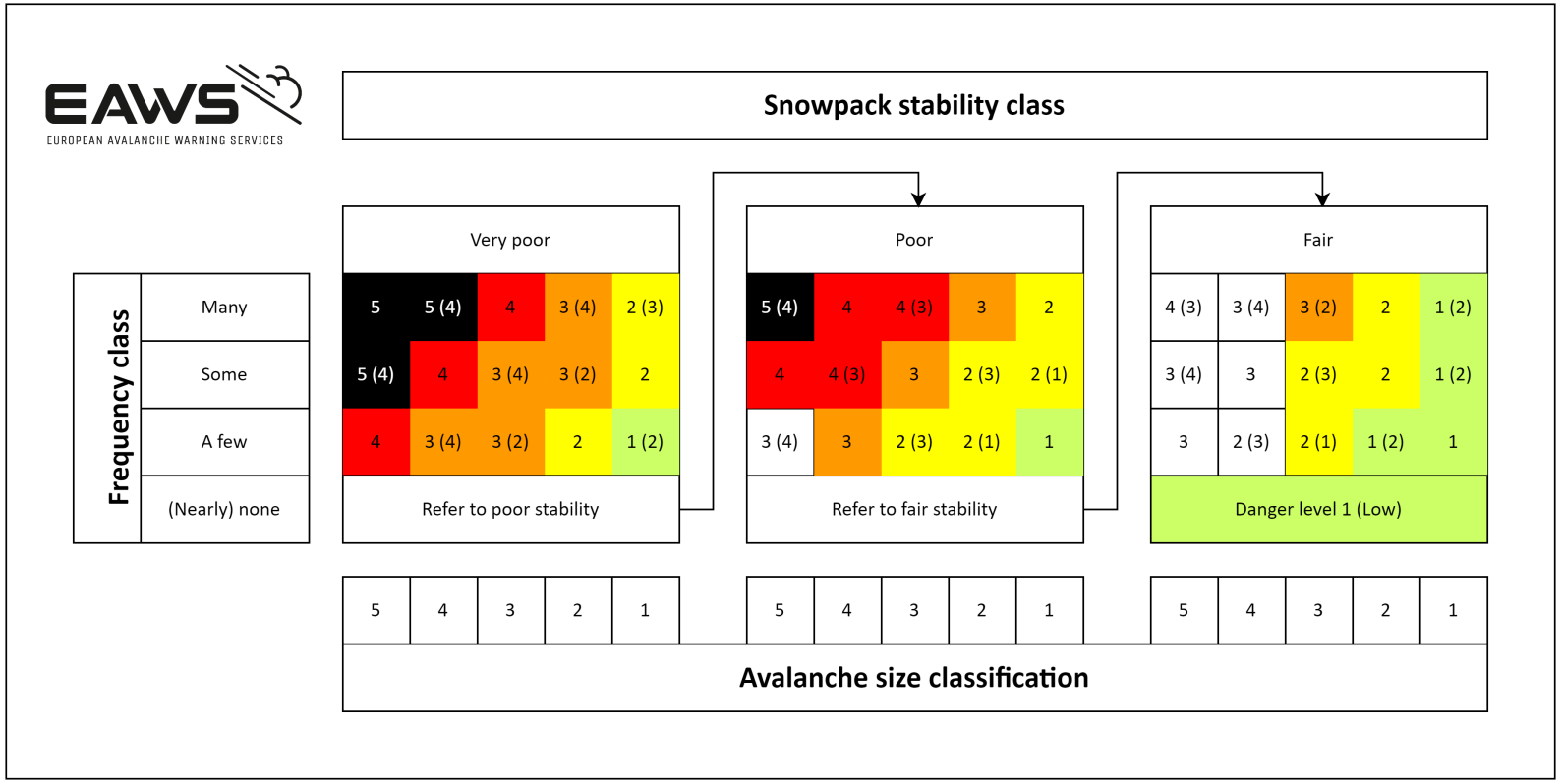

Figure 2.2.1: The EAWS Matrix [European Avalanche Warning Services, 2022]. According to the workflow by Müller et al. [2024], the forecasters initially evaluate the frequency of the most vulnerable locations, moving left to right across the panels. When the stability-frequency combination is decided, the avalanche size is assessed, leading to the recommended danger level.

2.2.1 Swiss Guidelines for Local Avalanche Control

The documented Swiss method for local avalanche warning [Stoffel & Schweizer, 2008] is presented here with the primary aim of providing insight even though this method is not specifically applied in Norway - although there are clear similarities. This method is considered because this is one of very few documents available regarding the processes of local avalanche warning [Jaedicke et al., 2018; Øien & Albrechtsen, 2022]. Nonetheless, it is regarded as useful knowledge that can contribute to the reader's understanding of the decision-making processes in Norway, as well as general winter operation of norwegian roads. Some specific routines from Skred AS' Remote Avalanche Control System (RACS) at County Road 53 Tyin-Årdal are also presented in this section as supplementary notes.

Swiss national guidelines for local avalanche control services were established by Stoffel & Schweizer [2008] after Switzerland experienced an extraordinary winter with an abundance of avalanches during 1998-99.

There is a three-step scheme suggested for hazard assessment by local avalanche control services: **1)** Data analysis and danger evaluation **2)** Assessing the hazard to people and infrastructure **3)** Decision on preventive measures. These three steps are reviewed in the following subsections.

Initially, for a local avalanche control services to follow their responsibilities, they must have access to or establish several essential documents. These documents include:

- Avalanche map (or atlas): A map that delineates avalanche paths, including PRAs and runout areas, terrain inclination, as well as any existing avalanche protection measures such as supporting structures. It may also include a table detailing terrain characteristics such as altitude, inclination, aspect, topography, along with accompanying photographs.

  In Norway, a map catalog provided by NVE [2024b] gives an overview over useful map themes such as caution maps and hazard areas. There are some areas in Norway that already include more detailed avalanche danger areas that are conducted from specific assignments, but in most other places a caution map is the most widespread. Such caution maps are either processed by

  1) a topographic-statistical run-out model called alfa-beta method [Lied & Bakkehøi, 1980; Bakkehøi, 1983; Lied & Kristensen, 2003; Norem & Sandersen, 2012], that calculates the runout of avalanches, rockfalls, or landslides - based on topographic criteria using empirical data on historical avalanche events

  2) dynamic modeling with the numerical model MoT-Voellmy integrated with NAKSIN [Issler et al., 2023] - which, in addition to topographic

criteria, accounts for local climate and forest conditions, taking into account areas with usually little to no snow, and areas where forests have a significant influence on a potential release or the possible runout distance.

- Avalanche history: A document with records on the dates of significant avalanche events, including details such as the extent of the run-out and resulting damage. It may also be visualized on a map, showing the area extent of the events.

  In Norway, such registrations are to be found on either Varsom Regobs [Varsom Regobs, 2024] or Skredregistrering [NVE, 2024d] - where the same data can be easier visualized through NVE-Temakart [NVE, 2024c], NVE-Atlas [NVE, 2024a], or Varsom Xgeo [Varsom Xgeo, 2024].

- Endangered objects and potential damage: This information is typically organized in a table format, detailing the number and types of buildings or structures at risk, as well as evacuation zones. Different building types have different degrees of risk. For example, kindergartens and emergency services are considered more vulnerable than cabins. Alternatively, it may be GIS-based for more comprehensive analysis and visualization.

Data Analysis and Danger Evaluation

Based on the snow and weather data in to the region, both from empirical observations as well as forecasts, the avalanche situation can be assessed. The different parameters in such an assessment are summarized in Table 2.2.2. If observations and forecasts indicate that parameter values from this table might get exceeded - and crosses the threshold values which are based on historical experience and modeling of the area - then the avalanche control service must determine the probability of release, and the potential avalanche size.

At County Road 53 Tyin-Årdal, the critical avalanche sizes are by Skred AS [2022] defined by both the necessary fracture height and release volume of a theoretical avalanche that can reach the infrastructure of focus. The volumes can also be classified with the EAWS definitions [EAWS, 2024] on avalanche sizes. The critical fracture heights from the different PRAs along County Road 53 Tyin-Årdal are by Skred AS [Skred AS, 2022] based on numerical modeling in RAMMS [Christen et al., 2010]. These models are calibrated from real events, and inputs fracture heights, release volumes, friction parameters, and outputs runout lengths, flow height, density, and velocity.

Table 2.2.2: Data analysis and danger evaluation. From Stoffel & Schweizer [2008]

Data and observations	- public avalanche bulletin - new snow - snow depth - wind - temperature (air, snow) - snowpack stratigraphy (existence of weak layers) - avalanche activity (natural activity and results of explosive control) - eventual information from neighbouring services or ski areas
Forecasts (for the next hours)	- weather - public avalanche bulletin (development of danger and danger level) - new snow amout (snow fall limit) - wind (direction and speed) - air temperature trend
Conclusions	→ estimate of locally prevailing avalanche danger and its trend → people or infrastructure endagered? - If yes, proceed with further assessment - If no, time of next evaluation (repeating these steps) or possible explosive control to prevent large avalanches

Assessing the Hazard to People and Infrastructure

Following an assessment of the general danger in the region, the next step is identifying specific avalanche risks. This entails estimating the probability of avalanches occurring in one or more paths, as well as evaluating whether they pose a threat to individuals or infrastructure due to their potential size. It's important to note that such estimations regarding the probability of release and avalanche size and runout dynamics for each path typically carry a significant degree of uncertainty. This uncertainty must be taken into consideration when making decisions on preventive measures (in the next step).

The hazard assessment for specific avalanche paths takes into account various factors:

- The terrain features of the path, such as slope inclination in the starting zone and the undulation of the path.
- Past avalanche activity, which can affect the extent of avalanches in the run-out zone.
- The efficiency of permanent protective measures, such as buried supporting structures or filled dams from previous releases.
- Current snow conditions in the PRA, path, and the run-out zone.
- The expected avalanche dynamics.

Assessing conditions in specific PRAs relies on extrapolating data evaluated in

the first step, which entails an uncertainty. During storms, visibility may be poor, hindering direct observation and thus adding to the uncertainty.

When evaluating release probability and avalanche size, comparing current new snow depth with a predetermined critical value - based on historical data or avalanche modeling - proves useful [Stoffel & Schweizer, 2008]. This critical value must be adjusted based on present conditions, such as wind speed and direction, snowpack stratigraphy, temperature, and snowpack humidity.

The possibility of extreme avalanche events must always be considered. For that case, an avalanche hazard map is recommended. Although such events may not have been observed for several decades, it cannot be disregarded, particularly in extreme circumstances [Stoffel & Schweizer, 2008].

Decision on Preventive Measures

Based on the assessed probability and potential size of the avalanches in the specific avalanche paths, a decision must be made on potential preventative measures. Such measures may include road closures, artificially triggering of avalanches through blasting, restrictions for people in residential areas, and/or evacuations. Implementing restrictions for people in residential areas requires buildings to be reinforced.

An evacuation plan must be in place, and residents should be informed in advance about evacuation procedures to ensure safe evacuation process. Similarly, a plan detailing the areas to be closed and the placement of temporary closure barriers should be established, depending on the degree avalanche danger. Avalanche warning signs must be available.

An example of different caution levels with associated measures, for Skred AS' local snow avalanche warning along County Road 53 Tyin-Årdal, are shown in Table 2.2.3. Wyssen avalanche towers, with explosive charges, are used to artificially release avalanches from the different PRAs in the terrain. Figure 2.2.2 shows Lohne, P. (Skred AS) carrying out an ongoing avalanche control in coordination with the plowing crew.

Record-keeping of snow and weather data, observations, and decisions regarding measures is essential. It is advisable to provide justifications for the decisions made, whether why a preventive measure was suggested or dismissed. In cases where avalanche control is applied, documentation should include a table detailing the date, location, method, and results of the blasting.

Table 2.2.3: Definition of caution levels. From Skred AS' Remote Avalanche Control System (RACS) at County Road 53 Tyin-Årdal.

Level	Caution (recommended level)	Measures (recommended level, typical restrictions)
Green	Normal attention	No particular measures, normal operation
Yellow	Increased attention	Daily avalanche warning Avoid manual operations (e.g. brushing road signs)
Orange	Some restrictions	Daily avalanche warning Avoid manual operations (e.g. brushing road signs) Restrictions on work operations (snow plowing) Closure can happen at short notice. Possible opening can be considered. Consider avalanche control
Red	Comprehensive restrictions	Daily avalanche warning Closed road Avoid working in specified area Consider avalanche control

Figure 2.2.2: Lohne, P. (Skred AS) carrying out the avalanche control 21.02.2023, here in communication with the plowing crew from the NPRA - making sure the restrictions are met during the avalanche control. Picture taken by Falkeblikk AS, as commissioned by NVE.

2.3 Snowdrift Sensor FlowCapt 4

At the County Road 53 Tyin-Årdal, a FlowCapt 4 (FC4) snowdrift sensor is installed by Skred AS, the NPRA, and Innlandet County. The sensor measures solid particle flux intensities and wind speeds.

While such acoustic sensors have yet to reach the precision required for research applications [Font et al., 1998; Michaux et al., 2000; Jaedicke, 2001; T. Sato et al., 2005; Das et al., 2012; Trouvilliez et al., 2015; Zhang et al., 2022; Baron et al., 2023], they are considered a useful tool for avalanche forecasters in practical application - monitoring periods of snowdrift in a more qualitative/semi-quantitative way [Chritin et al., 1999; Jaedicke, 2001; Lehning et al., 2002; Lehning & Fierz, 2008; Vionnet et al., 2018; Skred AS, 2023b].

The sensing part of the instrument is a cylindrical coated tube (anti-abrasion, anti-adhesion, and anti-rime) that records change in internal acoustic pressure generated by mechanical impact from snowdrift particles [ISAW, 2024a]. Microphones inside the tubes transmit signals to a frequency analyzer, and through Fourier transformations, the signals can be differentiated into high frequencies from snowdrift particle impacts, and low frequencies from the loosening wake eddies behind the tube [Jaedicke, 2001]. The sound is transformed into a signal proportional to the snow drift flux in g/m^2/10 minutes.

This method enables simultaneous measurement of snow drift flux and wind speed. Wind data from the FC4-sensor is not used in this study as there is a weather station mounted on the same mast as the FC4, providing higher quality wind data at this location.

2.3.1 Sensor Setup and Configuration

The mast installation on the plateau above County Road 53 Tyin-Årdal consists of two components (Fig. 2.3.1):

- A Gill GMX compact weather station that measures temperature, air humidity, wind speed and direction. It uses an ultrasonic sensor and electronic compass. It is mounted on the top of the mast, just above the FC4 sensor (at approx. 2.5m height). The measurement intervals of the weather station are adapted to the intervals of the FC4 sensor, such that the data has same time periods.

- Two FC4 tubes placed above each other (0-1 m above the ground, and 1-2 m above the ground). The data is collected using a Campbell Scientific data logger. The sensor and logger are powered by a 12V lilthium battery

that is recharged using a solar cells on panel of 10W.

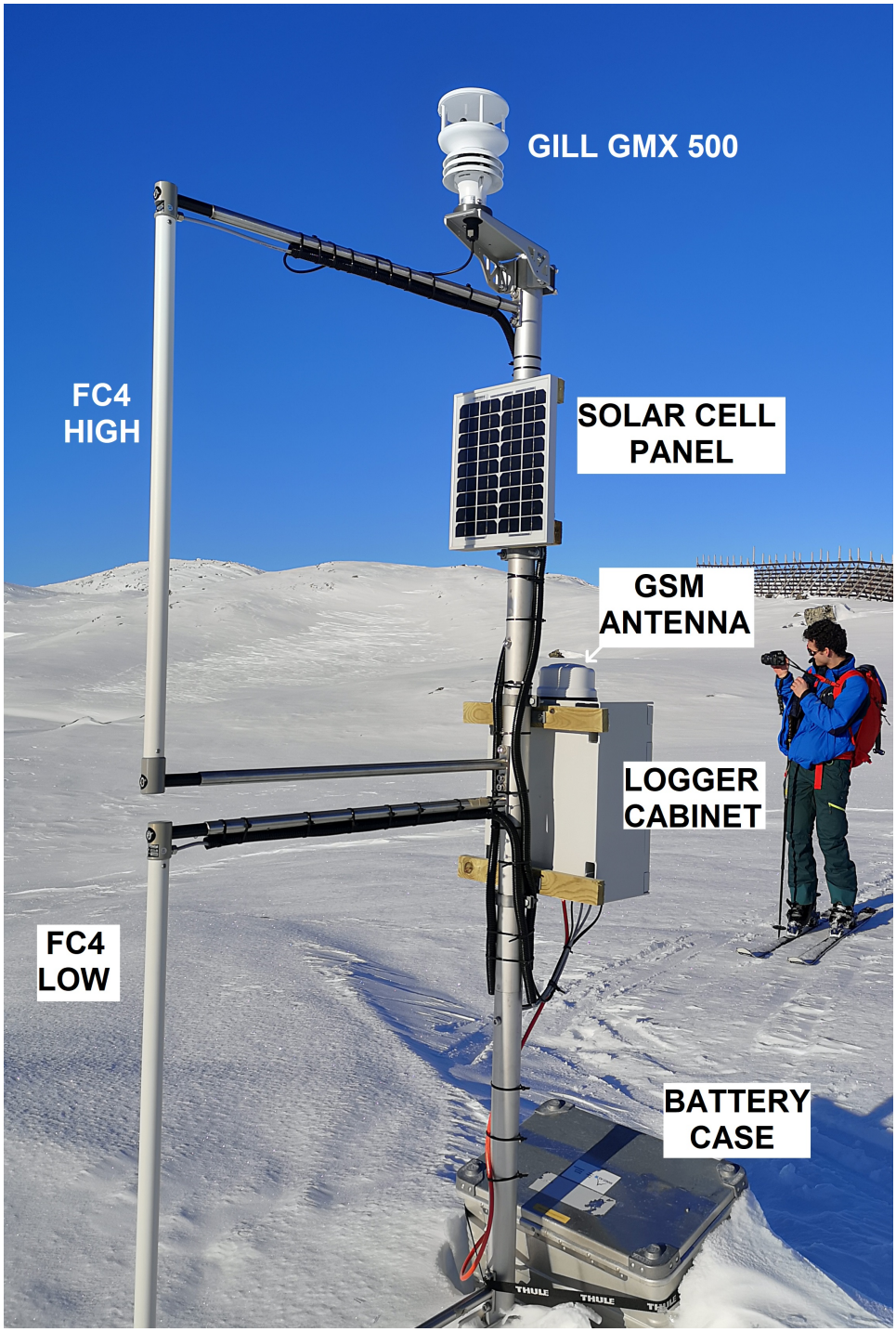

Figure 2.3.1: Overview of the installation. Picture taken by author 14.02.23.

The FC4 has no moving parts, and has relative low power consumption, which makes it suitable for locations with limited power access. The sensor is configured to actively measure for 6 seconds every minute. It then compiles the average, maximum, and minimum values for 10-minute periods. This gives a situational picture that is closer to the reality compared to single measurements, see Figure 2.3.2.

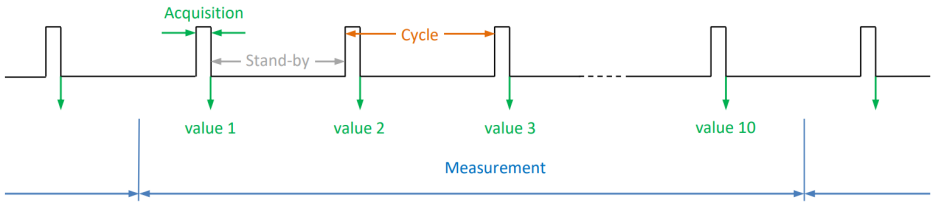

Measurement settings	Description	Default value
Acquisition duration [A]	True observation time of the physical phenomena, also called *time integration window.*	6 seconds
Cycle duration [C]	Sum of the acquisition duration and a stand-by duration.	1 minute
Measurement duration [M]	Reading/writing data interval, called *averaging duration.*	10 minutes
Duty cycle	Ratio between acquisition duration and cycle duration, i.e. fraction of time in which the sensor is effectively active.	10%

Figure 2.3.2: Measurement interval for the FC4 sensor [ISAW, 2024b].

The data logger CR350-Cell215 from Campbell Scientific is used for the collection of measurement data. The measurement data is sent via the 4G/5G mobile network (Telenor) to a local FTP server. Throughout the winter season, Grafana (open source observability platform) is used for storing and displaying the measured data. The FC4- and weather station data can be downloaded from this platform - which is done in this study prior to further data analysis as presented in Section 5 - Results.

2.3.2 FlowCapt 4 Experiences and Analysis

The experiences from the snowdrift sensor FC4 during the first winter season (2022/23), after installation December 2022, showed that the threshold value for registered snowdrift transport were 10 m/s - a bit higher than classic table values stating that fresh snow starts drifting at around 5-7 m/s [Kotlyakov, 1961; Tabler, 1994; L. Li & Pomeroy, 1997]. A possible explanation is the placement of the sensor on a small elevation in the terrain, which cause the snowdrift at lower wind speeds to follow the topography in the depressions around the elevation [Skred AS, 2023b]. Most of the snowdrift was measured with winds from the north-west, and the harshest winds came from the west. This was also experienced by Wyssen Norge AS [2020, 2021] in previous winter seasons

with avalanche warning. Snowdrift was measured in temperatures between -12 and 0 degrees.

The FC4-sensor in combination with the weather station provided valuable data basis for site-specific avalanche warning and planning of avalanche control for County Road 53 Tyin-Årdal. The snowdrift sensor provided the forecasting group useful information about the weather situation in periods where local observations and web cameras gave no information due to storms and poor visibility. The continuous data measurements, in contrast to point observations (snowpits and webcam), gave the forecasting group a basis to evaluate duration of snowdrift periods. This contributed to qualitatively assess the total accumulation in the PRAs, making it easier to make the decision whether to close the road or not - for conducting avalanche control by blasting.

Skred AS believes, that through further analysis, data experience, and installation of snow depth gauges, would make it possible to establish threshold snowdrift mass flux values for correlated critical amounts of snowdrift deposition in the PRAs.

Some of the recommendations mentioned in the report by Skred AS [2023b] were:

- To establish snow depth measurements in combination with FC4, to observe how snowdrift correlates with snowfall and snow available for transport.

- To establish snow depth measurements in PRAs to assess deposition caused by snowdrift. This can be done in combination with the establishment of terrain models using drone photogrammetry/laserscan.

In addition to the usage of laserscans for this study, a snowdepth sensor (DecentLab MBX-01 sensor) have subsequently been installed March 2024 at the area of Tyinstølen, for a more extensive analysis in the future.

2.4 Remote Sensing

An introduction to remote sensing is provided as laserscans were conducted in the fieldwork collecting data on the snow depth changes. Knowledge of the quality of the output data and the reliability of the derived information with this technology is important, especially for research context.

Remote sensing is the collection of information about objects or phenomena on the Earth's surface without direct physical involvement [Dozier, 1989b]. This

is accomplished using sensors located on satellites, aircrafts, or ground-based platforms. Remote sensing is based on the interaction between electromagnetic waves and matter, where the backscattered light from objects and its time delay and frequency shift is registered [Aggarwal, 2004; Gibson et al., 2013; Elachi & Van Zyl, 2021] - making it possible to assess the distance to each point and create a Digital Elevation Model (DEM) [Cracknell, 2007].

In snow science, remote sensing has long been recognized for its potential and has been utilized in acquiring snow data via satellites [Rango & Itten, 1976; Chang et al., 1982, 1987; Dozier, 1989a; Hall et al., 2002; Nolin, 2010; Kapper et al., 2023]. In contrast, field-based approaches often include significant uncertainties and gaps in the spatial distribution, affecting the risk assessment and detailed comparison with meteorological triggering factors [Eckerstorfer et al., 2016]. Using satelittes, aircrafts, and ground-based remote sensing can fill these data gaps, offering improved quantitative measures of snowpack and avalanche activity and dynamics [Nolin, 2010].

Fundamental research questions in avalanche science have remained consistent over the decades. Researchers continue to strive for knowledge regarding the timing, location, type, and size of avalanches, along with the contributing factors of topography, meteorology, and snowpack properties [Eckerstorfer et al., 2016].

Remote sensing instruments can be categorized into active and passive. Passive sensors measure the radiation that is naturally emitted or reflected by the target from external sources such as the sun [Tedesco, 2015]. Active sensors emit energy and measure the amount reflected back or backscattered by the target as a function of range [Collis, 1970]. Active sensors include Radio Detection and Ranging (RADAR) and LiDAR [Eckerstorfer et al., 2016].

2.4.1 Light Detection and Ranging (LiDAR)

It has become a standard to use LiDAR in collection of terrain data as it is considered one of the most reliable methods in creation of DEMs [Liu, 2008]. LiDAR-sensors operate by emitting pulses of laser light, usually around 500 - 1550 nm [Sasano & Browell, 1989; Wei et al., 2012; Deems et al., 2013; Budei et al., 2018; Kapper et al., 2023].

A LiDAR sensor measures the time for the pulses to return from solid surfaces by reflection. The time data is calculated to determine the distance between the sensor and the target. Modern LiDAR systems, deployed on drones (Remotely Piloted Aircraft System (RPAS)), incorporate a Global Positioning System (GPS) and sensors to measure the platform's angular orientation relative to the ground, known as the inertial measurement unit [Wallace et al., 2012;

Colomina & Molina, 2014; Kapper et al., 2023]. Real-Time Kinematics (RTK) is an example of technology that takes use of a GPS to gain centimeter-level positioning accuracy during the flight through communication with satellites [W. Li et al., 2021]. Figure 2.4.1 shows a LiDAR-mounted drone that uses RTK technology.

Figure 2.4.1: A LiDAR-mounted drone operated by Solbakken, E. from the NPRA. Picture taken by the author 21.02.23.

Active remote sensing of snow avalanches by using LiDAR was first demonstrated by Prokop [2008] focusing on the factors affecting the accuracy of the measurements such as weather conditions and scanner position. Deems et al. [2014] used a similar approach on calculating the volume of snow avalanche mass based on changes in snow cover, measured under both snow-free and snow-covered conditions. Sovilla, McElwaine, et al. [2010] measured snow depths just before and after a snow avalanche to measure snow depths of

avalanche masses, giving an improved estimate of avalanche mass depths compared to traditional methods such as manual inspections and photogrammetric methods.

The primary data output from a LiDAR survey is a geo-located point cloud. The point cloud is quantified by ground point spacing (distance) and ground point density (number of points per unit area). The output depends on factors like pulse repetition frequency, flight speed, flight route, scan angle, scan frequency, swath overlap (for achieving desired ground point spacing), and target area characteristics (complexity and reflectivity) [Tedesco, 2015].

LiDAR-data is commonly applied as raster format, which facilitates accessibility and compatibility with various software applications, such as in a Geographic Information System (GIS). Raster data, also known as gridded data, are organized as a grid of values represented by pixels on a map, where each pixel denotes an area on the Earth's surface. Unlike standard images, these raster files are spatially referenced, meaning each pixel corresponds to a specific geographic location, determined by the raster's spatial resolution [Wise, 2018].

For converting LiDAR-data to raster data, values from the LiDAR point cloud are associated to a raster grid, and each pixel/cell in that grid is given a value based on the points that fall within the cell's spatial extent. Alternatively, interpolation methods can be employed to estimate cell values by considering nearby points, both within and outside the cell. Interpolation often involves statistical operations to calculate cell values, thereby enabling predictions in areas lacking data points. Understanding the error associated with these predictions is essential, particularly in research contexts, for assessing the reliability of derived information [Wasser, 2018].

There are several advantages to using a Remotely Piloted Aircraft System (RPAS) and an Unmanned Aircraft System (UAS) to carry optical remote sensors. This includes gaining access to remote areas, collecting objective observations without direct contact, and collecting continuous data over a period of time [Eckerstorfer & Malnes, 2015].

Some disadvantages are that gathered information are limited to the surface [Awasthi & Varade, 2021], and that cloud cover, low light, and physical obstacles hinder visibility [Prokop, 2008; Rynning, 2019]. There can also be limited opportunity to validate the data in-field.

The NPRA is currently working on method development on the use of LiDARs on UAS to support avalanche monitoring [Statens Vegvesen, 2021]. Their research project Geohazard Survey from Air (GEOSFAIR) - an innovation project for the public sector 2021-2024 in collaboration with NGI and the research institute SINTEF - has produced some experiences regarding workflow, data-gathering, and hardware [Reutz et al., 2022; Frauenfelder et al., 2022; S. Salazar et al.,

2023; McCormack et al., 2024].

The study from Haddad et al. [2023] showed that when forecasters were given additional LiDAR data in the hazard assessment, it allowed them to see the results of the mitigation more clearly - causing them to change their assessment of the avalanche hazard post-mitigation in some cases.

The NPRA is also adopting an autonomous LiDAR-mounted Unmanned Aerial Vehicle (UAV) to monitor the terrain and support decision-making in e.g. areas utilizing road closures as a preventive measure [S. E. Salazar et al., 2023].

3

Study Area

3.1 County Road Fv. 53 Tyin-Årdal

The study area is related to the County Road 53 between Tyin and Årdal in Innlandet County (Fig. 3.1.1). The road stretches 39 kilometers through a weather-exposed mountain pass. The road is particularly prone to avalanches between Tyinkrysset and Tyinosen. From Tyinkrysset, the road starts at 900 meters above sea level, and has a rapid climb up through the forest line (Tyinslinna area) to 1100 meters above sea level, next to the Tyin lake. The road continues at this altitude situated right between the lake in the east and a steep overlying slope of additional 200 meters in the west - a slope that flattens out at the top into a large mountainous plateau. After this road section, at Tyinosen, it begins a slow decline, in a less avalanche-prone area, down to Øvre Årdal in the west. In the section between Tyinkrysset and Tyinosen, the road has several points along the road which are located at the end of several physical avalanche paths. For every winter season, at least a couple of avalanches crosses the road - hindering the traffic, requiring considerable resource use in plowing the road [Wyssen Norge AS, 2020, 2021].

In 2010, the Norwegian Public Road Administration (NPRA) and Innlandet County conducted a trial for a Remote Avalanche Control System (RACS) along this road section, resulting in the installation of fourteen Wyssen Avalanche Towers (Fig. 3.1.2). During the winter of 2019/20, a total of 217 avalanches were registered, with 122 of them artificially released by explosive charges from the towers, and 14 crossed the road [Wyssen Norge AS, 2020].

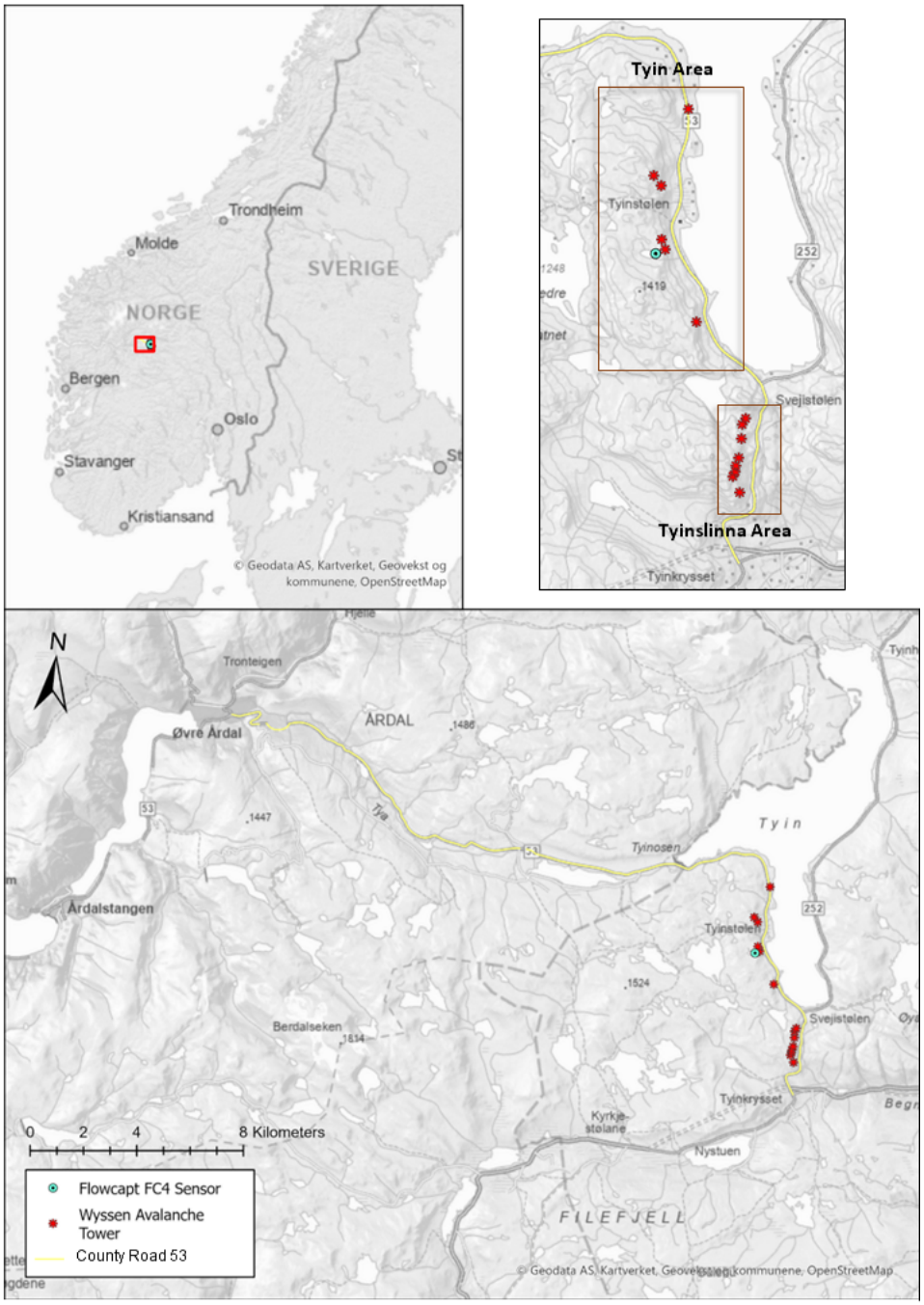

Figure 3.1.1: Location of County Road 53 Tyin-Årdal, the fourteen Wyssen Avalanche towers, and the FlowCapt 4 (FC4) sensor.

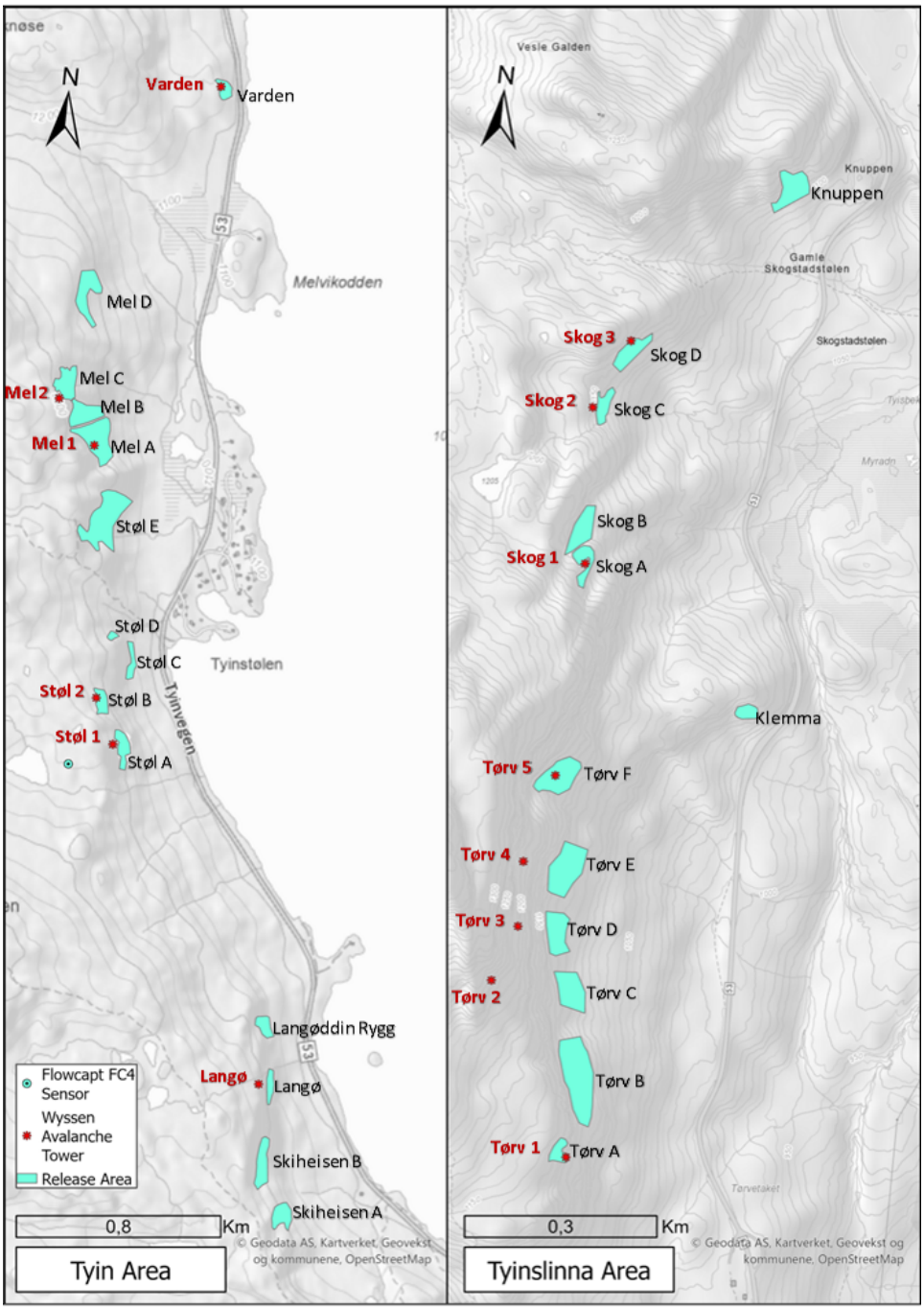

Figure 3.1.2: Tyin and Tyinslinna area - as delineated in previous Fig. 3.1.1. Presents the locations and names of Wyssen Avalanche towers, as well as the associated PRAs used for modeling in RAMMS::Avalanche by Skred AS [2022].

The specific fieldwork area in this study is presented in Figure 3.1.3. Snow cover surveys were conducted on this plateau west of avalanche towers Støl 1 & 2, where also the FC4 is installed. Figures 3.1.4 & 3.1.5 show in field pictures from this area.

Several places along the road have snow fences installed. They are are designed to prevent the accumulation of large amounts of snowdrift in the PRAs [Tabler, 2003]. Tveit [2018] underlined that many of the fences recieved too little maintenance, and in several places fences had collapsed. The three snow fences at Tyinstølen by avalanche towers Støl 1 & 2 have also undergone maintenance over time. These were assessed to have a good effect on reduction of snowdrift deposition in the PRAs related to avalanche towers Støl 1 & 2.

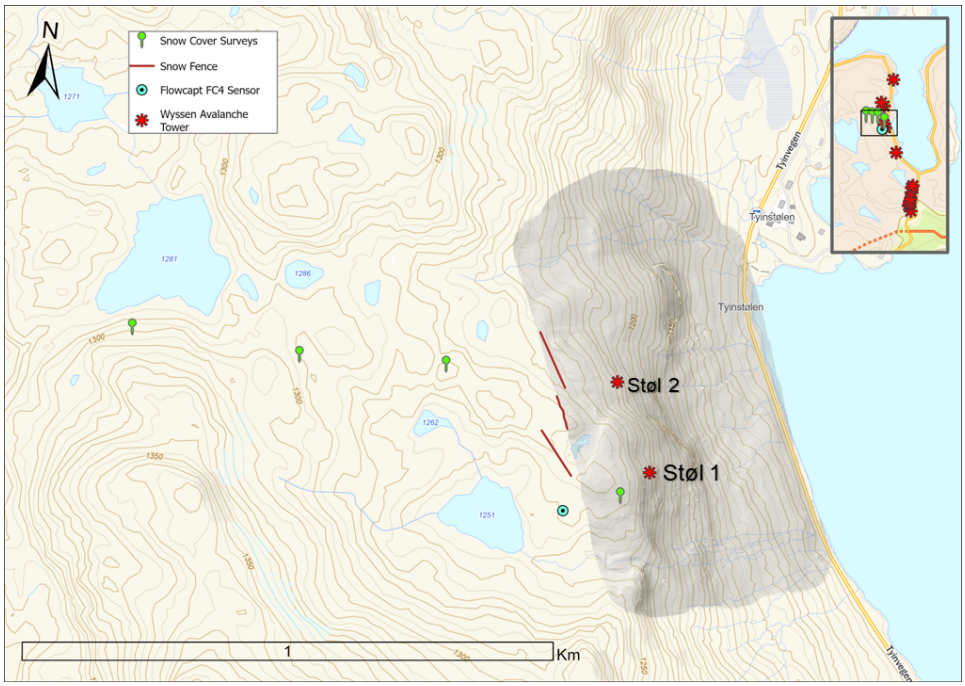

Figure 3.1.3: Overview of the fieldwork area at Tyinstølen, related to the avalanche towers Støl 1 & 2. The area of consecutive LiDAR-scans is displayed as a transparent grey shadow part, and has an accuracy of ±10-30cm - discussed in more detail in Data and Methods Section 4.2.

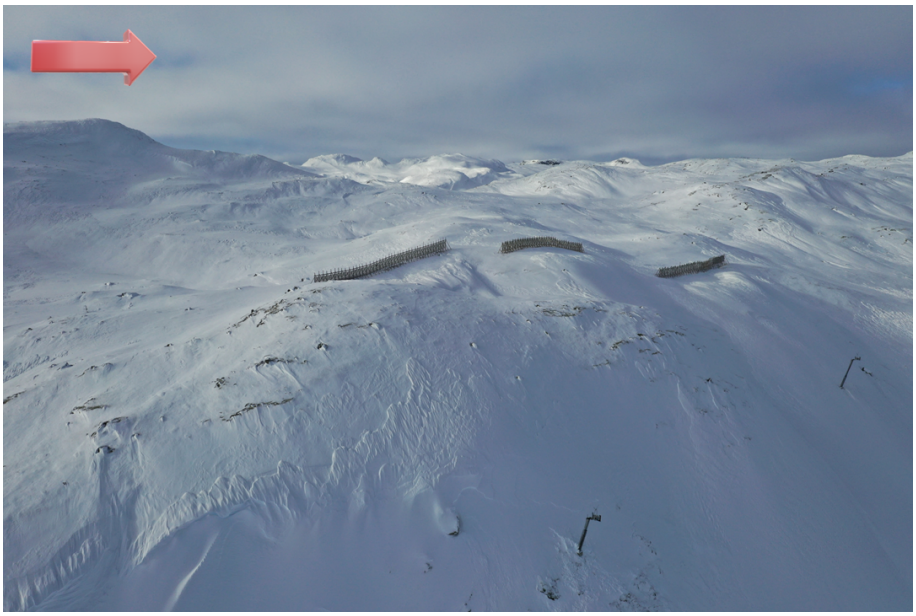

Figure 3.1.4: Avalanche towers Støl 1 (left) & 2 (right), and snow fences. Direction of picture towards NWW. Patches of windslabs on top of the general snow cover (wind crust) can be seen. Picture taken by the author 21.02.2023. Red arrow indicates north direction.

Figure 3.1.5: The snowdrift catchment plateau above avalanche towers Støl 1 & 2. Direction of picture towards south. Patches of windslabs on top of the general snow cover (wind crust) can be seen. Picture taken by Solbakken, E. 21.02.2023. Red arrow indicates north direction.

3.1.1 Road Importance and Consequences of Road Closure

County Road 53 is important for the inner parts of Oppdal County, and particularly the local community of Øvre Årdal as the road connects the community to the European roads in the south-east. There are several drawbacks for the community of Øvre Årdal when the road gets closed during the winters. This includes disruption of transportation, economic impacts on the local businesses, hindering of emergency responses, social isolation, and the inconvenience as well as the environmental consequences due to the necessary transportation detours. Even though snowdrift is a very resource- and cost-intensive process in the operation of winter roads [Tabler, 1994; Thordarson, 2002; Tabler, 2003; Margreth, 2007; Skred AS, 2023b], it is of great importance to mitigate such socioeconomic impacts.

Temporary road closures serve as the primary measure to mitigate the avalanche risk - this is one of the most common ways to meet the traffic safety requirements in Norway [Statens Vegvesen, 2014a]. Applying road closure is an assessment made by the local avalanche warning. The road gets closed when there is an assumption that avalanches might reach the road, based on the previous days' snowfall and wind conditions. The road also gets closed when there has been an avalanche that has crossed the road. This requires the removal of snow through snow plowing (Fig. 3.1.6 & 3.1.7) before the road can open again. During periods of high avalanche danger, the road gets closed over multiple days - this occurs several times during every winter season [Wyssen Norge AS, 2020, 2021]. The RACS is an important HMS tool for the plow drivers. Plowing can be time-consuming (hours) after prolonged closure due to snowdrift, which causes the drivers of the vehicles to have a long exposure time to the avalanche danger.

Figure 3.1.6: Snowplowing after an avalanche crossed the road under avalanche tower Varden. Picture taken 21.02.2023, by Falkeblikk AS as commissioned by NVE.

Figure 3.1.7: The snow covered road of County Road 53 Tyin-Årdal after a snowdrift event. Subsequent avalanche control and snow plowing were conducted later the same day. Avalanche towers Støl 1 & 2 can be seen in the background. Picture taken in the north-west direction by the author 21.02.2023.

The users of the road, such as locals, cabin owners, plowers, and visitors, can expose themselves and others to danger if they inadvertently venture onto the closed road under circumstances of high avalanche danger. In such sitations, there is a large chance of dangerous situations such as:

- Road users and plow vehicles meeting under very poor visibility conditions and might collide.
- Lone road users getting stuck in snowbanks on the road.
- Road users being in the road without the plowing crew knowing about it.
- Malfunctioning of vehicles in harsh weather conditions.

In general, the NPRA continuously remind road users to be up-to-date on the status of the roads, and provide additional notifications along roads (Fig. 3.1.8) as well as on their digital platforms (Road Traffic Central unit, website and app). This is especially important for mountain passes and weather-exposed regions.

Figure 3.1.8: Road sign provided by the NPRA before entering County Road 53 Tyin-Årdal from Tyinkrysset. Sign indicates that the road is closed, followed by a roadblock further up the road. Picture taken by the author 21.02.2023.

3.1.2 Climate and Snowpack Challenges

The road lies within the mountains of Jotunheimen. The majority of the region is situated above the treeline at around 1000 meters. Many mountain peaks tower above 2000 meters, while valley bottoms descend to below 1000 meters at the periphery of the region. Situated more than 150 kilometers from the Norwegian western coast, the climate is transitional between maritime western Norway and the more continental climate from the plateaus and valleys in the east. The area has typical alpine conditions, winters are cold, with temperatures dropping below freezing (Fig. 3.1.9), and the area receives substantial precipitation throughout the winter season (Fig. 3.1.10). Strong winds are very common in the area, especially from the west (Fig. 3.1.11), and wind speeds can increase significantly during storms, contributing to blizzard

conditions, reduced visibility, and huge amount of snowdrift from the large catchment plateau west of the road, facilitating the avalanche hazard and risk along the whole road section between Tyinkrysset and Tyinosen.

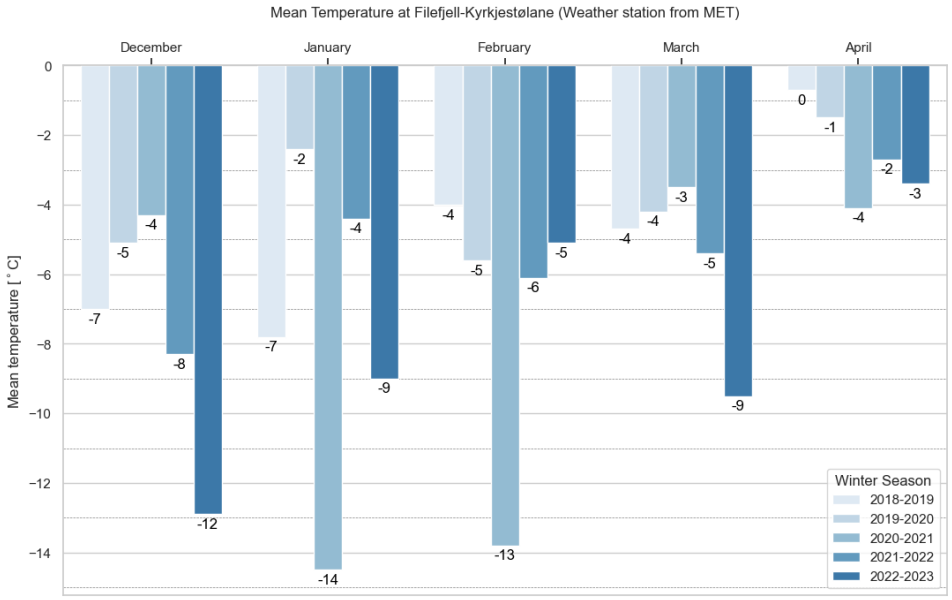

Figure 3.1.9: Mean temperatures during the winter months 2018 through 2023. Data extracted from the weather station by Norwegian Meteorological Institute (MET) [NCCS, 2024], located at Kyrkjestølane - 8km west of Tyinkrysset.

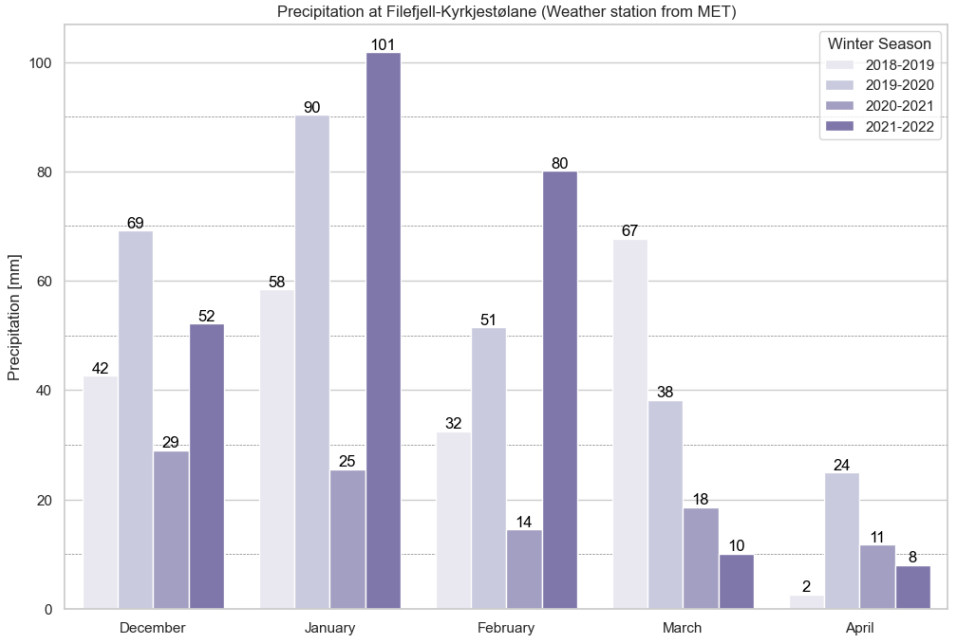

Figure 3.1.10: Monthly precipitation during the winter months 2018 through 2022. Data extracted from the weather station by MET [NCCS, 2024], located at Kyrkjestølane - 8km west of Tyinkrysset.

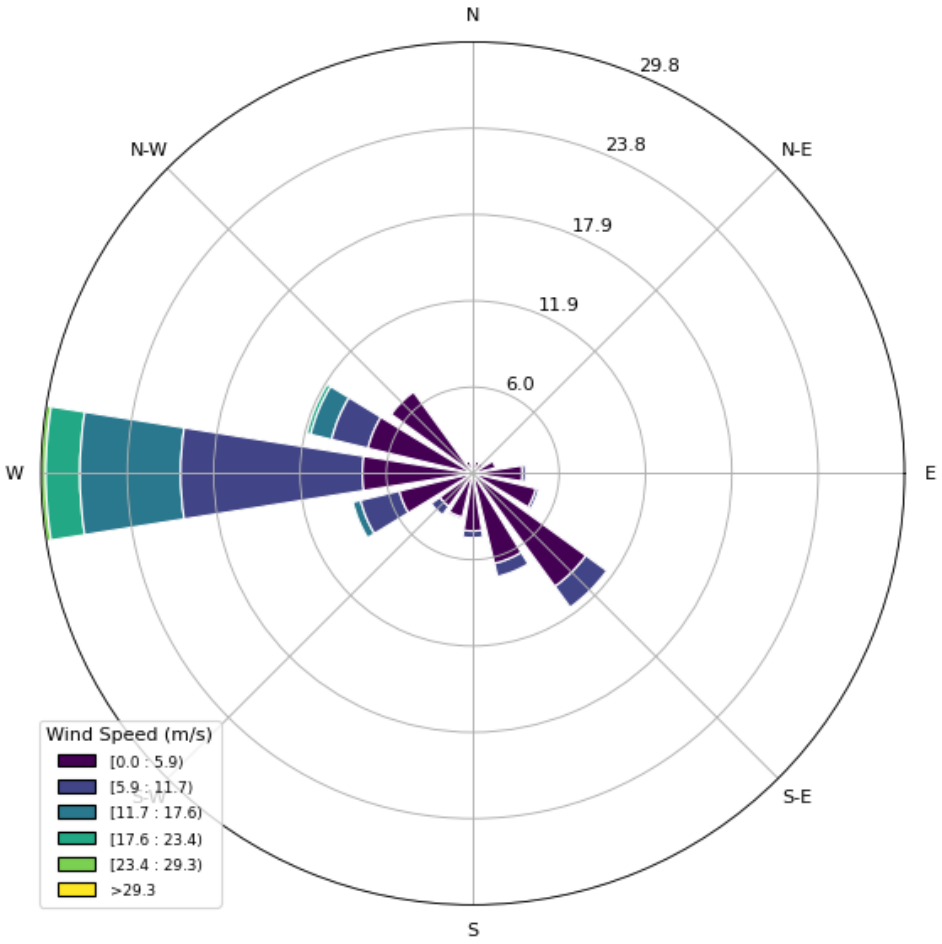

Figure 3.1.11: Wind rose data from the Gill Weather Station on top of the snowdrift sensor FC4 - located at the mountainous plateau west of Tyinstølen. Data period from December through April, in the winter season 2023-2024.

Wind slabs caused by snowdrift is the most reported avalanche problem during winter seasons [Wyssen Norge AS, 2020, 2021]. Figures 3.1.12 & 3.1.13 show the distribution of the defined type of avalanche problems winter seasons 2019/20 and 2020/21.

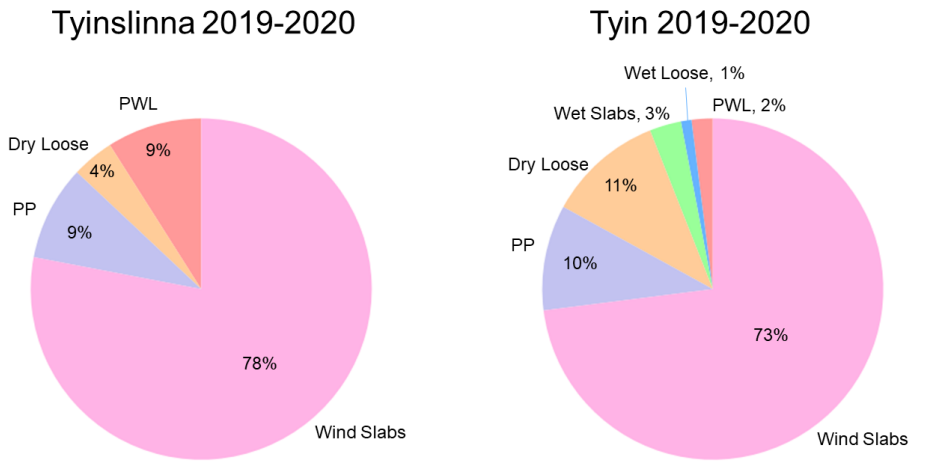

Figure 3.1.12: Distribution of the defined type of avalanche problem throughout winter season 2019-2020, data from Wyssen Norge AS [2020]. PP = Precipitation Particles, PWL = Persistent Weak Layer.

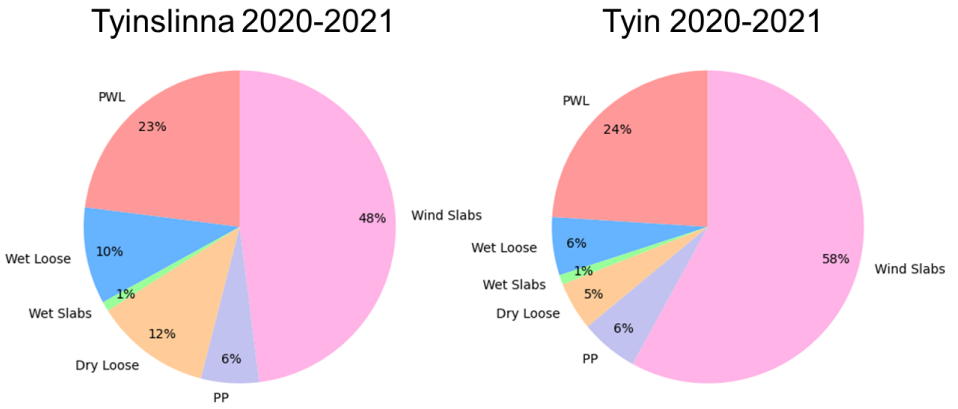

Figure 3.1.13: Distribution of the defined type of avalanche problem throughout winter season 2020-2021, data from Wyssen Norge AS [2021]. PP = Precipitation Particles, PWL = Persistent Weak Layer.

4

Data and Methods

4.1 Fieldwork

4.1.1 Snow Cover Surveys

Snow cover surveys were conducted by the author in the period 13-21 February to monitor the development of the snowpack at the plateau close to the snowdrift sensor FC4 and the avalanche towers Støl 1 & 2, an area earlier presented in Figure 3.1.3 in Section 3.1. The main focus was on assessing the amount of available snow for wind transport. This plateau acts like a large catchment area for snowdrift. Thus, the snow cover surveys focused on the upper part of the snowcover, and on the properties related to whether the snow was prone to wind erosion or not - such as snow type, hardness, and density. The weather- and snowpack development was monitored throughout the fieldwork period, and is summarized in the Results Section 5.3.

The snow cover surveys were performed using the systematic snow cover diagnosis approach by Kronthaler & Zenke [2006] - a methodology adapted to a norwegian system by the national avalanche warning service Varsom [NVE, 2011, 2013]. In the snow profiles, different parameters were measured such as the air temperature, temperature profile inside the snow, snow layering, hardness, grain types & sizes, and humidity. Following paragraphs go into more detailed methodology for each parameter.

Hardness by Hand Testing

The hardness corresponds to the first "object" that can be pressed into the snow layer (pressure must correspond to a weight of max. 5 kg). The hand test was carried out wearing gloves. The hardness levels is as described in Table 4.1.1. Figure 4.1.1 shows the snow pit wall after a conducted hand test.

Table 4.1.1: Hardness index, a method by Kronthaler & Zenke [2006], applied in the Norwegian avalanche warning service [NVE, 2011].

Code	Hand test
F	Fist
4F	Four fingers
1F	One finger
P	Pen
K	Knife
I	Ice, too hard for knife

Figure 4.1.1: The author carrying out a snow cover survey on wind-compacted snow at the plateau above Tyinstølen. The snow pit wall shows countours from a conducted hand test. Picture taken by field assistant nr. 1 of 2: Fabrice Kaltenrieder

Density Measurements

The density of the snow was measured on the wind packed snow, with a wedge shaped density cutter - manufactured by Snowmetrics in the USA. The cutter consists of a snow container and a flat cutter (Fig. 4.1.2). A sample for each snow layer were obtained and weighed by a hanging spring scale (Fig. 4.1.3). As the volume of the snow container was known (10 x 10 x 20cm) the density could be calculated and given in kg/m^3.

Density cutters tend to underestimate between 0-9%, especially those of a smaller volume [Proksch et al., 2016; Hao et al., 2021]. Everything under 11% is considered 'accepted practice' [Conger & McClung, 2009].

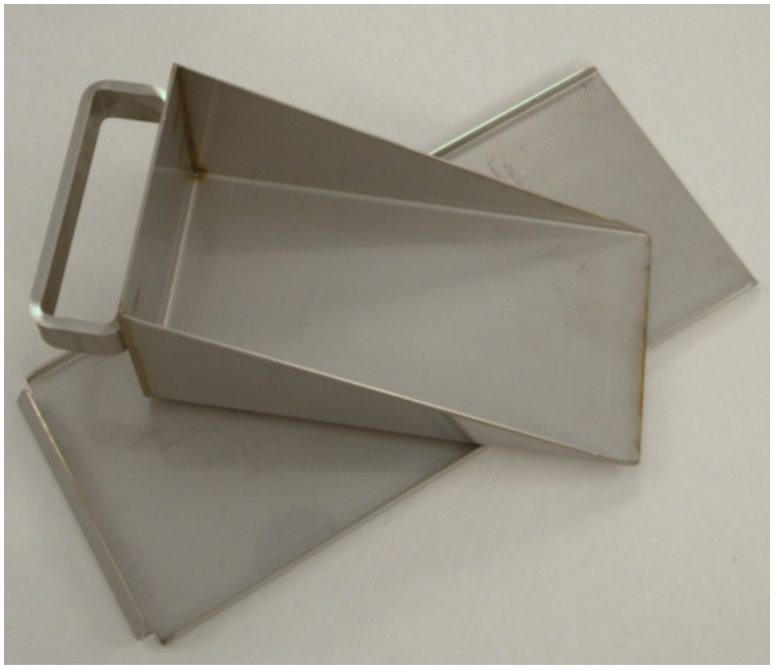

Figure 4.1.2: The parts of a wedge shaped density cutter: a snow container and a flat cutter. Made by the Snow Research Associates and manufactured by Snowmetrics in the USA [Conger & McClung, 2009].

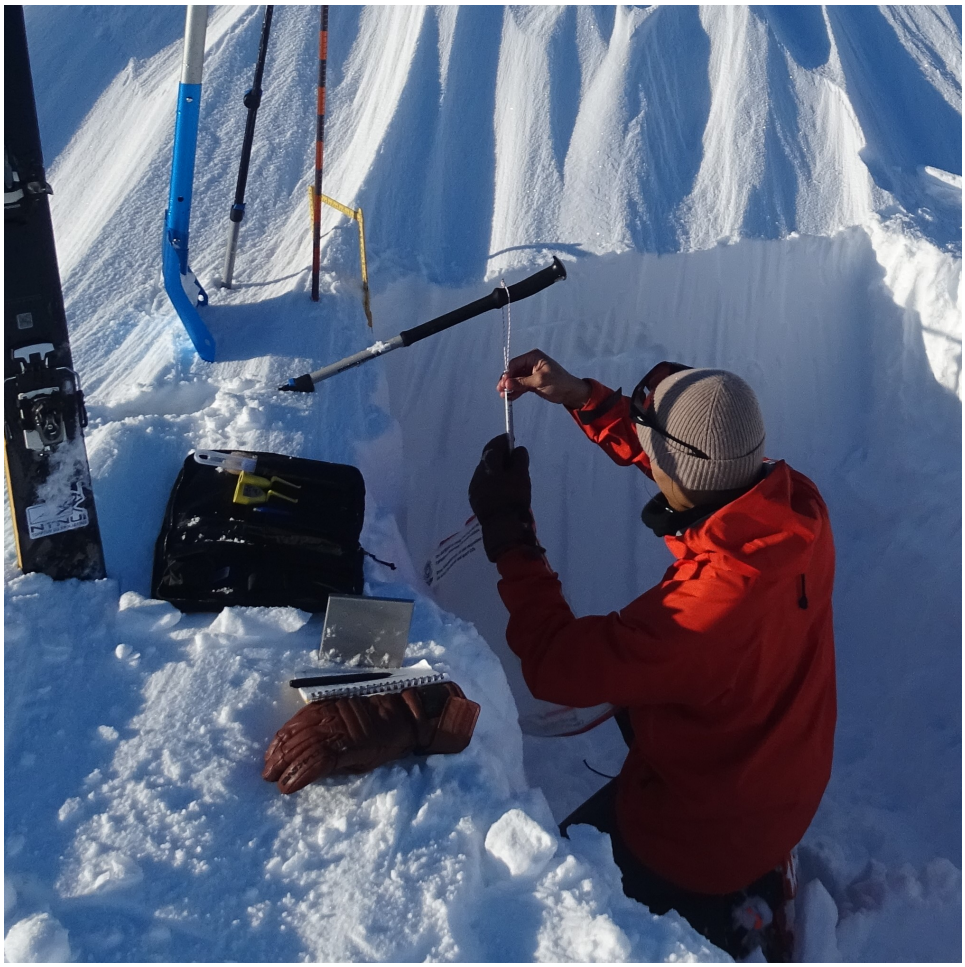

Figure 4.1.3: The author weighing a sample of snow with a hanging spring scale. Snow collected from a wedge-shaped density cutter. Picture taken by field assistant nr. 1 of 2: Fabrice Kaltenrieder

Grain Shapes and Sizes

Grain shapes were identified for each individual layer. All the main classes (and some subclasses) for the grain types that are used in this study are summarized in Table 2.1.1 in Chapter 2 - Theoretical Background.

The grain sizes were noted as accurately as possible, using a grid plate and magnifying glass. The average size were used, based on the longest axis of the snow crystal.

Snow Humidity

The water content of the snow surface were estimated from point measurements using a "hand" squeeze test as from the method by Techel & Pielmeier [2011]. The classification terms used are summarized in Table 4.1.2. The Liquid Water Content (LWC) is used to describe the snow humidity in the snow profile diagrams.

Table 4.1.2: LWC of the snow, a method by Techel & Pielmeier [2011] applied in the Norwegian avalanche warning service [NVE, 2011].

Code	Term	Description
D	Dry	Loose snow without the ability to hold together when making a snowball
M	Moist	The snow binds well together when making a snowball
W	Wet	The snow binds well and feels wet, but it is not possible to press water out of the snow ball
V	Very wet	It is possible to press water out of the snowball
S	Slush	Water flows out of the snow and the snow does not bind together

Stability Tests

Stability tests on the snow were conducted when the goal of the survey was to detect the probability of release. This was relevant for the local avalanche warning. An Extended Compression Test (ECT) were in these cases conducted, providing information on the initiation and propagation of possible fractures. A schematic overview of the desired snowpit is given in Figure 4.1.4.

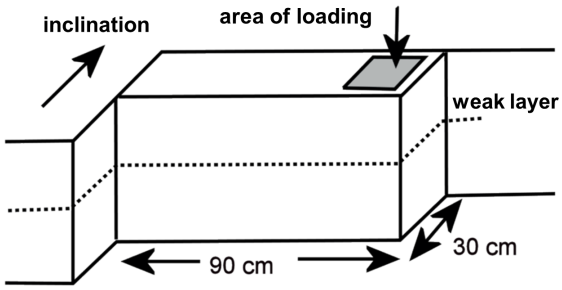

Figure 4.1.4: ECT - Extended Compression Test. Schematic sketch, edited figure from NVE [2011]

The procedure included isolating a column (90x30cm), which goes vertically

deep enough to include weak layers. Snow profile diagrams denoting Ground (GND) suggest that the column was dug all the way down to the ground. A shovel was laid on the loading area, and the observer's hand was used to strike on the shovel (falling with its own weight against the shovel) and were performed like this:

- 10 strikes initiated from the wrist
- 10 strikes initiated from the elbow joint
- 10 strikes initiated from the shoulder joint

The number of strikes needed to obtain a first fracture were noted. If that fracture did not propagate throughout the column, the striking continued, and the strikes needed until it breaks were noted. The depth of the break were also noted. The results were classified as shown in Table 4.1.3.

Table 4.1.3: ECT classification table from NVE [2011], a methodology adapted from Kronthaler & Zenke [2006] and applied in the Norwegian avalanche warning service.

Code	Description
ECTPV	Fracture propagates across the entire column upon release (by force).
ECTP##	Fracture propagates across the entire column after ## number of strikes OR small fracture after ## number of strikes and then propagates over the entire column after ##+1 number of strikes. The maximum number of strikes is 30.
ECTN##	Small fracture after ## number of strikes, but does not propagate after ## nor ##+1 number of strikes.
ECTX	No fractures during the test after 30 strikes.

Figures 4.1.5 & 4.1.6 show the author conducting an ECT-test in collaboration with Skred AS on one of their weekly snow cover surveys.

Figure 4.1.5: Shaping the snow pit to conduct an ECT-test, in collaboration with Skred AS at one of their weekly snow cover surveys. Picture taken by the author's field assistant nr. 2 of 2: Vilde Edvardsen Hansen.

Figure 4.1.6: The author carrying out an ECT-test. Picture taken by the author's field assistant nr. 2 of 2: Vilde Edvardsen Hansen.

4.1.2 Snow Profiles from the Forecasting Group

Weekly snow profiles from the forecasting group at Skred AS - and occasionally from the local Varsom observer - are a part of the data foundation for both the local avalanche warning, and also for this study. The author collaborated with the two weekly surveys in the fieldwork-period 13-21 February. The weekly surveys from the whole winter season are archived in Varsom Regobs [2024] - which is a platform for registering of snow observations, provided by the national avalanche warning service Varsom. The locations of these surveys are shown in Figure 4.1.7.

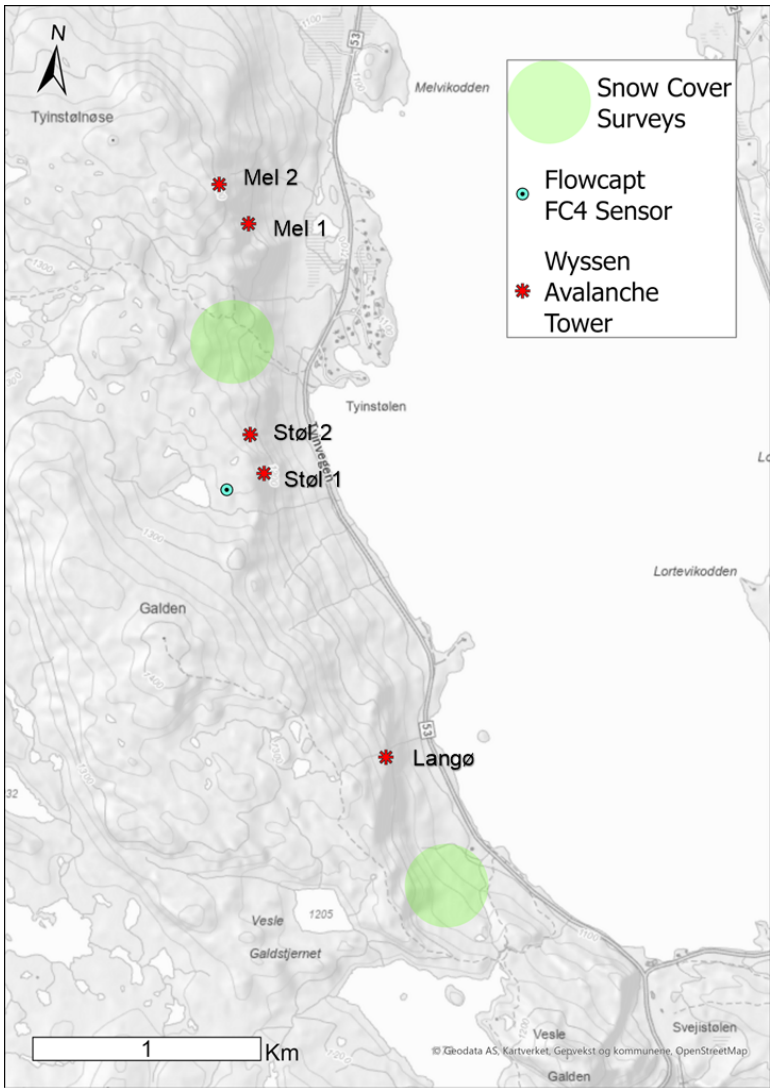

Figure 4.1.7: Approximate areas (green circles) where the weekly snow cover surveys by the forecasting group are most often carried out.

4.2 LiDAR Scans

Airborne LiDAR-scans from a Remotely Piloted Aircraft System (RPAS) were conducted by Solbakken, E. from the NPRA in Bergen. The NPRA is currently working on method development on the use of LiDARs on a Unmanned Aircraft System (UAS) to support avalanche monitoring [Statens Vegvesen, 2021]. Flying remote missions without direct involvement with observers is by the NPRA considered important to continue to gain experience and track potential issues impacting the usability in the future - especially related to their research project GEOSFAIR.

A RTK-drone (DJI Matrice mounted with LiDAR and a GPS) was used to carry out five different scans in the period 13-21 February: the 15th, 17th, 19th, 21th before the avalanche control, and on the 21th after the avalanche control. An overview of the dataset is visualized in Figure 4.2.1.

The data from the surveys were in raw format (LAS-files), which were subsequently converted into processed data (TIFF-files) for use in a Geographic Information System (GIS), mainly ArcGIS Pro. The accuracy of each scan is initially ±5-15cm based on the properties of the flight route and an altitude of 80 meters. One very important aspect of the LiDAR-data is that it exclusively compares data from similar measurements with the same flight pattern and height. Then, when assessing the height change between two different measurements, it is reasonable to assume an accuracy of ±10-30cm. If absolute snow height were to be assessed (through subtracting a DEM), this would give an additional inaccuracy. The relative precision (surface change) between measurements is the focus of this study rather than absolute precision (change between absolute snow height).

The processed LiDAR-data (TIFF-files) are the basis for further analysis, both through different functions in ArcGIS Pro as well as through coding in the Python language. In the case of Python coding, the LiDAR-data is converted into ASCII-files - in most cases delimited by polygons in ArcGIS Pro - and further processed through Python libraries such as Numpy, Matplotlib, and Pandas.

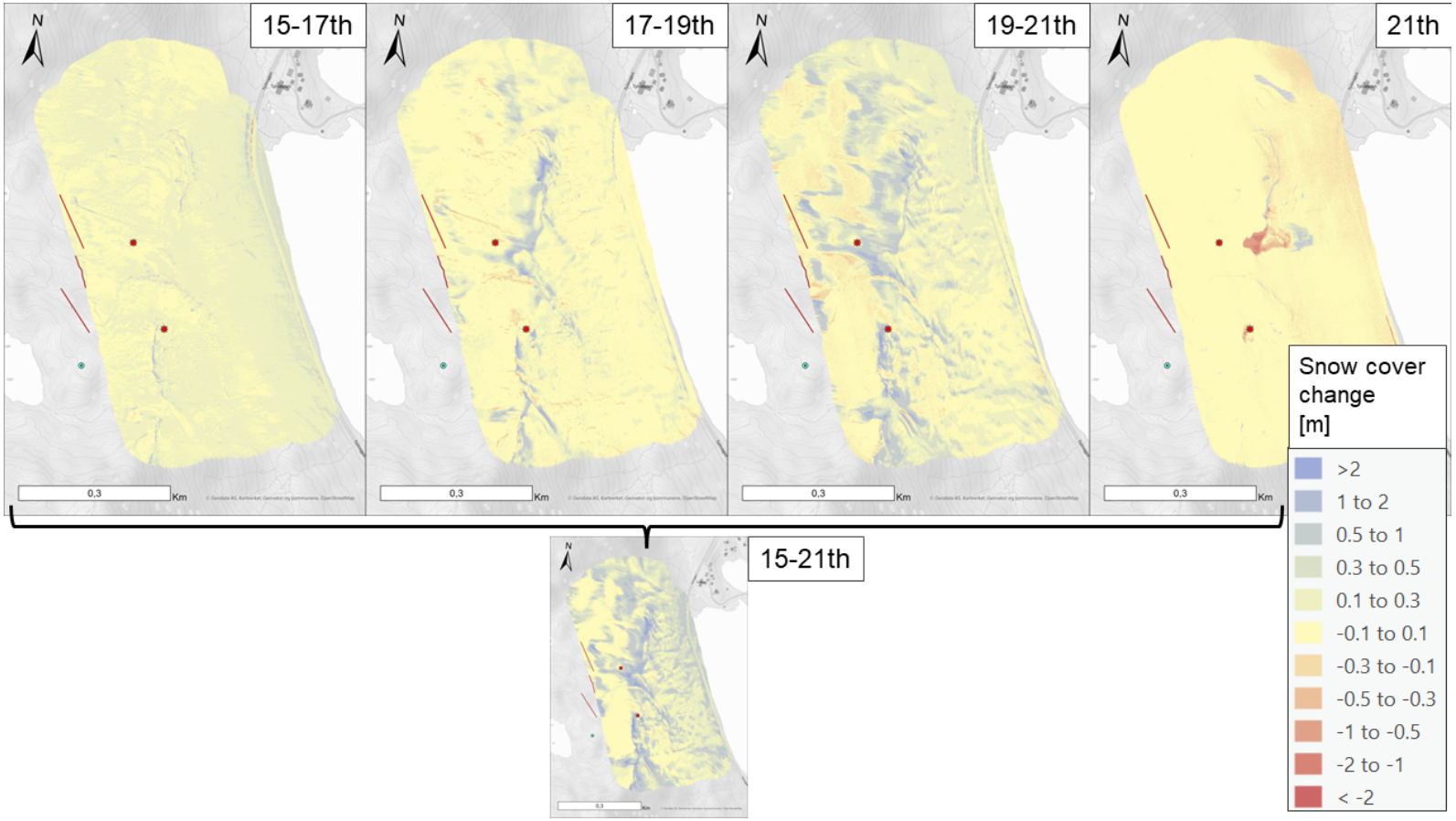

Figure 4.2.1: The five LiDAR-scans visualized through snow cover change in intervals. Avalanche towers Støl 1 & 2 marked as red stars, the snowdrift sensor FC4 as cyan circle, and snow fences as red lines. The LiDAR scans made on the 21th were conducted both before and after an avalanche control. Dates are through February 2023.

4.2.1 Snow Surface Change Calculation and Corrections for Additional Precipitation

The measured surface changes of the six PRAs (PRAs presented in Fig. 5.0.1 in Results Section 5) were derived between each LiDAR-measurement for each of the intervals: 15-17th, 17-19th, and 19-21st. This was done by importing the LiDAR-data into ArcGIS Pro and delineating the raster files for each polygons defining the PRAs. These clippings were converted into an ASCII-file for analysis in Python. Here, the difference between measurements were calculated and plotted (example shown in Fig. 4.2.2). The mean snow surface change was extracted for each PRA. Data for each PRA is summarized in Table A.1 in Appendix A.

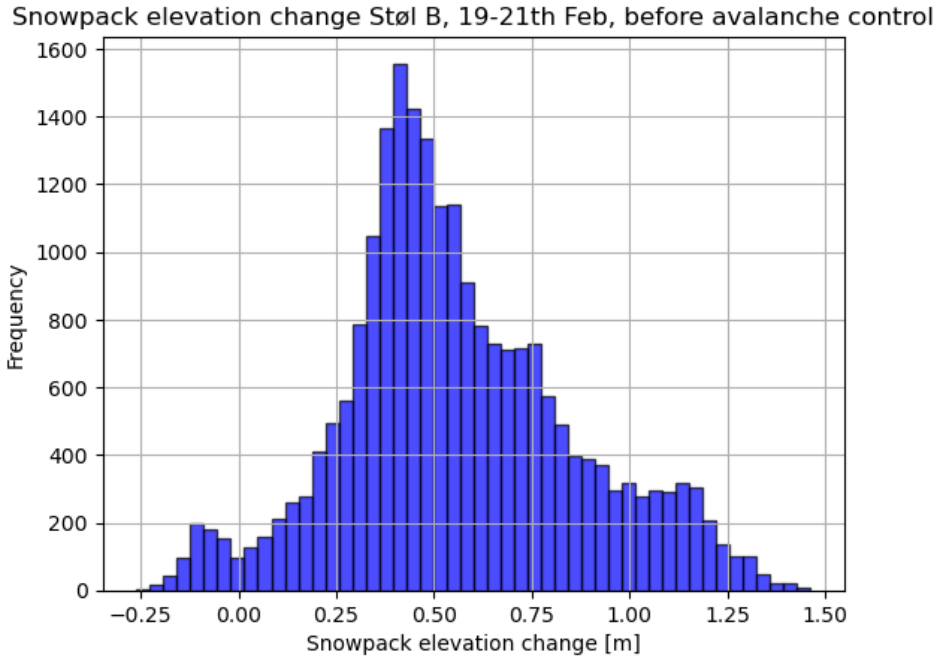

Figure 4.2.2: Measured snow surface change at Støl B, by LiDAR-scans 19th and the 21st.

Corrections regarding additional precipitation were done for each of the snow surface change measurement intervals. This was done by initially summing up precipitation values (FV53 Tyinosen, every 10 min) between each time period between LiDAR-scans (time stamps of minute-precision).

By using the defined rule of thumb (as mentioned in Section 2.1.1) regarding conversion of precipitation measurements [mm] into the estimated snow height [cm] (1mm→1cm snow), this value was subsequently subtracted from the measured mean surface change value - and thus corrected for additional precipitation.

4.2.2 Volume Change Calculation and Corrections for Additional Precipitation

The measured volume changes of the six PRAs (PRAs presented in Fig. 5.0.1 in Results Section 5), were derived between each LiDAR-measurement - for each of the intervals: 15-17th, 17-19th, and 19-21st. This was done by importing the LiDAR-data into ArcGIS Pro and delineating the raster files for each polygons defining the PRAs. The volume change was derived for each of the PRAs for each of the time intervals. Data for each PRA are summarized in Table A.2 in Appendix A.

Corrections regarding additional precipitation were done for each of the measured volume changes. This was done by initially summing up precipitation values (FV53 Tyinosen, every 10 min) between each time period between LiDAR-scans (time stamps of minute-precision).

The mentioned rule of thumb (Section 2.1.1) - which states that 1 mm of precipitation (Fresh Snow Water Equivalent (FSW)) equals to 1 cm of snow - were used to estimate the mean snow surface change [m] based on precipitation measurements. This value was subsequently multiplied with the area [m^2] of the PRA - and subtracted from the measured volume change, and thus corrected for additional precipitation. This calculation is presented in Equation 4.1.

$$\Delta V - (A \cdot \sum FSW) = \Delta V_{corr} \tag{4.1}$$

where

- ΔV is the measured volume change [m^3] from LiDAR-scans and GIS-analysis.
- A is the area [m^2] of the polygon defining the PRA
- FSW is the Fresh Snow Water Equivalent (FSW) [m]
- ΔV_{corr} is the volume change [m^3] corrected for additional precipitation

4.3 Weather Stations

Figure 4.3.1 shows an overview of the locations of the four weather stations that are accounted for in this study. Information on each weather station follows.

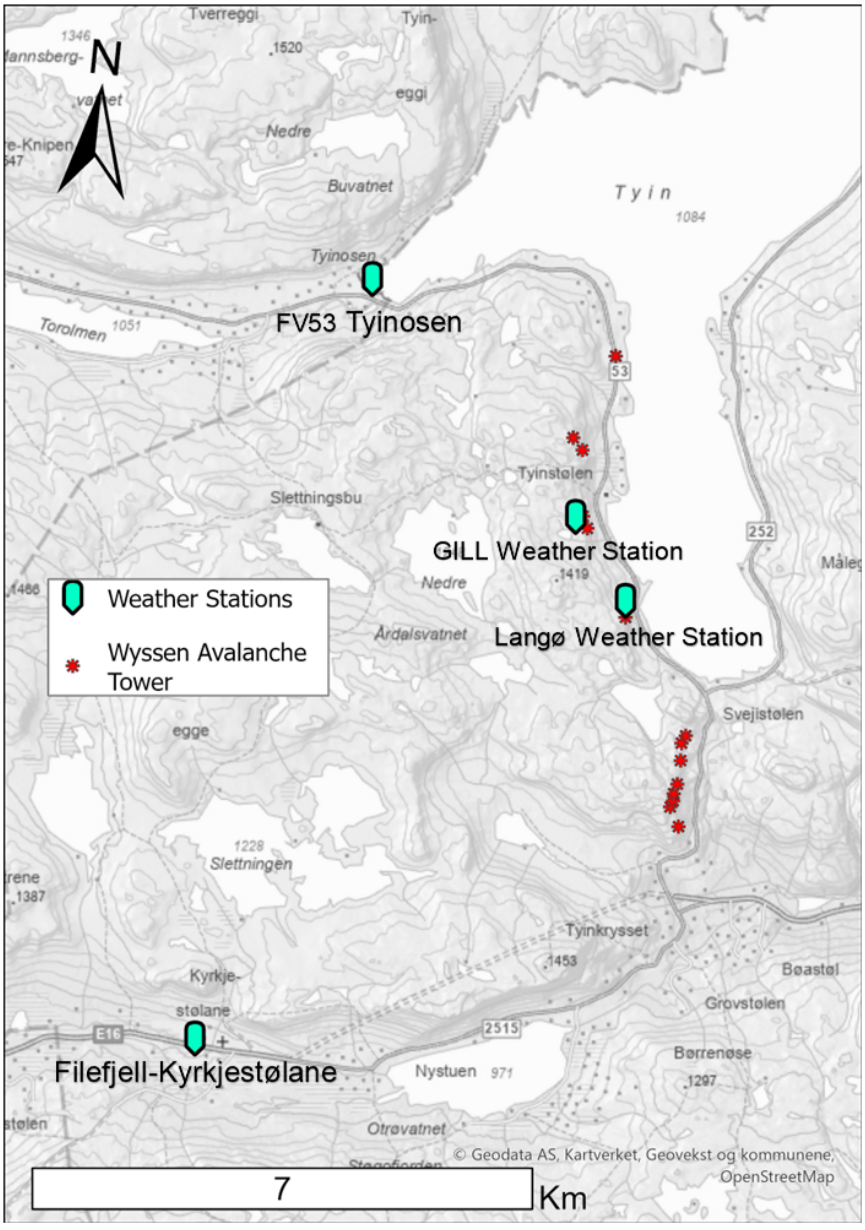

Figure 4.3.1: Overview of the locations of the four weather stations accounted for in this study. The GILL Weather Station is mounted on top of the snowdrift sensor FC4 at the fieldwork area. The Langø Weather Station is attached to the Langø Avalanche tower.

FV53 Tyinosen

- Station: FV53 TYINOSEN
- Station ID: 54815
- Data: Precipitation (10min), wind speed & direction (10min), temperature (10min), humidity (10min)
- Data owner: Norwegian Public Road Administration (NPRA)
- m.a.s.l.: 1080

The location is 2,9km north of the FC4-sensor. With regards to precipitation and temperature measurements, this station is given the greatest focus due to its placement in the same regional climate and altitude.

Filefjell-Kyrkjestølane

- Station: Filefjell-Kyrkjestølane
- Station ID: SN54710
- Data: Precipitation (10min), wind speed & direction (10min), temperature (1h), snowdepth (1h), humidity (24h), radiation (1min),
- Data owner: Norwegian Meteorological Institute (MET)
- m.a.s.l.: 956

This weather station is located 9 km SW from the area of interest by Tyinstølen. It's precipitation measurements corresponded well with the weather station FV53 Tyinosen - which is closer to Tyinstølen. But due to its distal placement for the relevant study area, none of the measurements are used in this study.

Noteworthy, if the FC4-sensor sometime in the future will be is used in a similar way as Lehning & Fierz [2008] by verifying snowdrift in relation to a physical snow cover model such as SNOWPACK, then this weather station can be relevant for model input on wind, air temperature, relative humidity, snow depth, surface temperature, and reflected short-wave radiation.

GILL Weather Station

- Station: "MaxiMet GMX 500 Compact Weather Station" from Gill Instruments, mounted on top of the FC4-installation
- Data (every 10th minute): Windspeed- and direction
- Data owner: Skred AS, the Norwegian Public Road Administration (NPRA), Innlandet County
- m.a.s.l.: 1258

Located in the fieldwork area on the plateau above Tyinstølen. The plateau

is wide and open and is a huge snowdrift catchment area. Thus, this weather station records good data on the general weather situation in the region. The data is imported from the open source observability platform Grafana, where access must be authorized.

Langø Wyssen Avalanche Tower

- Station: A weather station mounted on the Langø Wyssen Avalanche Tower
- Data (milliseconds): Temperature, windspeed- and direction, precipitation
- Data owner: Wyssen Norge AS
- m.a.s.l.: 1180

Experiences from Wyssen Norge AS [2020, 2021] show precipitation measurements of varying quality; records rain well, but snow combined with wind less good. Wind and temperature measurements are however considered good. For this study, no data from this station are used, as wind data is derived from the GILL Weather station, and precipitation measurements are assumed to be of higher quality from the FV53 Tyinosen weather station.

4.4 FlowCapt 4

The snowdrift data from the snowdrift sensor FC4 is originally in g/m^2 per 10 min but are mostly manipulated as a cumulative value for this study - where the specified zero/start point varies based the desired interval. The data is imported from the open source observability platform Grafana, where access must be authorized. Figure 4.4.1 shows the measured snowdrift plotted together with Daily Rain Rate (DRR) from the Filefjell-Kyrkjestølane weather station during the winter season 2022/23.

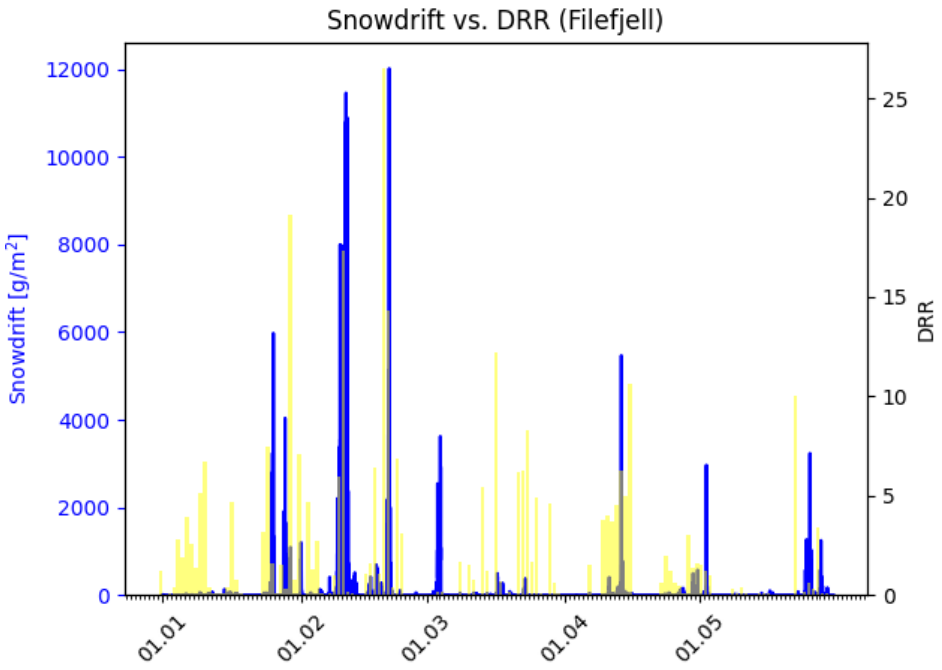

Figure 4.4.1: Measured snowdrift from FC4, and Daily Rain Rate (DRR) [mm] from Filefjell-Kyrkjestølane weather station. Data throughout winter season 2022-2023.

4.4.1 Extrapolation of Snowdrift Data for Each PRA

Manipulation of the point data measurements from the FC4 were done, with the purpose to explore a method to normalize the data by taking into account the difference in sizes of the defined PRAs (Fig. 5.0.1 in Results Section 5) - and to uncover whether each PRA showed a tendency of same pattern in their respective correlation between the measured snowdrift and the measured volume- and surface change.

This was done by extrapolating the accumulated FC4-data [g/m^2] to an estimated length of a theoretical cross-section for each PRA, as presented in Equation 4.2 and visualized in Figures 4.4.2 and 4.4.3.

$$Q \cdot L = M \tag{4.2}$$

where

Q is the measured snow mass flux from the FC4-sensor [g/m^2], a cumulated value for a custom defined period.
L is the length of a theoretical cross-section with 1 m height [m^2] fitted to the same length of the diameter of a PRA normal to the snowdrift direction.
M is the total snow particle mass transport [g] during the defined period.

In this study, the resulting total snow particle mass transport M, is converted to [kg] by dividing by 1000.

The defined PRAs as presented in Figures 4.4.2 & 4.4.3, as well as in the Results Section 5, originates from the PRAs earlier presented in Figure 3.1.2 (polygons used by Skred AS [2022] in RAMMS modeling), but are for this study adjusted based on LiDAR-observations during fieldwork - to fit the observed terrain slope and spatial distribution of snowdrift. All in accordance to NVE's guidelines on spatially delineating PRAs NVE [2020a].

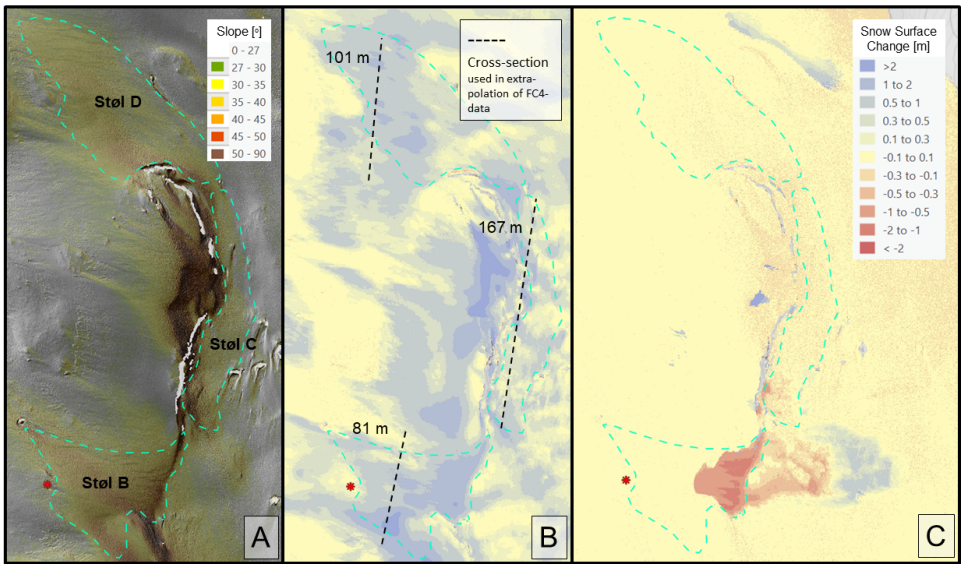

Figure 4.4.2: A) Three of the defined PRAs presented in Results Section 5. Raster data from LiDAR-scan 21.02.23. **B)** The chosen cross-sections for extrapolation of FC4-data. Raster data from LiDAR-scans 15-21st Feb. **C)** Snow surface change after avalanche control 21.02.23.

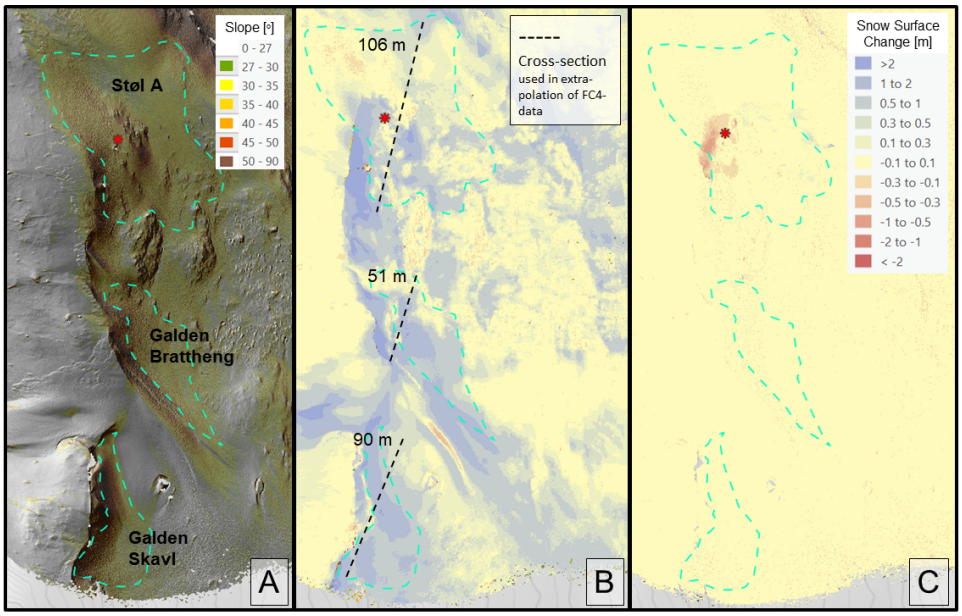

Figure 4.4.3: A) Three of the defined PRAs presented in Results Section 5. Raster data from LiDAR-scan 21.02.23. **B)** The chosen cross-sections for extrapolation of FC4-data. Raster data from LiDAR-scans 15-21st Feb. **C)** Snow surface change after avalanche control 21.02.23.

/5

Results

The in-situ monitoring of the snow cover development through snow pit surveys at the snowdrift catchment plateau revealed that the snow cover was close to static, with hard wind-/melt crust (depending on altitude) covering the whole plateau, and local patches of wind slabs (pen-knife hardness) on top of this crust in lee-areas towards the east - covering approx. 15-20% of the plateau.

Hence, most of the additional snowfall during the fieldwork period 13-21 February was wind-transported along the hard snow cover and distributed in these local patches of wind slabs both at the plateau and in the Potential Release Areas (PRAs) (Fig. 5.0.1). A more detailed summary of the snowpack development is given in Section 5.3.

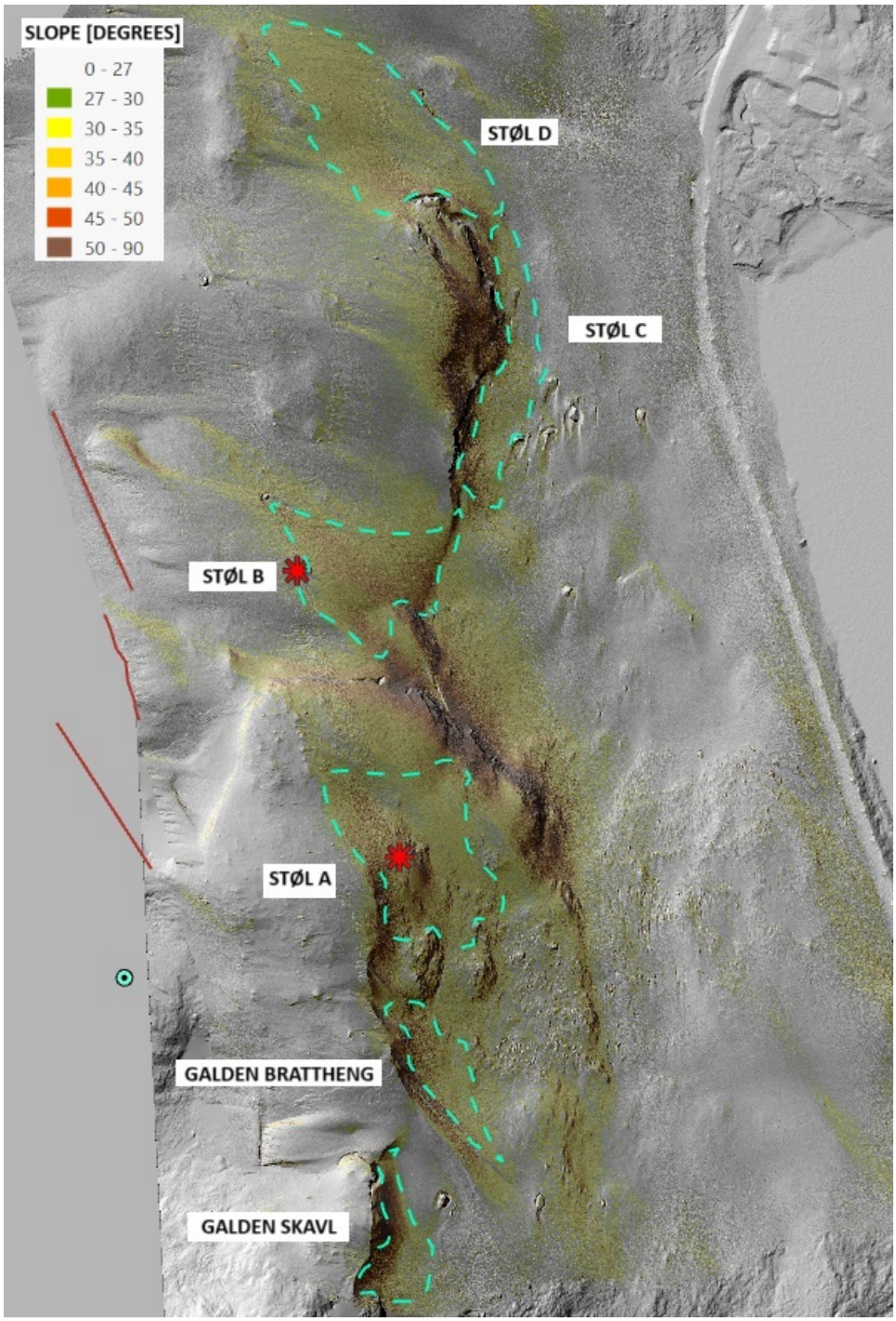

Figure 5.0.1: The Potential Release Areas (PRAs) defined in this study for further analysis - chosen based on the observed terrain development through LiDAR-scans as well as on guidelines for delineating PRAs by NVE [2020a]. Red lines are snow fences, cyan circle is the FlowCapt 4 (FC4), red stars are the avalanche towers Støl 1 and 2, related to PRAs Støl A and B, respectively. Raster data from LiDAR-scan 21 February.

Figure 5.0.2 shows an overview of the collected weather data during the field-work period 13-21 February - displaying measured snowdrift from the FlowCapt 4 (FC4), precipitation from FV53 Tyinosen Weather Station, and weather data from GILL Weather Station installed just above the FC4; wind speed & direction, and temperature. There was a storm event prior to 13 February, and avalanche control was conducted this day. Three storm event with winds from the west happened up to the last avalanche control 21 February.

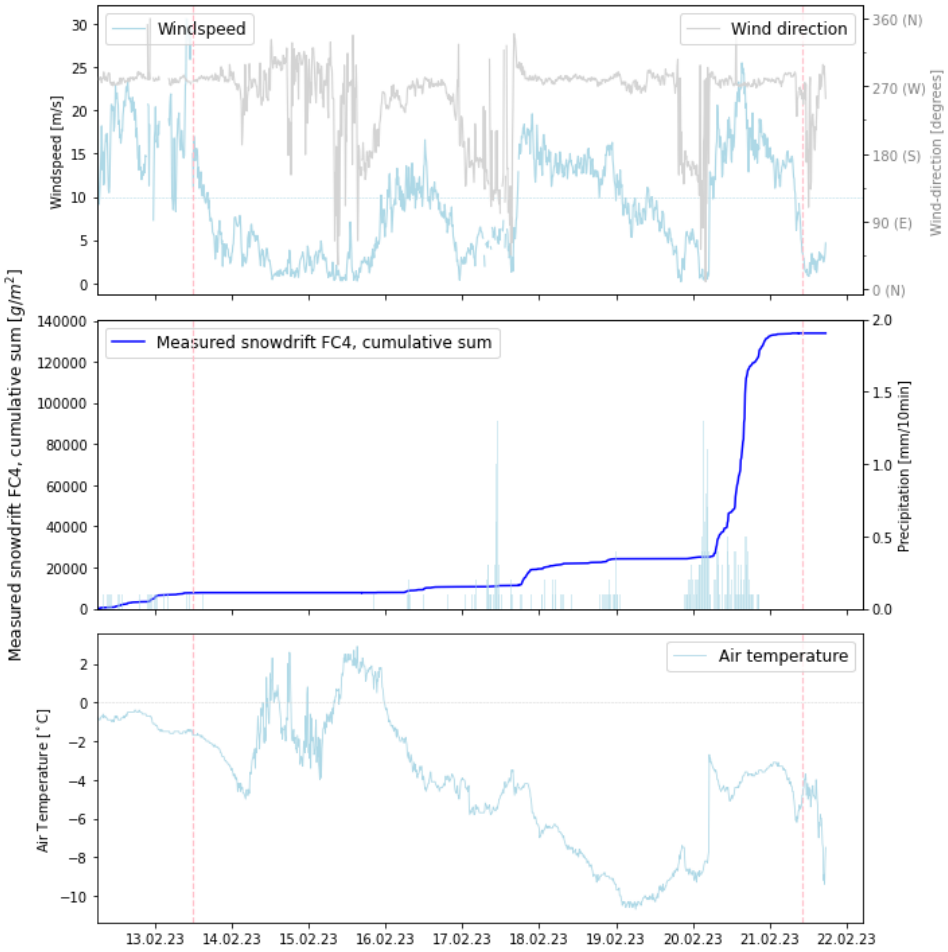

Figure 5.0.2: First subplot: Windspeed and direction. **Second subplot:** Measured snowdrift from FC4 (cumulative sum), and precipitation (FV53 Tyinosen Weather Station). **Third subplot:** Temperature (GILL Weather Station)
Red vertical lines indicate dates of avalanche control. A horizontal line at wind speed value 10 m/s is displayed to mark the experienced wind speed threshold value for registered snowdrift, as experienced throughout the winter season 22/23 [Skred AS, 2023b].

As the snowcover in the PRAs were laserscanned several times during fieldwork, a correlation could be made between the measured snowdrift and the deposited volume and mean surface change for each PRA. Figure 5.0.3 shows an example of such a plot for PRA Støl B. Similar plots for the other PRAs are presented in Appendix B.

Prior to these analyses, corrections regarding the additional snowfall were made for the measured volume and surface changes, as well as extrapolation of the measured snowdrift from the FC4-sensor to fit the estimated cross-section for each PRA - resulting in an estimate on the total weight of transported snow particles, which are given as a secondary X-axis in the following plots. The different methods for these corrections are summarized and explained in Sections 4.2.1, 4.2.2, and 4.4.1.

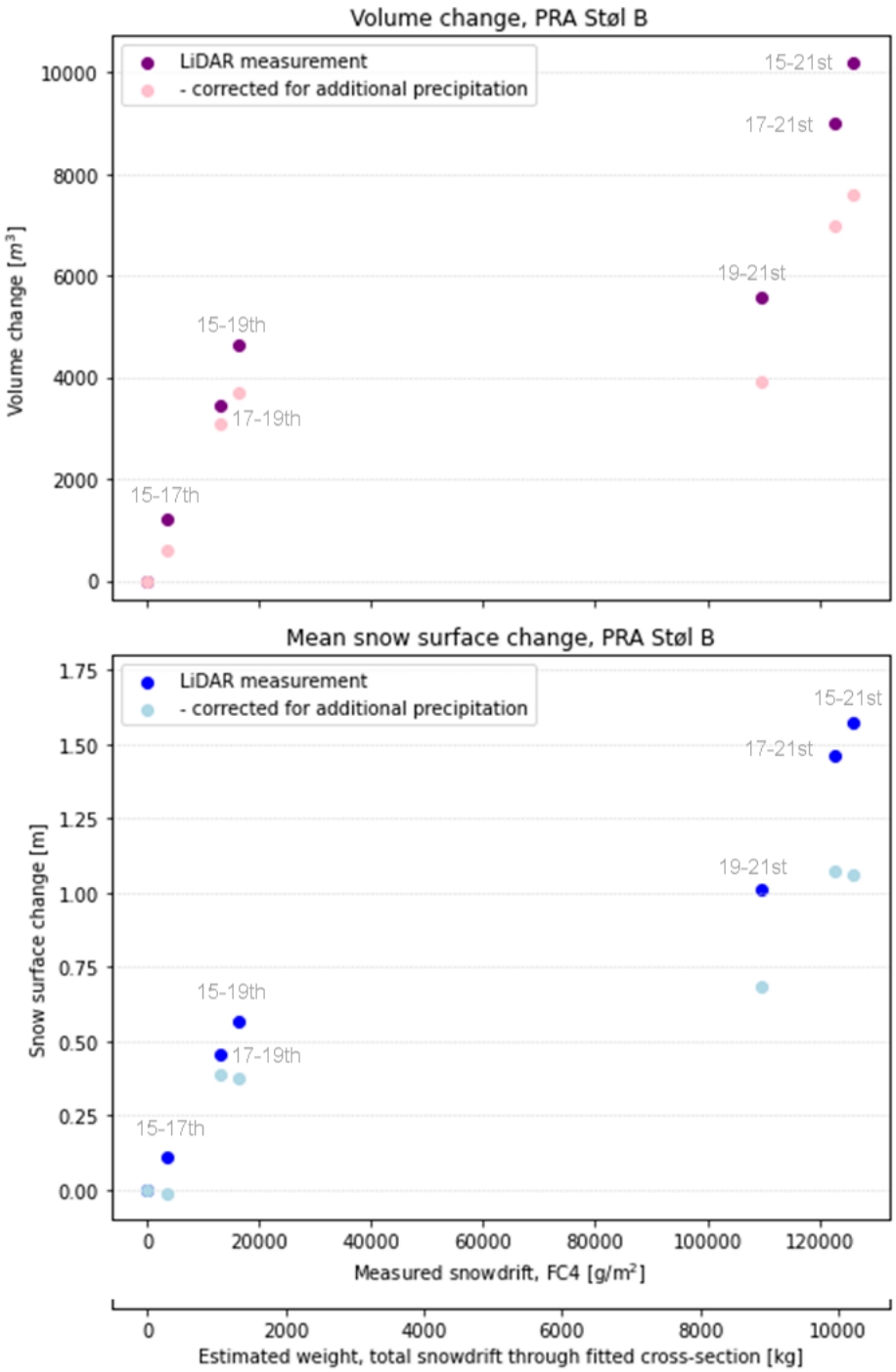

Figure 5.0.3: First subplot: Measured volume changes and corresponding corrections for additional precipitation. **Second subplot:** Measured mean snow surface changes and corresponding corrections for additional precipitation. Data from both subplots correspond to both x-axes presented at the bottom. All data values are presented in Tables A.1 & A.2 in Appendix A.

5.1 Extrapolation of FC4 data and Comparability between Potential Release Areas

To see whether each PRA's respective correlation between measured snowdrift and deposition were comparable with one another, the snowdrift data were extrapolated. This was done by converting the point measurement from the FC4 into a measurement based on a cross-section that was qualitatively fitted to the width of each PRA towards the snowdrift direction from the west. The method is described in Section 4.4.1.

Measured snowdrift values were therefore used as total mass of snowdrift [kg] - without it implicitly meaning the entire snowdrift amounts were deposited in the PRAs. Changes in volume and surface heights were plotted against the snowdrift for each PRA, which can be seen in Appendix B. A compilation of all the PRAs together is presented in Figure 5.1.1 – with corrections for additional snowfall presented as grey scatter points which show the shift to a lower value under each corresponding colored scatter point.

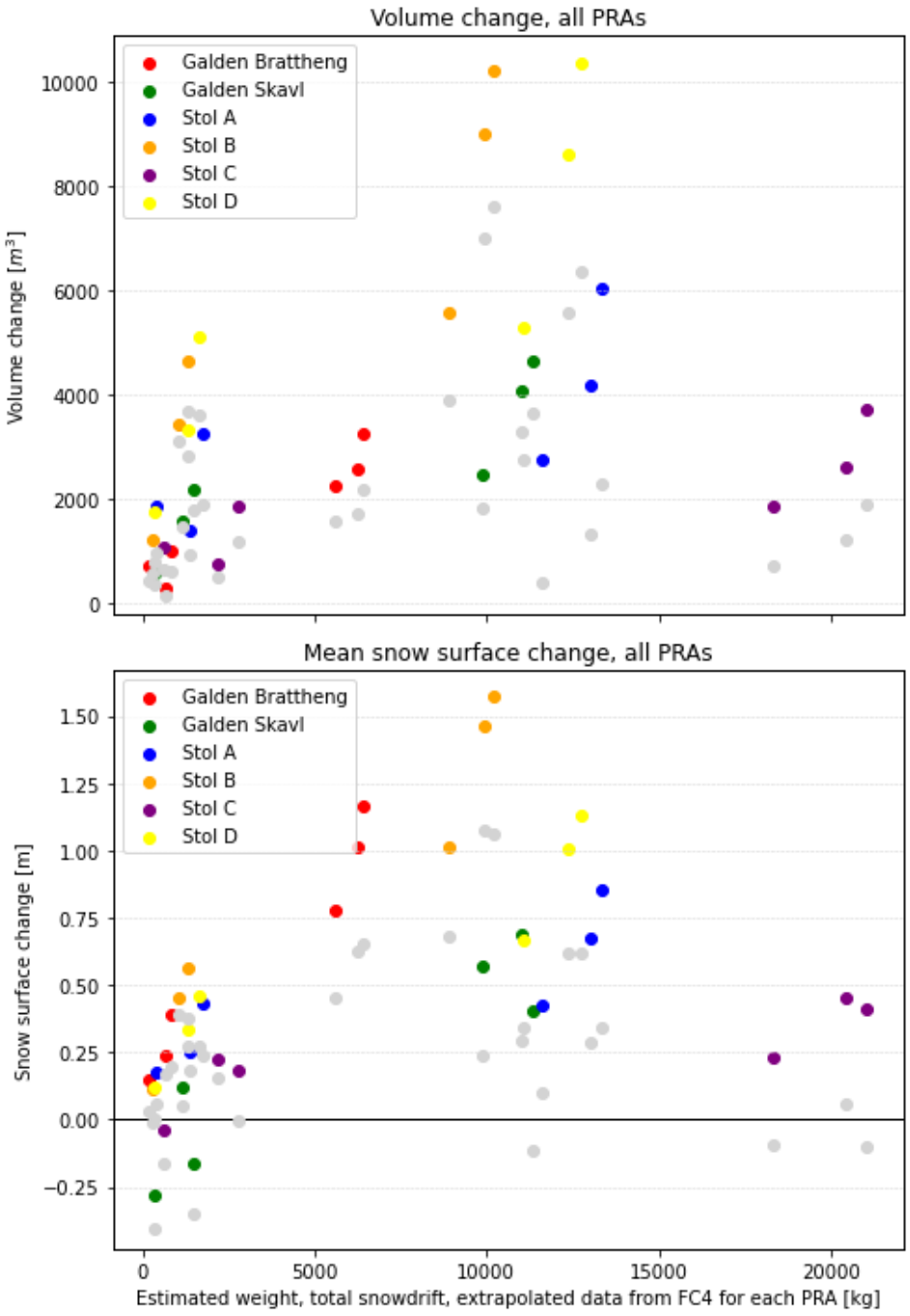

Figure 5.1.1: First subplot: Measured volume changes and corresponding corrections (grey dots) for additional precipitation. **Second subplot:** Measured mean snow surface changes and corresponding corrections (grey dots) for additional precipitation. Data values are presented in Tables A.1 & A.2 in Appendix A.

Figure 5.1.1 showed a huge spread across values (also for the corrected values) - as one would expect due to terrain variations of each PRA in terms of aspect, wind exposure, size, and curvature (convex/concave). By differentiating the six PRAs by their terrain curvature, the same plot is presented in Figure 5.1.2 - but with the PRAs that were considered concave/flat were highlighted.

The definitions of curvatures (convex/concave) and the application of it was not quantified but solely based on custom descriptions used for classification of each PRA:

- Convex areas have diverging terrain aspects downslope: *Galden Skavl, Støl A, and Støl C*
- Concave areas have converging terrain aspects downslope: *Galden Brattheng, Støl B, and Støl D*

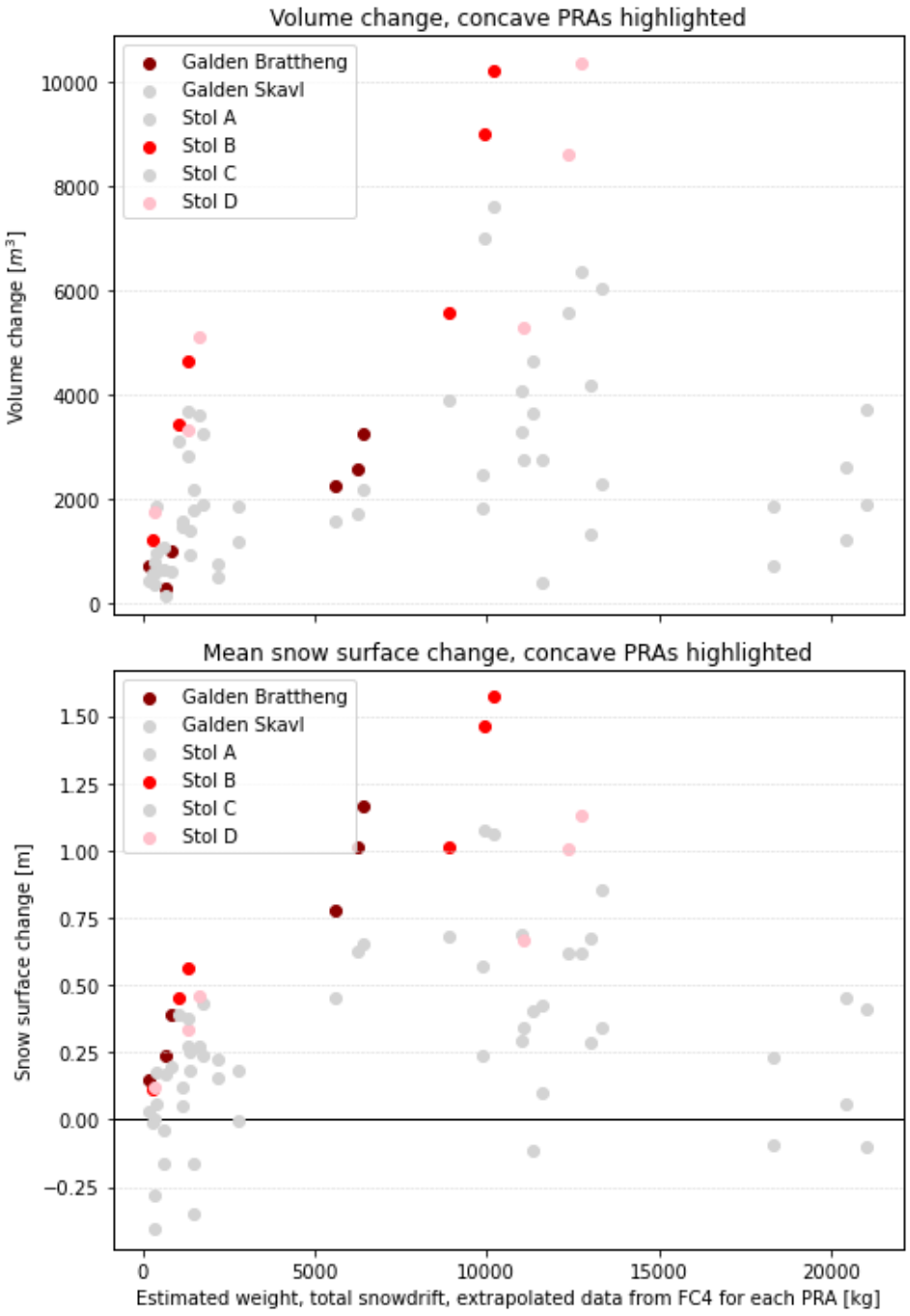

Figure 5.1.2: First subplot: Measured volume changes for the *concave/flat* PRAs highlighted as red nuances. Grey dots are the remaining datasets - including all corrections for additional precipitation. **Second subplot:** Measured mean snow surface changes for the *concave/flat* PRAs highlighted as red nuances. Grey dots are the remaining datasets - including all corrections for additional precipitation.

Figure 5.1.3 shows the same plot highlighting the concave areas - but with the corrected values, accounting for the additional precipitation.

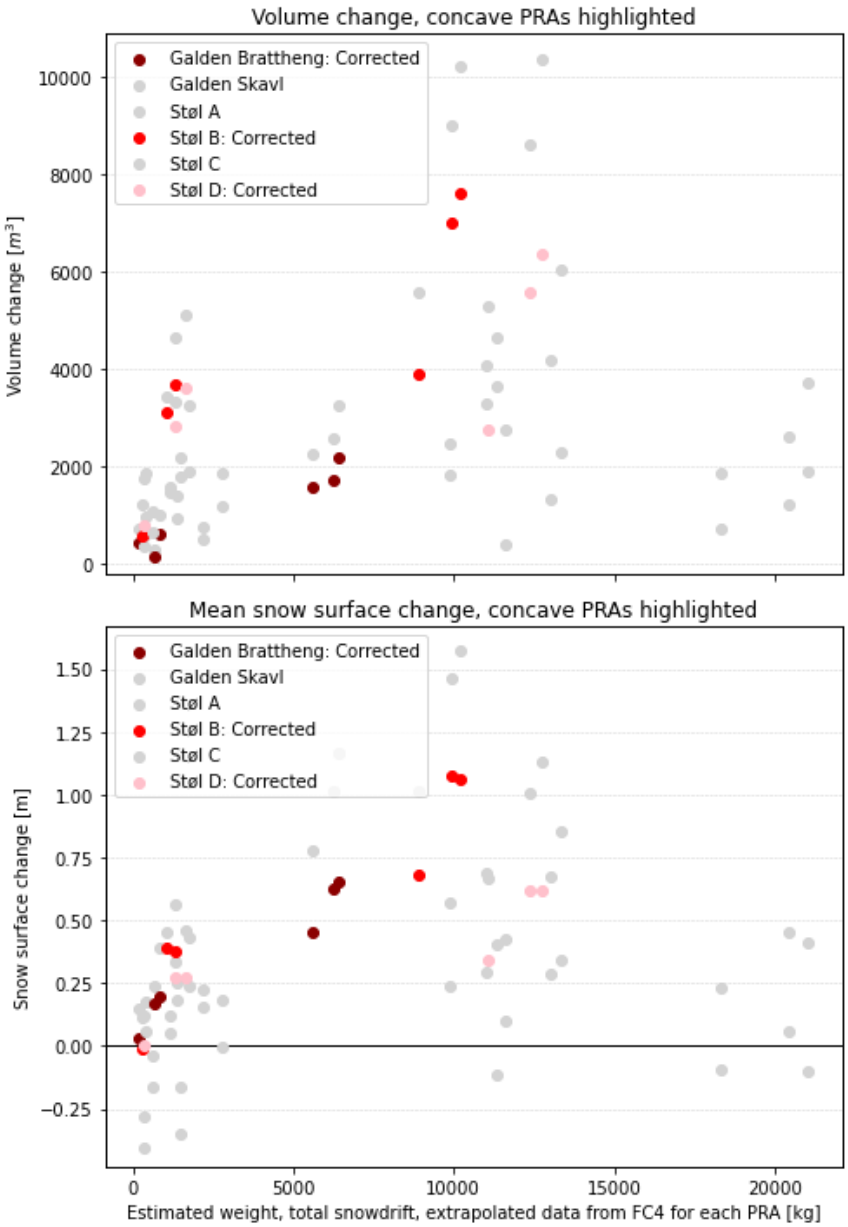

Figure 5.1.3: First subplot: Corrected volume changes for the *concave/flat* PRAs highlighted as red nuances. Grey dots are the remaining datasets - including all corrections for additional precipitation. **Second subplot:** Corrected mean snow surface changes for the *concave/flat* PRAs highlighted as red nuances. Grey dots are the remaining datasets - including all corrections for additional precipitation.

Figure 5.1.4 shows the same plot where the PRAs that were considered more convex were highlighted.

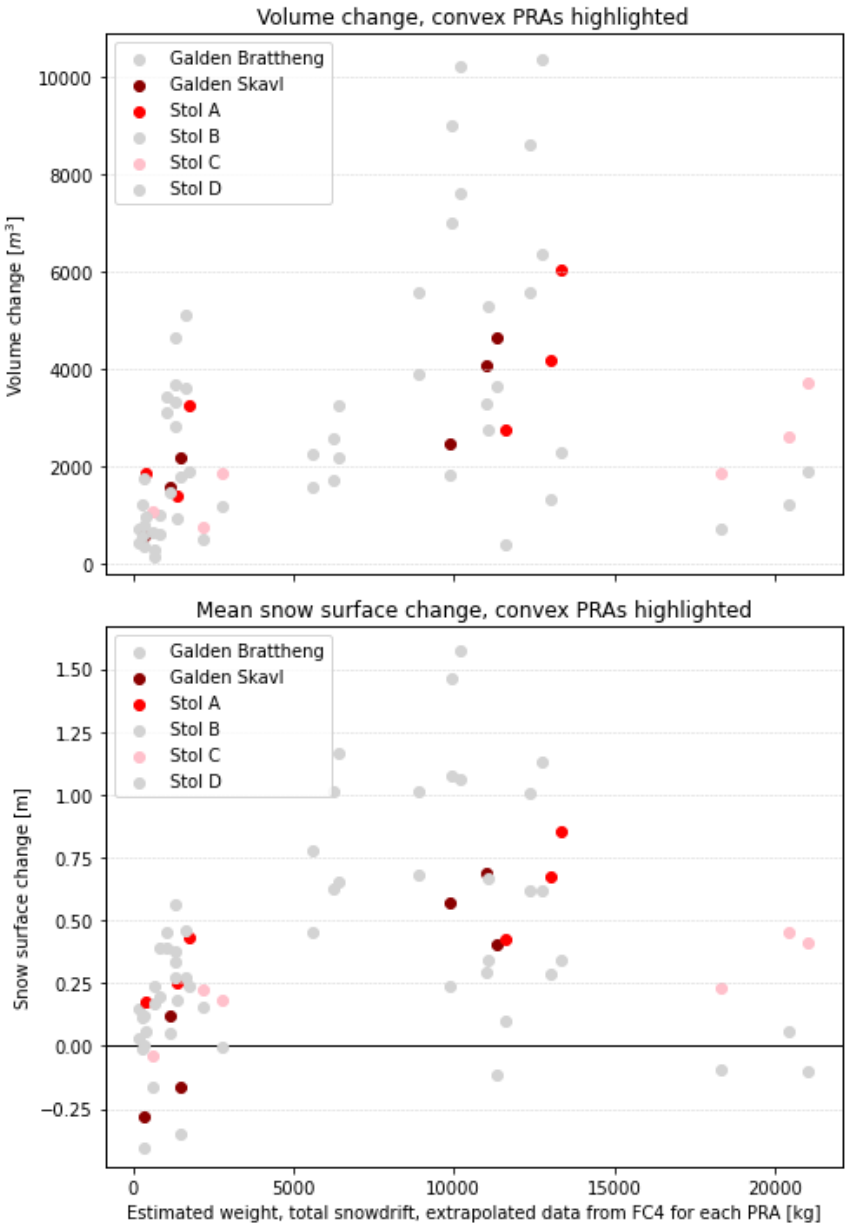

Figure 5.1.4: First subplot: Measured volume changes for the *convex* PRAs highlighted as red nuances. Grey dots are the remaining datasets - including all corrections for additional precipitation. **Second subplot:** Measured mean snow surface changes for the *convex* PRAs highlighted as red nuances. Grey dots are the remaining datasets - including all corrections for additional precipitation.

Figure 5.1.5 shows the same plot highlighting the convex areas - but with the corrected values, accounting for the additional precipitation.

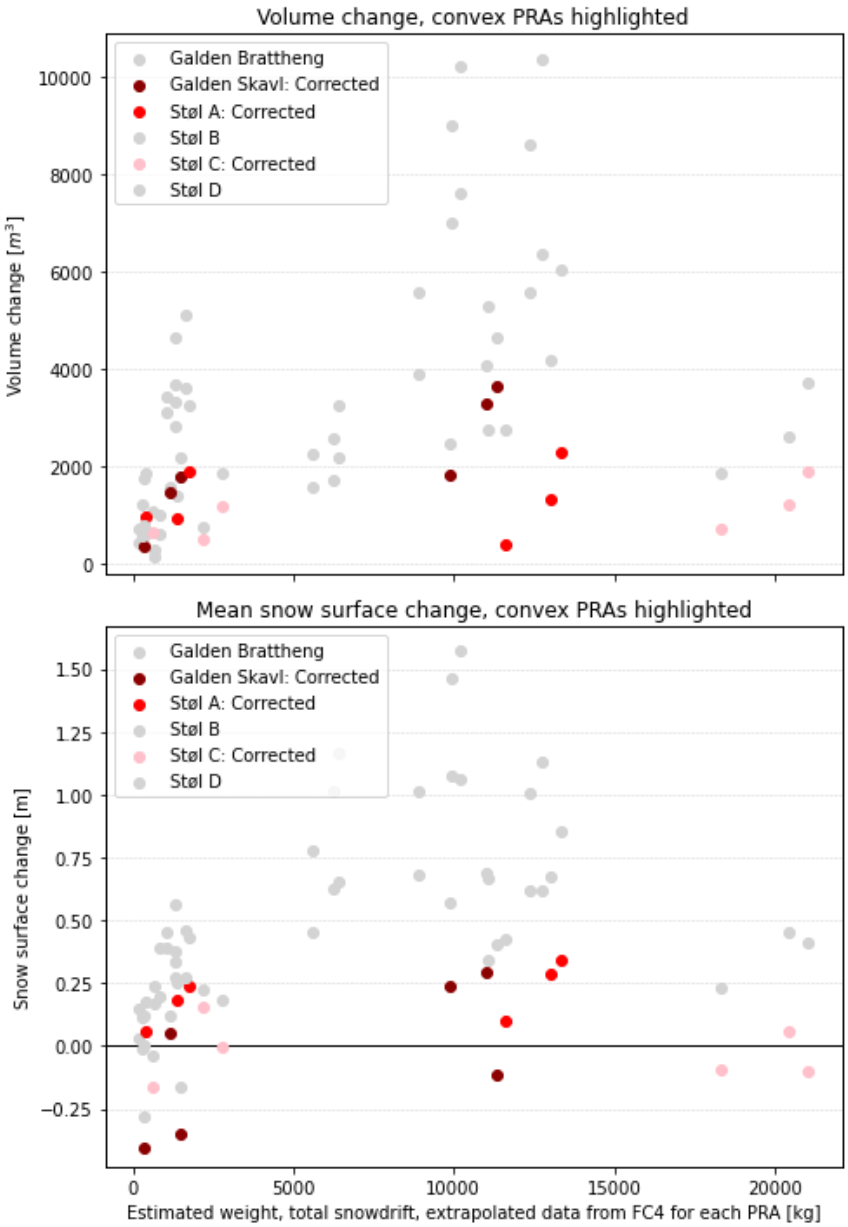

Figure 5.1.5: First subplot: Corrected volume changes for the *convex* PRAs highlighted as red nuances. Grey dots are the remaining datasets - including all corrections for additional precipitation. **Second subplot:** Corrected mean snow surface changes for the *convex* PRAs highlighted as red nuances. Grey dots are the remaining datasets - including all corrections for additional precipitation.

5.2 Relationship between Measured Snowdrift and Snowdrift Deposition

As the snowdrift depositions in the PRAs, seemingly, and expectedly, had large variations between them, a sensible way to go, regarding establishing a statistical relationship, were choosing an area that accumulated the most snow, but also in a steady manner. In this case it was PRA Støl B. Results Section 5.1 showed that volume changes had larger fluctuations than mean snow surface change - both within each PRA but also between them. Mean snow surface change is considered the best basis for such analysis as it excludes the effect from very small or large PRAs; small areas can have the same mean surface change as large areas.

The choice of Støl B as a reference is considered the most conservative approach in this case. This is the desirable attitude as well - since most of the issues regarding local avalanche warning are about dealing with uncertainty. An exponential fit for the dataset from Støl B is shown in Figure 5.2.1. The regression is fitted to the measurements and not the corrected values for additional precipitation.

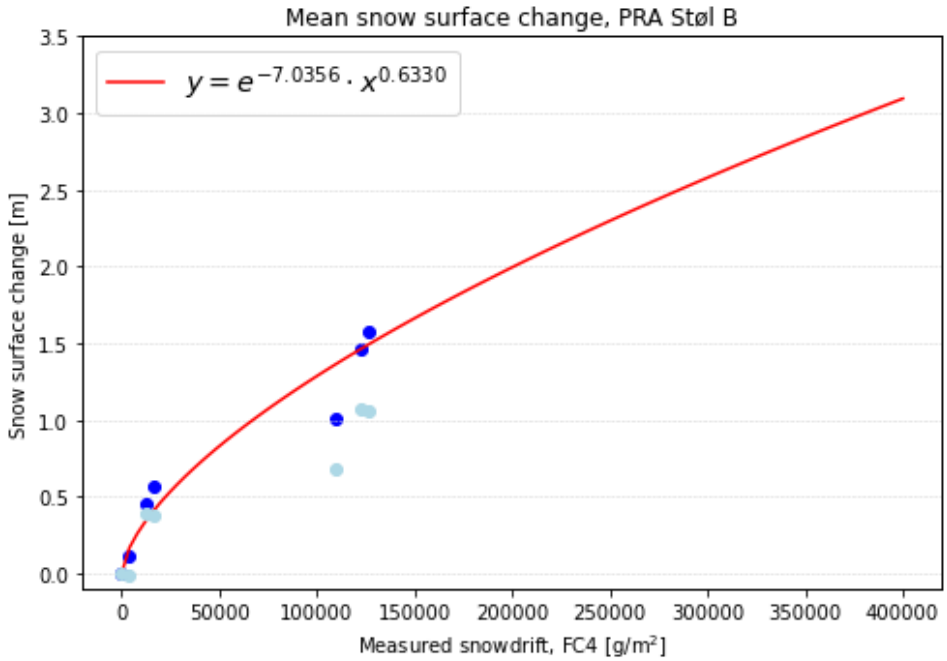

Figure 5.2.1: Exponential fit for the mean snow surface change at PRA Støl B. Light blue scatter points indicate corrected values for additional precipitation. Data collection stems from LiDAR-scan intervals: 15-17th, 15-19th, 15-21th, 17-19th, 17-21st, 19-21st.

For context, the exponential fit is visualized against the registered fracture heights from most of the avalanche controls in the winter seasons 2022-2023 and 2023-2024 (Fig. 5.2.2). This figure can indicate a good correlation to the maximum expected fracture height - but it is important to take into account that the recorded fracture heights are based on visual inspection in the field. However, this relationship can be beneficial as an additional tool in risk assessment, as it can contribute to reduce uncertainty.

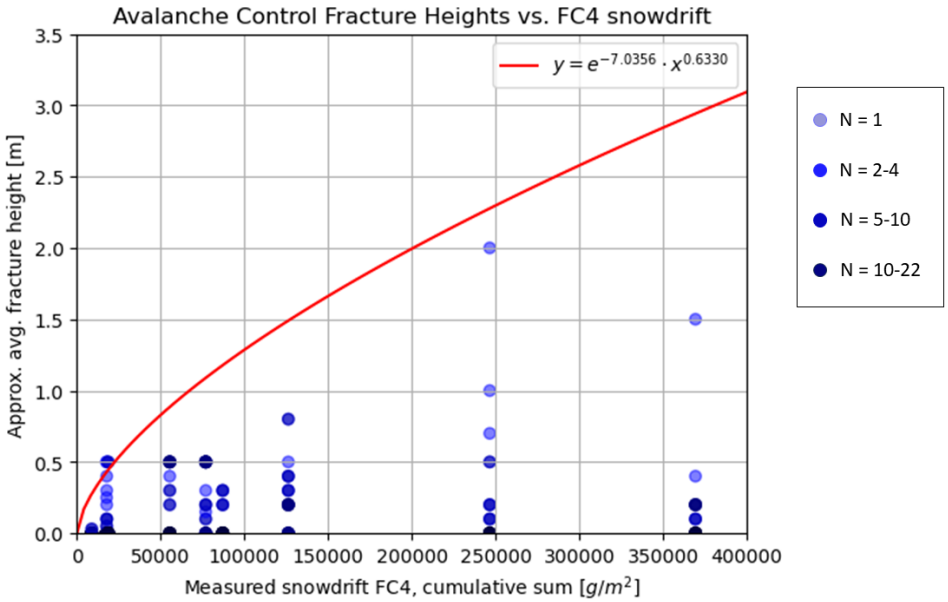

Figure 5.2.2: Registered fracture heights from the avalanche controls during winter seasons 2022-2023 and 2023-2024, N = number of registrations. Distributed over measured snowdrift (cumulative sum) from the FC4 with the zero-point set to the previous avalanche control. Fracture heights are approximations based on visual evaluation from road. Data summarized in Tab. D.1 in Appendix D. Total N = 216.

Additionally, Figure 5.2.2 shows us that most of the registrations are at lower FC4 values, but the fracture heights might not necessarily be the smallest ones. This can tell us that registrations during low FC4 values are based on snow-driven avalanche cycles, whereas for high FC4-values, avalanches are more based on wind-driven avalanche cycles. The largest fracture heights are experienced during high FC4 values. The largest fracture height registered were associated with an avalanche at Støl B 05.02.2024 [Skred AS - Varsom Regobs, 2024], and released within windslabs [Skred AS, 2024b].

5.3 In-depth Fieldwork Weather and Snowpack Development

In this section, a more detailed review of the snow cover development at the snowdrift catchment plateau is given, showing the methods used and the resulting data collected.

This section will introduce a short overview, and subsequently go chronologically through each defined period: The period before 13th, 13th (avalanche control) 14-15th, 16-17th, 18-19th, 20-21st, and 21st (avalanche control).

Overview: The overall goal of monitoring the snow cover in the fieldwork period 13-21 February was to continuously map snow available for wind transport and whether the old snow cover was prone to wind erosion or not. The snow drift sensor FC4 is installed at this plateau - above avalanche towers Støl 1 & 2 at Tyinstølen. The snow cover surveys focused on the upper part of the snow cover and mainly its snow type, hardness and density. It was seen as important to know whether most of the additional snowfall during fieldwork was transported or not, and whether the old snowpack contributed to the total amount of measured snowdrift from the FC4.

The development of the weather and the snowpack both prior to, and during the fieldwork 13-21 February were considered optimal in terms of carrying out a study of this nature. The snowpack at the plateau had stabilized by mild temperatures, and was minimally affected throughout the fieldwork period due to hard windcrust. Old skitracks from the 14th could be recognized the 19th - and were unaffected both in terms of additional snowfall and erosion. The period 19-21st had the most precipitation and winds, but the snow cover at the catchment plateau remained the same.

This provided a basis for assuming that most of the additional snowfall at the plateau during fieldwork was transported away from the plateau, and a portion of this were deposited in the larger lee-areas in the defined PRAs (Fig. 5.0.1), and a less proportion remained in the smaller lee areas on the catchment plateau (few cm). Sublimation is also assumed to have occurred, where the furthest transported snow particles have had a greater chance of sublimation before reaching the PRAs.

During the stay, the region experienced three storm events (summary of weather data earlier presented in Fig. 5.0.2); all with winds from the west. Snowfall occurred 5 of the 10 days in the field, with the most intense snowfall just before the avalanche control on the last field day, 21 February - where two avalanches went over the road and two avalanches almost reached the road. These avalanches, along with several others (EAWS avalanche size 1-2), had mostly fracture heights close to 50 cm [Skred AS - Varsom Regobs, 2023b].

- Before 13 February: Documents from Skred AS [2023a] stated that avalanche control and snow cover surveys on 8 February resulted in stable snow cover in the PRAs. 11-13 February experienced heavy snow transport and deposited large amounts of snow in the PRAs at both Tyinslinna and Tyin. Fieldwork by the author was not conducted before the 14th.

- 13 February: Avalanche control: Avalanche control 13 February produced two avalanches that released from the ground due to depth hoar (Mel 1, and Støl 1 which crossed the road), while at the other runout areas avalanches released from within the newest patch of windslabs (on layers including DF) - at between 10-20cm depth [Skred AS - Varsom Regobs, 2023a]. Figure 5.3.1 shows an overview of the runout lengths and fracture heights from this avalanche control. There was remaining snow in most of the PRAs except at Mel 1 and Støl 1 which had exposed bedrock (Fig. 5.3.2).

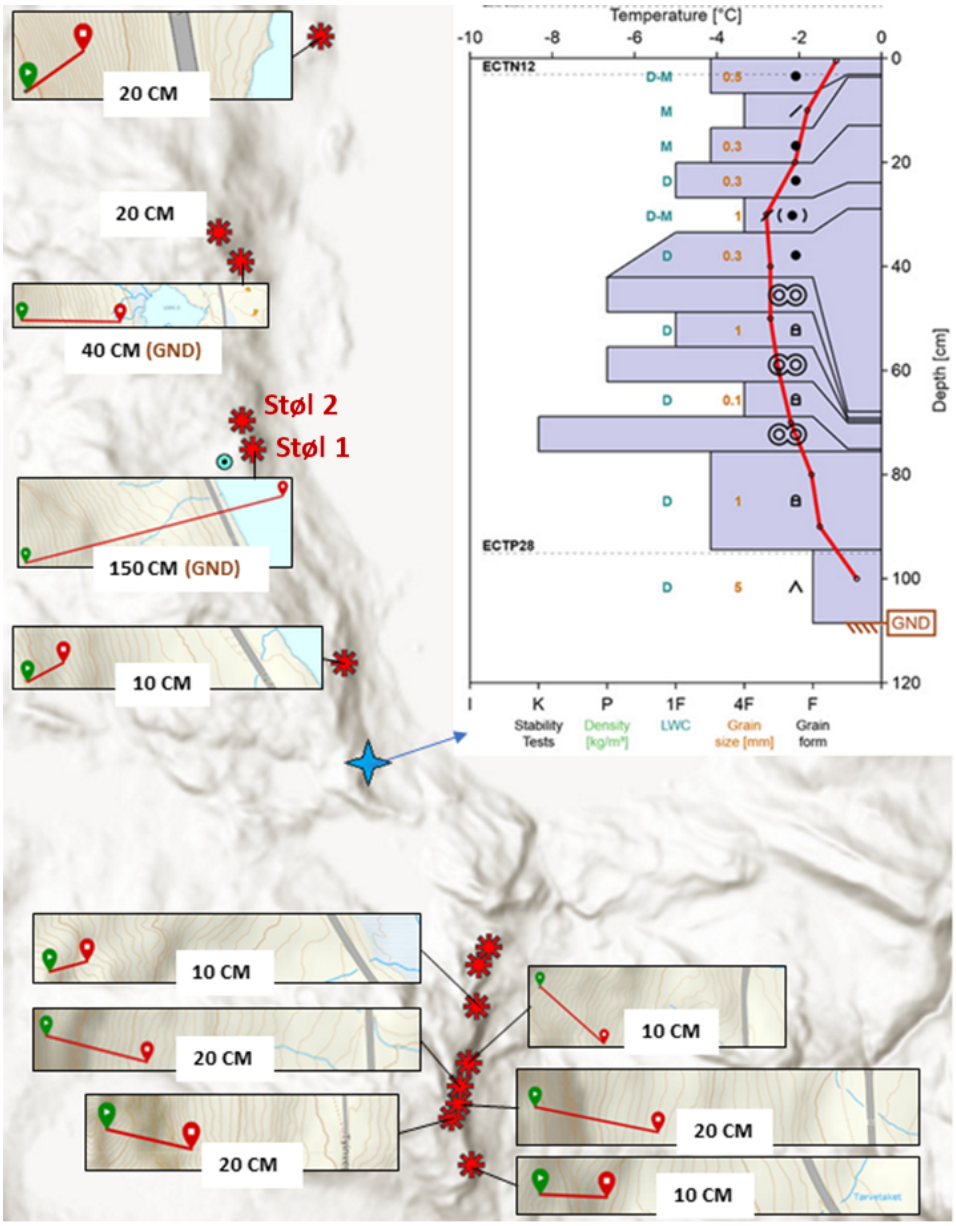

Figure 5.3.1: Overview of runout lengths and approximate fracture heights from the avalanche control conducted 13 February 2023 [Skred AS - Varsom Regobs, 2023a]. Includes a representative snow profile for the region, conducted the same day (`https://www.regobs.no/registration/329294`) by the author in cooperation with the forecasting group (Skred AS). Figure compiled by author - fracture heights, runout lengths, and snow profile are taken from Varsom Regobs [2024], available online.

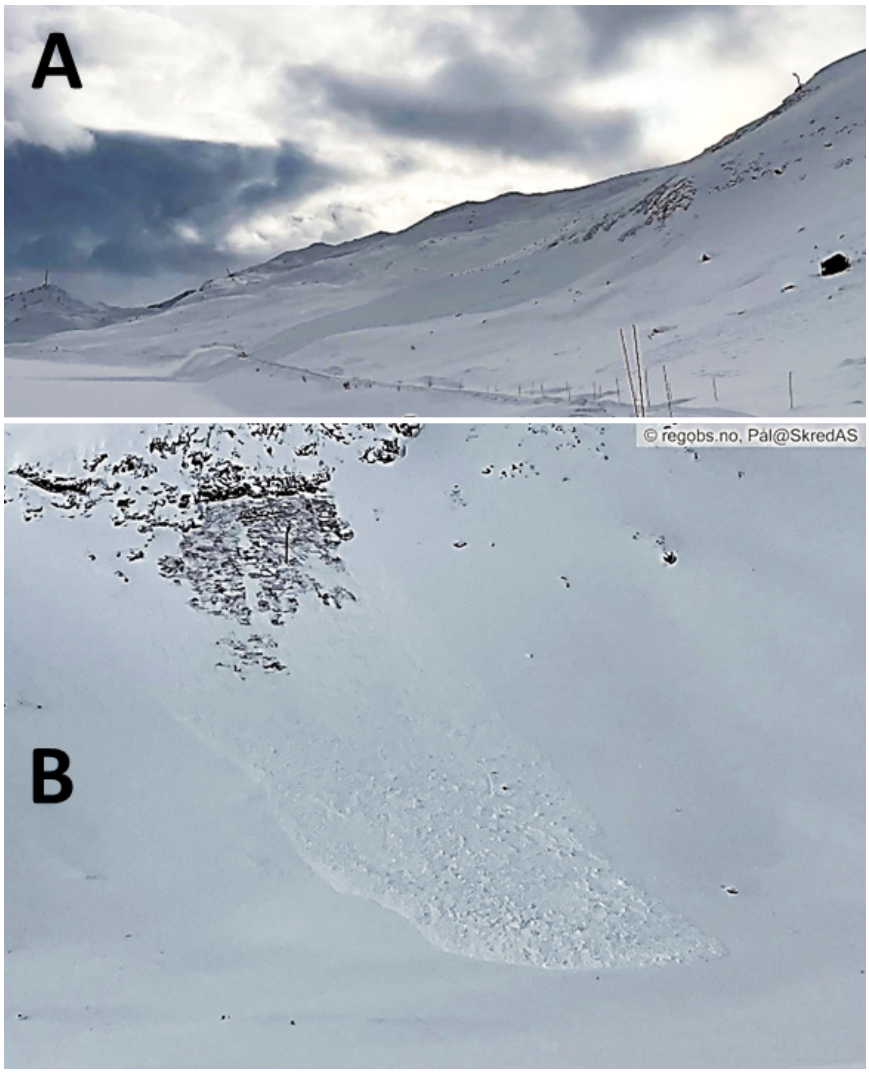

Figure 5.3.2: The two PRAs where avalanches released from the ground due to depth hoar. From the avalanche control 13 February 2023. **A)** The released area and deposited avalanche at Støl 1 (`https://www.regobs.no/registration/329250`) **B)** The released area and deposited avalanche at Mel 1 (`https://www.regobs.no/registration/329237`)

- 13-15 February - Stable conditions: Mild temperatures (over 0°C) had stabilized the remaining windslabs in the PRAs. Snow cover surveys at the plateau showed that the whole catchment region consisted of windcrust (or meltcrust depending on altitude), and had patches of overlying windpacked snow on approx. 15-20% of this area - based on visual estimations in-field (Fig. 5.3.3) and from photographs (Fig. 5.3.4). The windslabs were concentrated in lee areas towards the east.

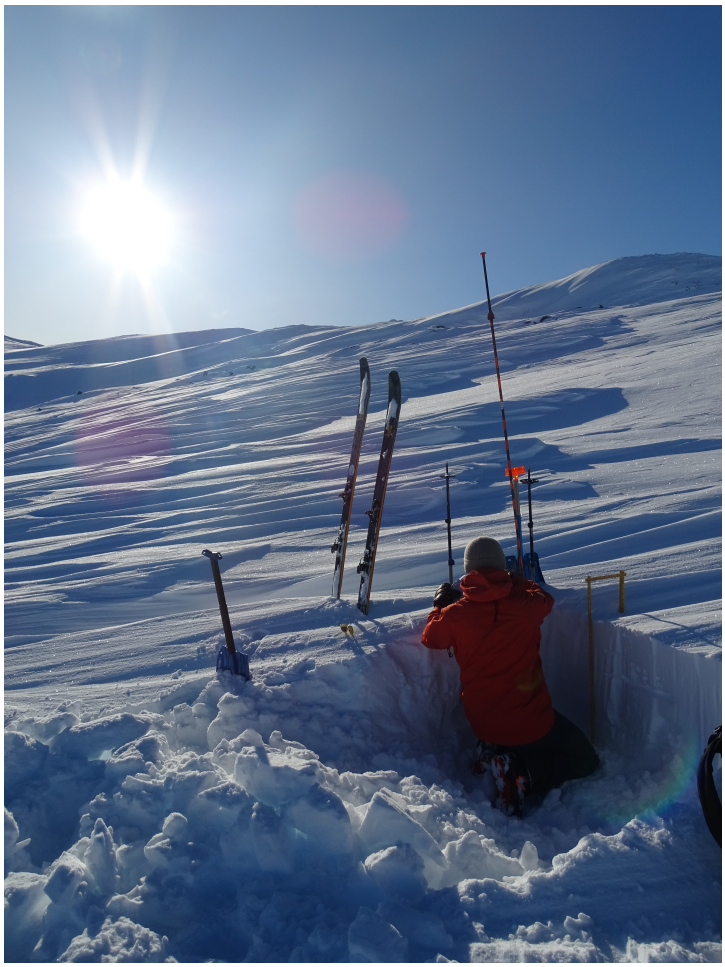

Figure 5.3.3: Patches of windslabs could be visually differentiated from the rest of the snow cover which consisted of a pen-strong windcrust. Here, the author conducts a snow cover survey on a representative windslab. Direction of photography towards SSW, taken by field assistant nr. 1 of 2: Fabrice Kaltenrieder.

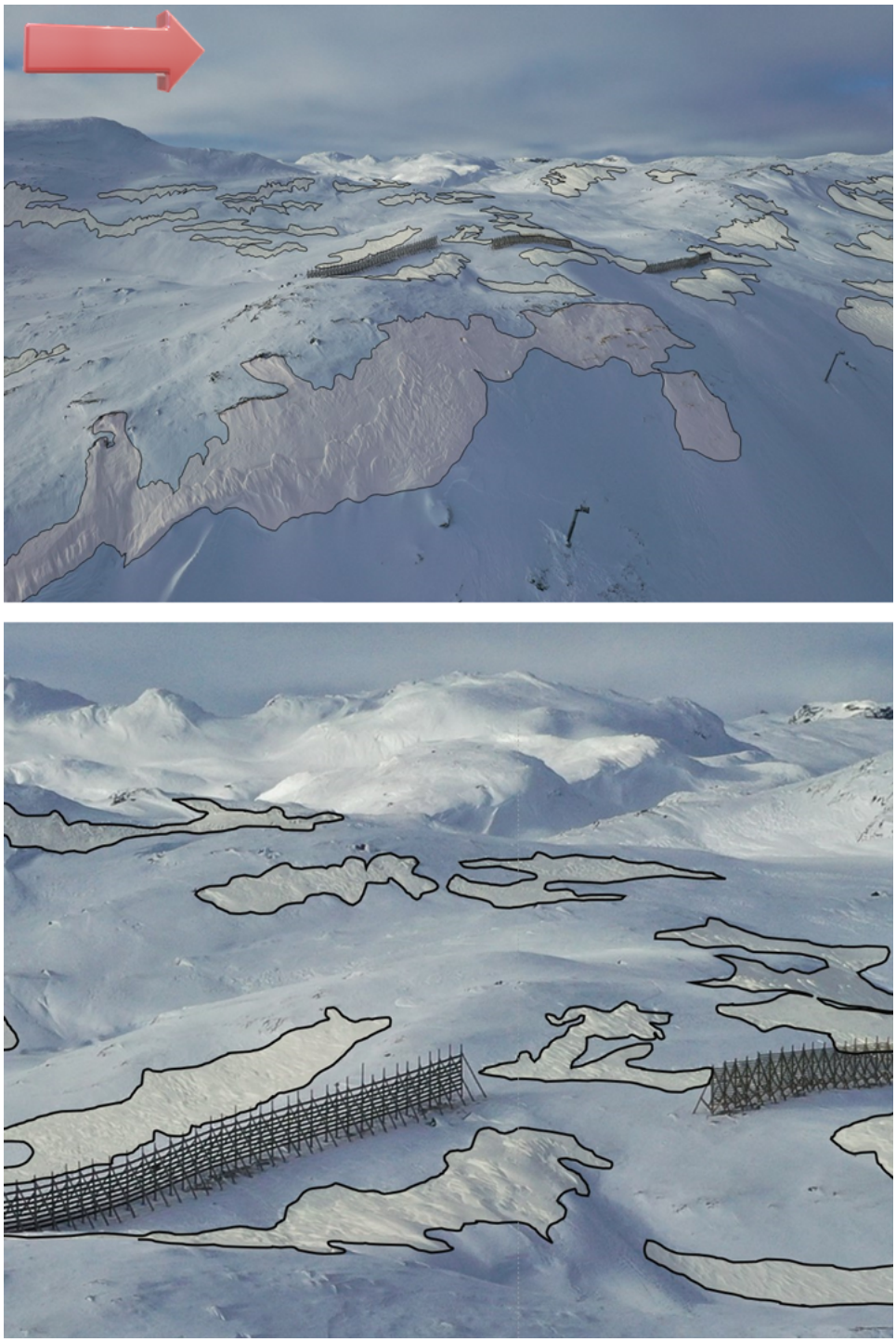

Figure 5.3.4: Overview of the fieldwork area at the plateau just above Tyinstølen. Wind slabs marked by polygons sketched by the author, based on visual observations in-situ and on photographs. The underlying snow cover base consisted of hard windcrust. Direction of north indicated by red arrow. Picture taken by the author 21.02.2023.

The wind slabs had a thin layer of wind crust (pen-hardness) on top, and an average density of around 240 kg/m^3 (Fig. 5.3.5). Here it is important to be aware that these values might be an underestimation between 0-9% [Proksch et al., 2016; Hao et al., 2021; Conger & McClung, 2009] due to the precision of the wedge shaped density cutter and the small volume/low resolution.

Figures 5.3.7 & 5.3.6 show details on the underlying wind crusted base from snow cover surveys.

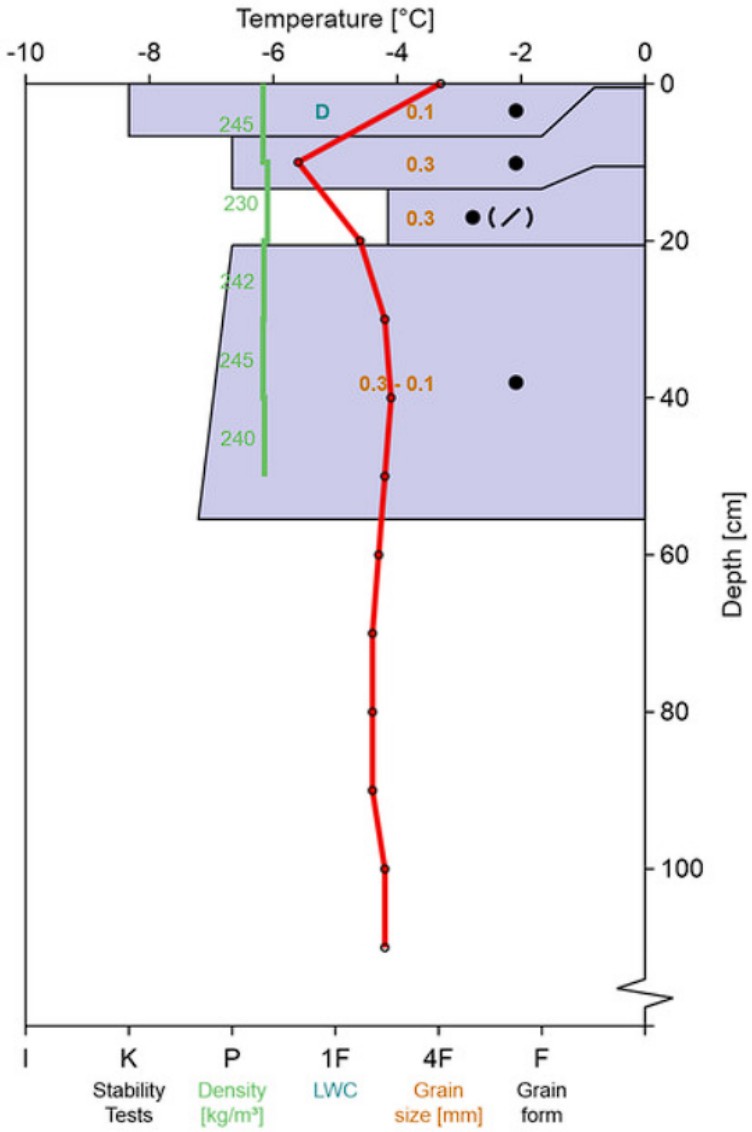

Figure 5.3.5: Survey on a wind slab on an eastern aspect at the plateau, 14 February. Ignores the underlying crust snowpack. Uncovers a weak layer of Decomposing and Fragmented precipitation particles (DF), which will later be recognized, and help to determine the relative age of subsequent snowdrift deposition. `https://www.regobs.no/Registration/329530`

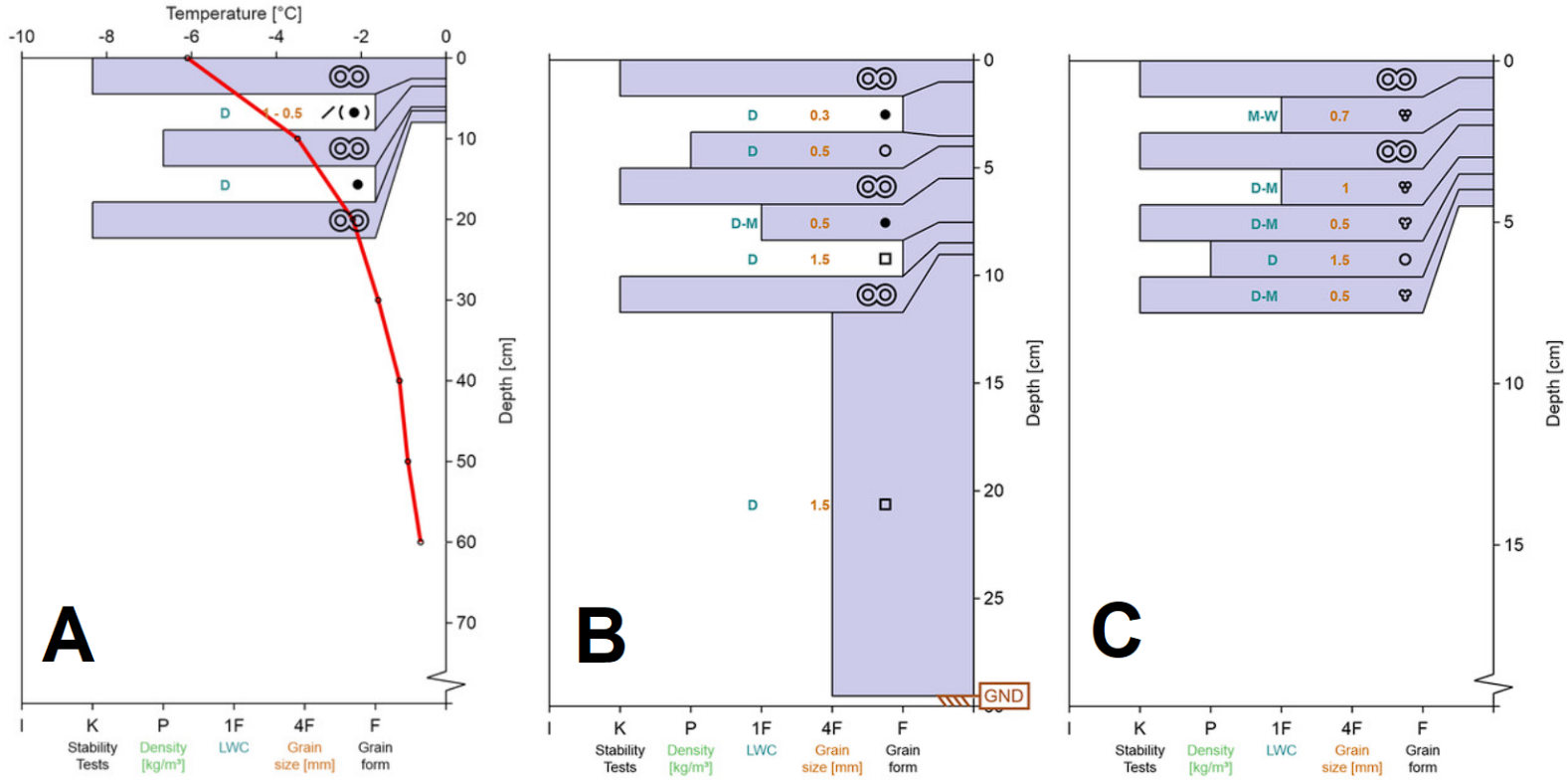

Figure 5.3.7: Surveys on the wind crusted base at the plateau, 14 February. Focuses on the properties of the uppermost part of the crust. Ignores the overlying windslabs. **A)** Crust thickness at the top is 2,5cm. Conducted in a north-faced aspect at 1299 m.a.s.l., **B)** Crust thickness at the top is 1cm. Conducted in a flat terrain at 1281 m.a.s.l., **C)** Crust thickness at the top is 0,5cm. Conducted in a SE-facing aspect at 1252 m.a.sl.
A: `https://www.regobs.no/Registration/329536`
B: `https://www.regobs.no/Registration/329539`
C: `https://www.regobs.no/Registration/329542`

Figure 5.3.6: Upper part of the crusted base, which covers most of the plateau. The layers of crust and melt forms can be seen here. This is a cross-section related to snow pit survey part C in Fig. 5.3.7.

- 16-17 February - Snowfall & moderate breeze from SE: Figure 5.3.8 shows that this period gave 12.7 mm of precipitation, mainly with gentle-moderate breeze (4-7 m/s) from the SE - but data holes and snowdrift measurements might indicate the winds perhaps were stronger during snowfall. Snowdrift was measured both during and after snowfall, with the strongest snowdrift after the most intense precipitation.

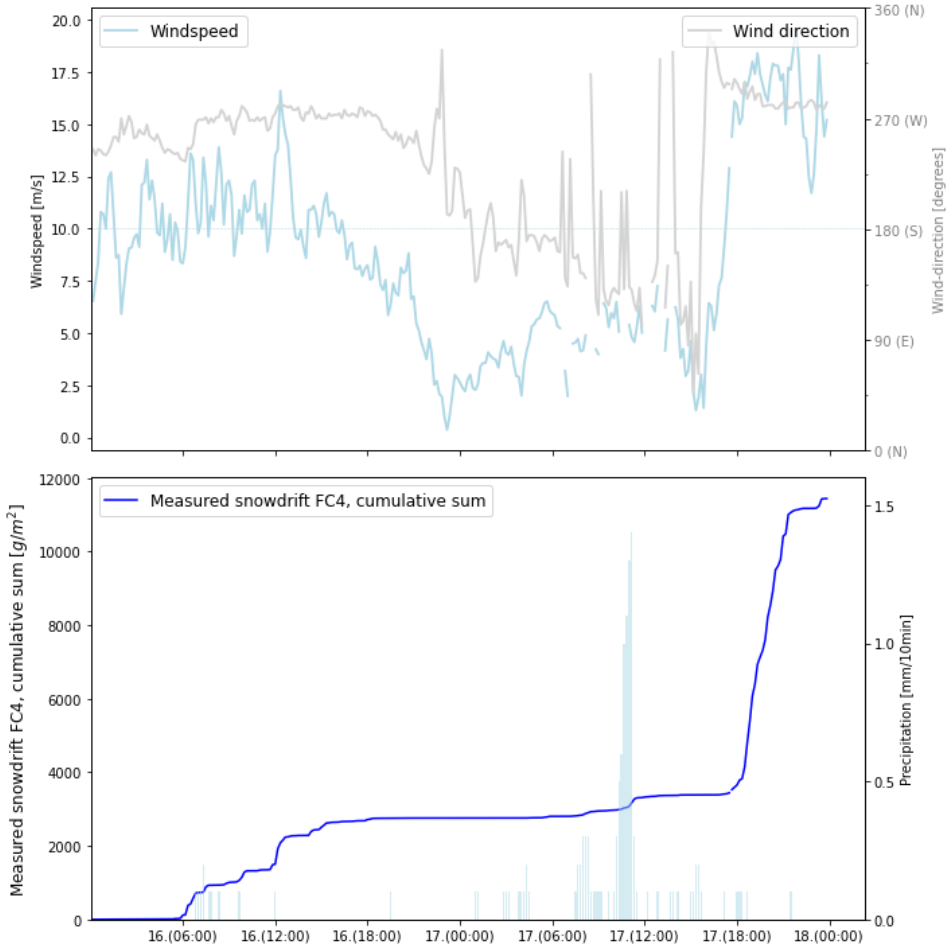

Figure 5.3.8: First subplot: Windspeed and direction. **Second subplot:** Measured snowdrift from FC4 (cumulative sum), and precipitation (FV53 Tyinosen Weather Station). Shows the weather development during 16-17 February. Most precipitation came with winds from the SE. A horizontal line at wind speed value 10 m/s is displayed to mark the experienced wind speed threshold value for registered snowdrift, as experienced throughout the winter season 22/23 [Skred AS, 2023b].

- 18-19 February - Strong breeze from W: Winds from the west transported the fresh snow and deposited a small layer (few cms) of fresh wind slab (Fig. 5.3.9) on the same wind slab patches as mentioned from earlier. A buried weak layer of DF (Fig. 5.3.10) could be recognized from 14 February, and helped determine the relative age of the newest patches of windslabs.

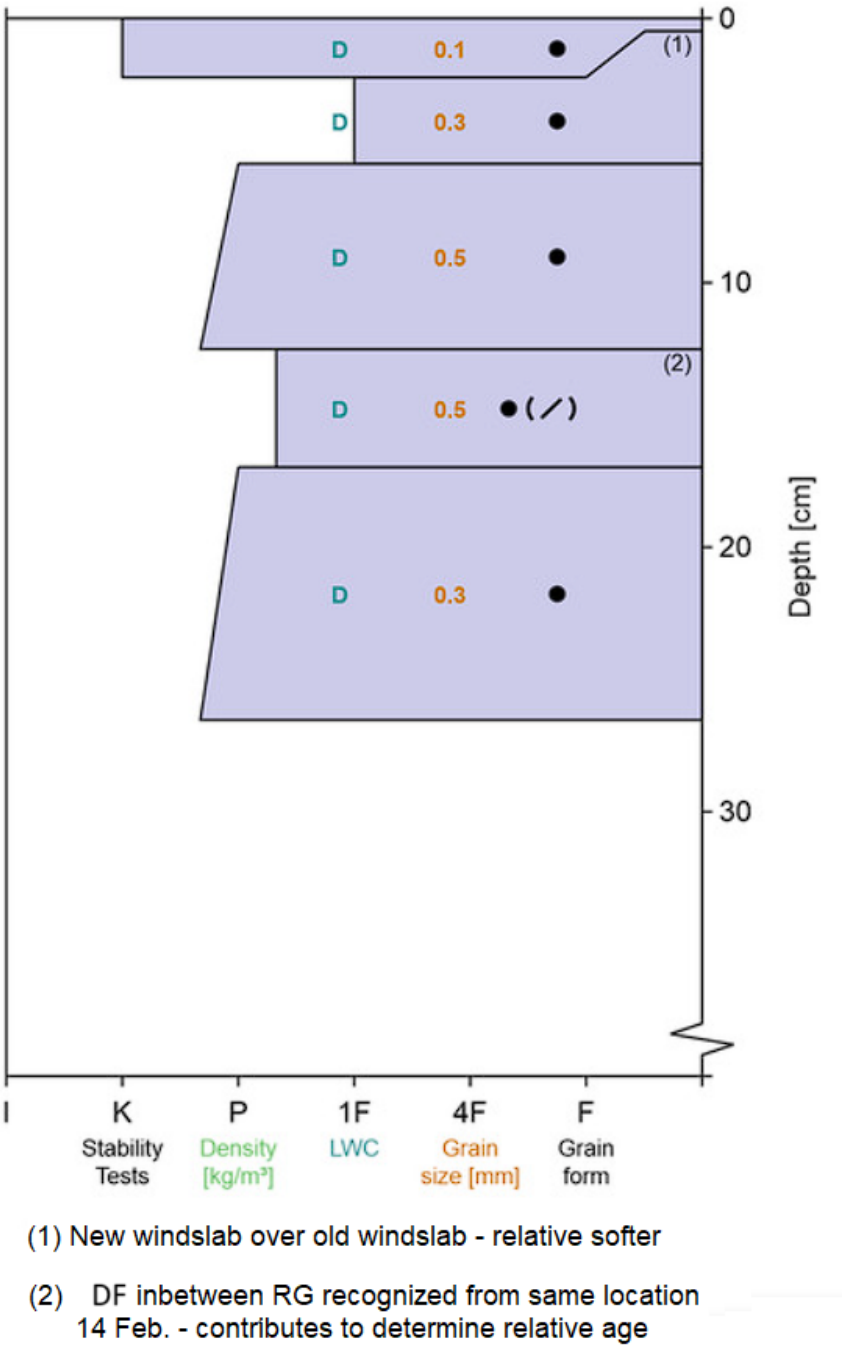

Figure 5.3.9: Snow cover survey done close to the older snow profile from 14 February (Fig. 5.3.5). Shows the development of the wind slab patches after snowfall and wind transport 14-19 February. The recognized DF inbetween RG (2) contributes to determine the relative age and differentiating the old windslabs against the newest windslabs (1).

Figure 5.3.10: DF recognized from 14 February. Sunlight shines through this layer to a greater extent than the other layers. Snow profile summarized in Fig. 5.3.9. Picture taken 19 February.

The snow cover were close to identical to the situation from Tuesday 14 February. The hard wind slabs still covered approx. 15-20% of the plateau, in the same lee-areas.

The crusted layer had not been torn up by the wind, which could be determined by the examination of old ski tracks and relative dating of older torn crust (Fig. 5.3.11).

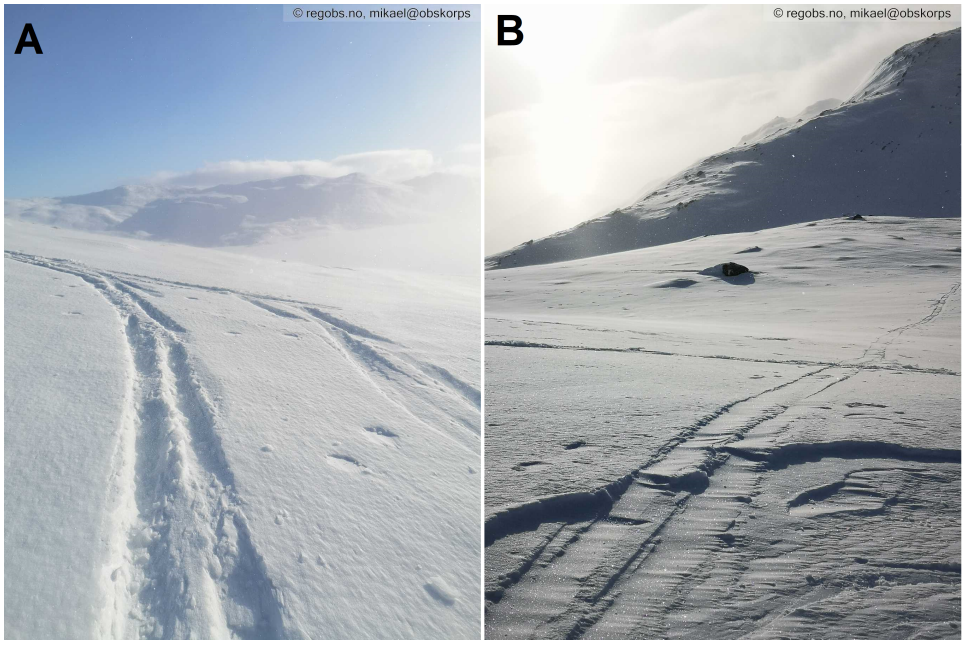

Figure 5.3.11: A) The crust at the plateau has not been torn up by the wind anywhere along our old ski tracks from 14 February
B) Patches of torn crust could be dated before 14 February - by associating it with our old ski tracks from 14 February. Pictures taken 19 February.

- 20-21 February - Strong snowfall & moderate gale from W: During 20-21 February, a total of 32.6 mm precipitation fell, followed by moderate gale from the west, contributing to further snowdrift, as seen in Figure 5.3.12.

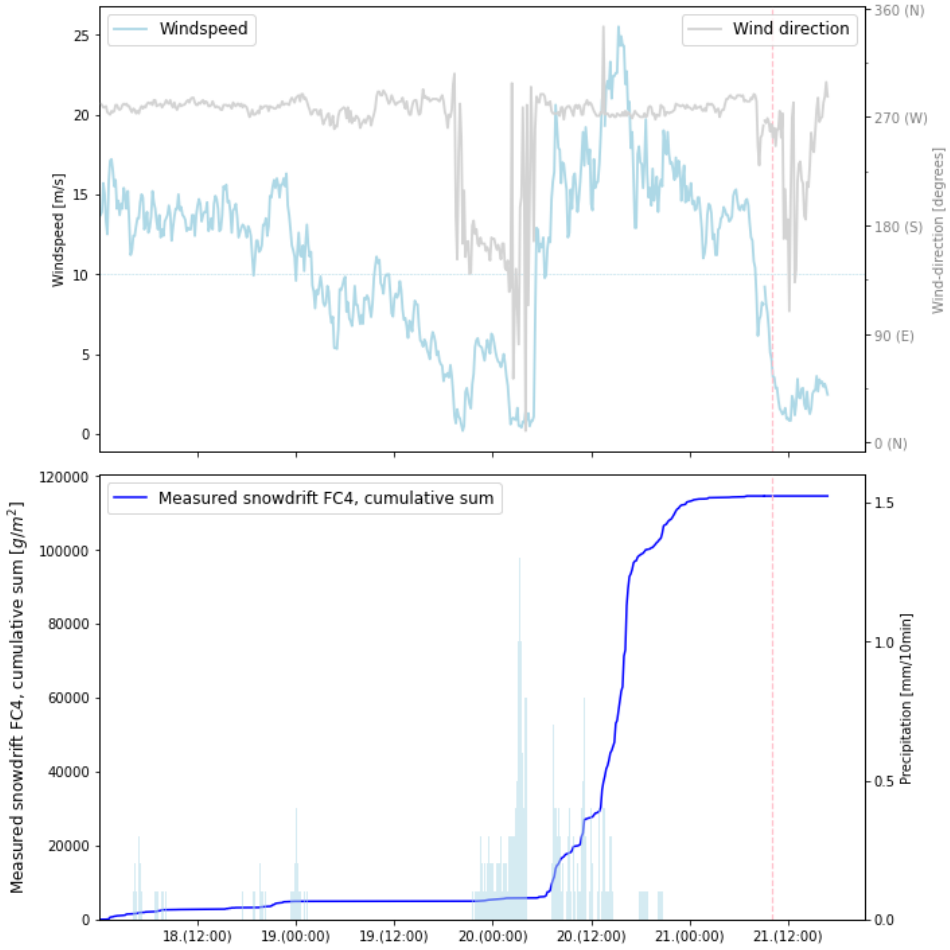

Figure 5.3.12: First subplot: Windspeed and direction. **Second subplot:** Measured snowdrift from FC4 (cumulative sum), and precipitation (FV53 Tyinosen Weather Station). Shows the weather development during 20-21 February. Red vertical line shows the time of avalanche control. Most precipitation came with winds from the S-SE.

- 21 February - Avalanche control: Avalanche control gave good results with avalanche releases on layer nuances within the newest windslabs in the PRAs. Avalanches crossed the road at Langø (Fig. 5.3.13) and Gamle Varden. Tørv 1 and 2 almost reached the road. Other avalanche runouts gave size 1–2 avalanches, with fracture heights mostly close to 50 cm [Skred AS - Varsom Regobs, 2023b]. An overview of the runout lengths are shown in Figure 5.3.14.

Figure 5.3.13: The avalanche that crossed the road underneath Langø avalanche tower during the avalanche control 21 February 2023. Picture taken the same day, by Falkeblikk AS as commissioned by NVE.

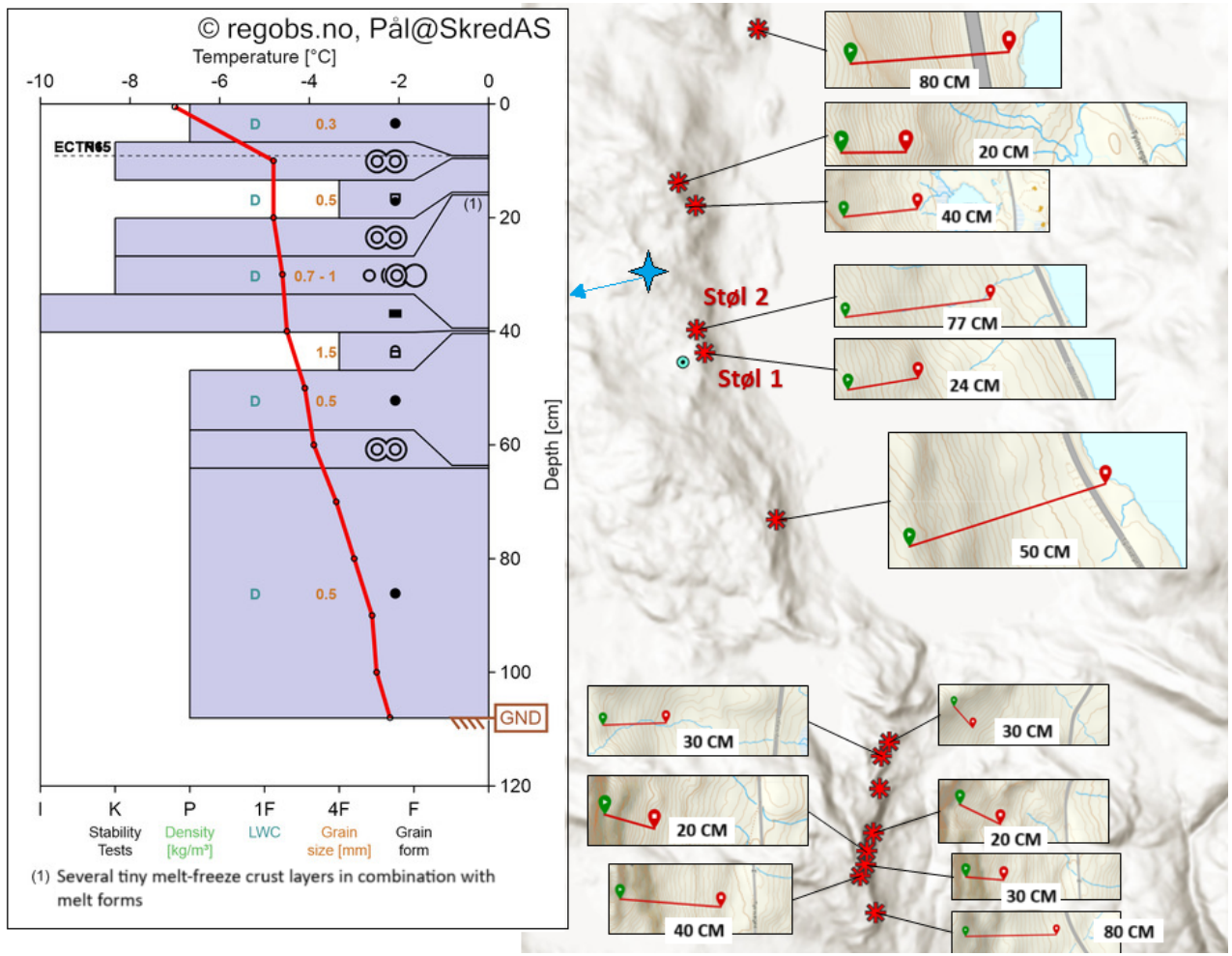

Figure 5.3.14: Overview of runout lengths and approximate fracture heights (except at Støl A & B which are precise avg. fracture heights measured from LiDAR) from the avalanche control conducted 21 February 2023 [Skred AS - Varsom Regobs, 2023b]. Includes a representative snow profile for the region, conducted the same day (`https://www.regobs.no/registration/330930`) by the author in cooperation with the forecasting group (Skred AS).

The depths of the released snow at Støl A & B during avalanche control 21 February were derived from laserscan, and are presented in Figures C.1 & C.2 in Appendix C. The analysis conclude with following numbers:

- Released area Støl A: Mean elevation change: −0.237 m (SD = 0.166)
- Released area Støl B: Mean elevation change: −0.772 m (SD = 0.276)

6

Discussion

Using the measured data from the FlowCapt 4 (FC4) sensor to establish a relationship to deposited snow depth appears to be feasible. However, the results show that the choice of method for measuring snow surface change will have significant influence on the outcome - and so do the spatial outlining of the chosen Potential Release Area (PRA). Mean snow surface change is a better basis than volume change for such relationship as it equalizes the impact from spatial variation within different PRAs, as well as their different length-width ratios.

As expected, it turns out that wind-exposed convex areas accumulate less snow than concave areas in more wind-protected areas. Therefore, it makes sense to focus on an area like Støl B, which, as shown in the results, accumulates relative more snow in a consistent manner, facilitating measurements of the highest snow depths in the total distribution.

Regarding the future use of the newly installed snow depth sensor (Fig. 6.0.1) at Tyinstølen, it meets the same criteria regarding the choice of the most applicable area in deriving the highest snow depths, as it is placed in a very wind-protected lee-area facing east. This is however a point-measurement, but one that might be comparable to the mean snow surface changes in the PRAs. It is expected to be useful in further data collection to build upon the proposed empirical relationship between measured snowdrift and deposited snow depth. Notably, it is also mounted on flat ground under the mountainside, not on the slope, perhaps allowing the measurements to be even more on the conservative side – which in that case has both upsides and downsides, and has to be taken into account.

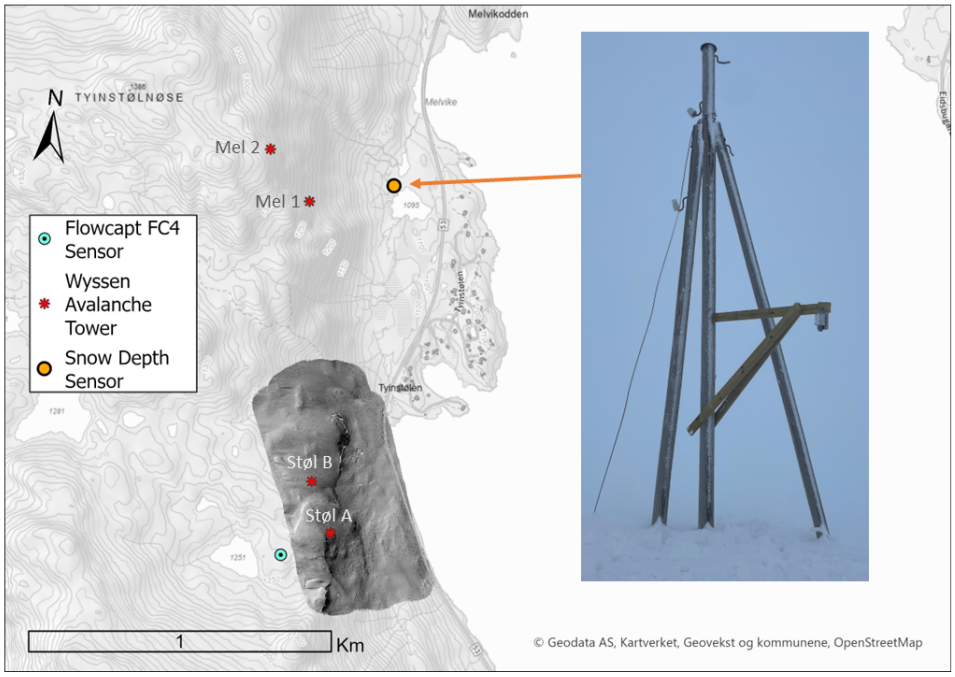

Figure 6.0.1: Location of the snow depth sensor (DecentLab MBX-01 sensor) installed March 2024 by Skred AS. Picture of the sensor taken by Skred AS.

Comparing the various PRAs with each other by extrapolating FC4 data introduces several significant uncertainties. The method of selecting a cross-section tailored to each PRA is based on assumptions and is debatable as to whether it is a good method or not – as mentioned, each PRA also varies in length-width ratio, leading to large variations in measured volume despite relatively similar length of chosen cross-sections. A closer analysis of the correlation between measured snowdrift and volume changes could be done by calculating the mass related to the volume change, but was not conducted. This could be a potential direction for further exploration – this again involves a generalization of the assumed density of the deposited snow, which may vary both spatially and temporally.

The proposed exponential relationship between measured snowdrift and snowdrift deposition was based on mean snow surface change (from LiDAR measurements) and does not account for corrections for additional precipitation. In general, there are uncertainties about the role of precipitation during snowdrift events regarding deposition in PRAs. The study by Radlwimmer [2023] showed that the major snow depth changes in Longyearbyen in Svalbard were mostly linked to high wind speeds - but neither precipitation nor wind was found to be a good proxy for snow depth changes, despite both having a great influence on it.

The data for the concave areas Støl B, Støl D, and Galden Brattheng (Appendix B, Figs. B.2, B.4, and B.5) indicate that it would be possible to apply a regressional trend on the corrected values aswell. But in general, these corrections seem to weaken the correlations as they make the dataset fluctuate more, and thus do not increase or contribute to a stronger relationship. Since the snow cover at the snowdrift catchment plateau was almost constant, and most of the snowfall was transported, one would have expected that corrections regarding additional precipitation would contribute to a stronger correlation - which was not the case. Perhaps this is an indication that snowfall during snowdrift does not necessarily have a significant role in determining snow surface changes - given there is a steady correlation between measured snowdrift and snowdrift deposition. However, for practical field application and to reduce uncertainty, regression was not carried out for the corrections as the most conservative approach lied with the focus on the actual measurements.

The measurements from FC4 must also be considered to have some uncertainty. The study by Cierco et al. [2007] showed that sensor saturation must be considered when extreme wind occurs. That study, along with several others [Font et al., 1998; Michaux et al., 2000; Jaedicke, 2001; T. Sato et al., 2005; Das et al., 2012; Trouvilliez et al., 2015; Zhang et al., 2022; Baron et al., 2023] highlights its limitations concerning quantitative data for research purposes, but that it plays an important role for operational application in determining the time intervals of snowdrift occurrences and to obtain a qualitative estimation of snow fluxes [Chritin et al., 1999; Jaedicke, 2001; Lehning et al., 2002; Lehning & Fierz, 2008; Vionnet et al., 2018; Skred AS, 2023b].

The snowdrift sensor is thus considered a tool that can continue to be used in the same way as before at this location, and that an empirical relationship to deposited snow depth can be built upon by the newly installed snow depth sensor at Tyinstølen.

Even if collecting more measurements with LiDAR-scans can be time- and resource-consuming, the results of this study may indicate that not necessarily too many additional LiDAR-datasets are needed before a strong correlation between measured snowdrift and mean surface change at Støl B is established.

Comparison of the proposed relationship against fracture heights for the winter seasons 22/23 and 23/24 can show a very rough correlation, and give indications on the maximum expected fracture height. However, it must be emphasized that these registrations are based on assumed fracture heights – determined from visual sight from the road.

This underlines the need for more precise measurements on fracture heights from avalanches if this data is to be used as a verification method for the proposed empirical relationship. In that case, photogrammetry (Structure-from-Motion (SfM)) can be an applicable method [McCormack et al., 2024],

and can detect snow depth changes of minimum 10-20 cm with high degree of certainty [Solbakken, 2019]. Collecting SfM-data from images by commercial off-the-shelf digital cameras is considered cheaper and more available than LiDAR-mounted drones.

Nevertheless, by continuing gathering data on registered fracture heights, this can help strengthen the data basis for verification of a empirical relationship between measured snowdrift and mean snow surface change - which can be used to say something about the maximum expected fracture height.

/7

Conclusion

The installed snowdrift sensor FlowCapt 4 (FC4) at County Road 53 Tyin-Årdal has contributed well to the risk assessment in the local avalanche warning by Skred AS through its first two winter seasons. While it mainly functions as a tool for assessing the snowdrift occurrence intervals, this study explored additional methods in an attempt to quantify snow drift and look for a correlation between measured snow drift and deposited snow.

An exponential relationship between measured snowdrift from the FC4 and mean surface change (measured from LiDAR-scans) for Potential Release Area (PRA) Støl B was presented. This relationship was compared to the registered fracture heights from avalanche controls during winter seasons 22/23 and 23/24, and shows a good correlation but underlines the need of more precise measurements on fracture heights from released avalanches, especially if this data will be further used as verification for the proposed relationship in the future.

In terms of additional snowfall during snowdrift events, this study applied corrections for that, and showed that corrections weakened the correlation as the dataset fluctuated more, and did not contribute to a stronger correlational trend. The snow cover at the snowdrift catchment plateau were almost constant throughout fieldwork, and most of the snowfall was therefore transported. Given the assumption of a steady correlation between snowdrift and snowdrift depostion, one would expect corrections to indicate a stronger relationship,

which was not the case. This might conclude with that snowfall during snowdrift might not have a significant role in determining or affecting snow surface changes as the wind plays the main part.

Measurements of volume changes were experienced to have more fluctuations than mean snow surface change against measured snowdrift. This study tried to compare deposition changes in each PRA by extrapolating the FC4-data, both for volume and surface change, and were found to indicate a comparability between areas with the same convexity (concave/convex). There are however a lot of uncertainty regarding the precision of the method as it is in an exploratory stage.

This study shows that, for building a relationship between measured snow depth and snow deposition, it might suffice to keep it simple with point-observations both in the snowdrift and deposition measurements - but with careful choice of locations that represents the largest values of the snow depth distribution for the more conservative approach. The newly installed snow depth sensor at Tyinstølen is considered a well-placed sensor that can further build upon the strengthening of an empirical relationship.

Bibliography

Aggarwal, S. (2004). Principles of remote sensing. *Satellite remote sensing and GIS applications in agricultural meteorology*, *23*(2), 23–28.

Ancey, C. (2001). Snow avalanches. In *Geomorphological fluid mechanics* (pp. 319–338). Springer. https://doi.org/10.1007/3-540-45670-8_13.

Awasthi, S., & Varade, D. (2021). Recent advances in the remote sensing of alpine snow: A review. *GIScience & Remote Sensing*, *58*(6), 852–888. https://doi.org/10.1080/15481603.2021.1946938.

Bakkehøi, S. (1983). Vær-, snø-og skredobservasjoner i Grasdalen. en sammenfatning (Weather, snow and avalanche observations in Grasdalen - a summary).

Baron, M., Haddjeri, A., Lafaysse, M., Le Toumelin, L., Vionnet, V., & Fructus, M. (2023). Snowpappus v1.0, a blowing-snow model for large-scale applications of crocus snow scheme. *Geoscientific Model Development Discussions*, *2023*, 1–52. https://doi.org/10.5194/gmd-17-1297-2024.

Bartelt, P., Buser, O., Valero, C. V., & Bühler, Y. (2016). Configurational energy and the formation of mixed flowing/powder snow and ice avalanches. *Annals of Glaciology*, *57*(71), 179–188. https://doi.org/10.3189/2016AoG71A464.

Bergen, J. D. (1978). Some measurements of settlement in a rocky mountains snow cover. *Journal of Glaciology*, *20*(82), 141–148. https://doi.org/10.3189/S0022143000198041.

Bigg, P. (1967). Density of water in SI units over the range 0-40 C. *British Journal of Applied Physics*, *18*(4), 521. https://doi.org/10.1088/0508-3443/18/4/315.

Birkeland, K. W., Mock, C., & Shinker, J. (2001). Avalanche extremes and atmospheric circulation patterns. *Annals of Glaciology*, *32*, 135–140. https://

doi.org/10.3189/172756401781819030.

Boyd, J., Haegeli, P., Abu-Laban, R. B., Shuster, M., & Butt, J. C. (2009). Patterns of death among avalanche fatalities: a 21-year review. *CMAJ*, *180*(5), 507–512. https://doi.org/10.1503/cmaj.081327.

Budei, B. C., St-Onge, B., Hopkinson, C., & Audet, F.-A. (2018). Identifying the genus or species of individual trees using a three-wavelength airborne lidar system. *Remote Sensing of Environment*, *204*, 632–647. https://doi.org/10.1016/j.rse.2017.09.037.

Chang, A. T., Foster, J. L., & Hall, D. K. (1987). Nimbus-7 SMMR derived global snow cover parameters. *Annals of glaciology*, *9*, 39–44. https://doi.org/10.3189/S0260305500200736.

Chang, A. T., Foster, J. L., Hall, D. K., Rango, A., & Hartline, B. K. (1982). Snow water equivalent estimation by microwave radiometry. *Cold Regions Science and Technology*, *5*(3), 259–267. https://doi.org/10.1016/0165-232X(82)90019-2.

Christen, M., Kowalski, J., & Bartelt, P. (2010). RAMMS: Numerical simulation of dense snow avalanches in three-dimensional terrain. *Cold Regions Science and Technology*, *63*(1-2), 1–14. https://doi.org/10.1016/j.coldregions.2010.04.005.

Chritin, V., Bolognesi, R., & Gubler, H. (1999). FlowCapt: a new acoustic sensor to measure snowdrift and wind velocity for avalanche forecasting. *Cold Regions Science and Technology*, *30*(1-3), 125–133. https://doi.org/10.1016/S0165-232X(99)00012-9.

Cierco, F.-X., Naaim-Bouvet, F., & Bellot, H. (2007). Acoustic sensors for snowdrift measurements: How should they be used for research purposes? *Cold Regions Science and Technology*, *49*(1), 74–87. https://doi.org/10.1016/j.coldregions.2007.01.002.

Clark, M. P., Hendrikx, J., Slater, A. G., Kavetski, D., Anderson, B., Cullen, N. J., ... Woods, R. A. (2011). Representing spatial variability of snow water equivalent in hydrologic and land-surface models: A review. *Water Resources Research*, *47*(7). https://doi.org/10.1029/2011WR010745.

Colbeck, S. (1980). Thermodynamics of snow metamorphism due to variations in curvature. *Journal of Glaciology*, *26*(94), 291–301. https://doi.org/10.3189/S0022143000010832.

Colbeck, S. (1982). An overview of seasonal snow metamorphism. *Reviews of Geophysics*, *20*(1), 45–61. https://doi.org/10.1029/RG020i001p00045.

Colbeck, S. (1983). Theory of metamorphism of dry snow. *Journal of Geophysical Research: Oceans*, *88*(C9), 5475–5482. https://doi.org/10.1029/JC088iC09p05475.

Colbeck, S. (1993). The vapor diffusion coefficient for snow. *Water resources research*, *29*(1), 109–115. https://doi.org/10.1029/92WR02301.

Colbeck, S. (1997). A review of sintering in seasonal snow. https://hdl.handle.net/11681/9229.

Colbeck, S. (1998). Sintering in a dry snow cover. *Journal of Applied Physics*, *84*(8), 4585–4589. ttps://doi.org/10.1063/1.368684.

Collis, R. (1970). Lidar. *Applied optics*, *9*(8), 1782–1788. https://doi.org/10.1364/AO.9.001782.

Colomina, I., & Molina, P. (2014). Unmanned aerial systems for photogrammetry and remote sensing: A review. *ISPRS Journal of photogrammetry and remote sensing*, *92*, 79–97. https://doi.org/10.1016/j.isprsjprs.2014.02.013.

Conger, S. M., & McClung, D. M. (2009). Comparison of density cutters for snow profile observations. *Journal of Glaciology*, *55*(189), 163–169. https://doi.org/10.3189/002214309788609038.

Conway, H., & Raymond, C. (1993). Snow stability during rain. *Journal of Glaciology*, *39*(133), 635–642. https://doi.org/10.3189/S0022143000016531.

Cracknell, A. P. (2007). *Introduction to remote sensing*. CRC press.

Das, R., Datt, P., & Acharya, A. (2012). An assessment of the FlowCapt acoustic sensor for measuring snowdrift in the Indian Himalayas. *Journal of earth system science*, *121*(6), 1483–1491. https://doi.org/10.1007/s12040-012-0234-2.

Deems, J. S., Gadomski, P. J., Vellone, D., Evanczyk, R., LeWinter, A., Birkeland, K., & Finnegan, D. C. (2014). Mapping starting zone snow depth with a ground-based lidar to improve avalanche control and forecasting. In *Proceedings of the international snow science workshop* (pp. 101–108). https://doi.org/10.1016/j.coldregions.2015.09.002.

Deems, J. S., Painter, T. H., & Finnegan, D. C. (2013). LiDAR measurement of snow depth: a review. *Journal of Glaciology*, *59*(215), 467–479. https://doi.org/10.3189/2013JoG12J154.

Dozier, J. (1989a). Remote sensing of snow in visible and near-infrared wavelengths. *Theory and applications of optical remote sensing*, 527–547. https://cir.nii.ac.jp/crid/1573387450577424128.

Dozier, J. (1989b). Spectral signature of alpine snow cover from the landsat thematic mapper. *Remote sensing of environment*, *28*, 9–22. https://doi.org/10.1016/0034-4257(89)90101-6.

EAWS. (2024). *Standard: Avalanche Size.* Retrieved from https://www.avalanches.org/standards/avalanche-size/ (Accessed January 26, 2024)

Eckerstorfer, M., Bühler, Y., Frauenfelder, R., & Malnes, E. (2016). Remote sensing of snow avalanches: Recent advances, potential, and limitations. *Cold Regions Science and Technology*, *121*, 126–140. https://doi.org/10.1016/j.coldregions.2015.11.001.

Eckerstorfer, M., & Malnes, E. (2015). Manual detection of snow avalanche debris using high-resolution Radarsat-2 SAR images. *Cold Regions Science and Technology*, *120*, 205–218. https://doi.org/10.1016/j.coldregions.2015.08.016.

Eckert, N., Keylock, C., Bertrand, D., Parent, E., Faug, T., Favier, P., & Naaim, M. (2012). Quantitative risk and optimal design approaches in the snow avalanche field: Review and extensions. *Cold Regions Science and Technology*, *79*, 1–19. https://doi.org/10.1016/j.coldregions.2012.03.003.

Elachi, C., & Van Zyl, J. J. (2021). *Introduction to the physics and techniques of remote sensing*. John Wiley & Sons.

Engeset, R., Landrø, M., Indreiten, M., Müller, K., Mikkelsen, O., & Hoseth, K. (2020). *Avalanche warning in Svalbard.* (No. 35). NVE.

European Avalanche Warning Services. (2022). *EAWS: Determination of the avalanche danger level in regional avalanche forecasting.* https://www.avalanches.org/wp-content/uploads/2022/12/EAWS_matrix_definitions_EN.pdf. (Last accessed: 21 June 2023)

Fierz, C., Armstrong, R. L., Durand, Y., Etchevers, P., Greene, E., McClung, D. M., ... Sokratov, S. A. (2009). *The International Classification for Seasonal*

Snow on the Ground. IHP-VII Technical Documents in Hydrology N°83, IACS Contribution N°1, UNESCO-IHP, Paris.

Font, D., Naaim-Bouvet, F., & Roussel, M. (1998). Drifting-snow acoustic detector: Experimental tests in La Molina, Spanish Pyrenees. *Annals of Glaciology*, *26*, 221–224. https://doi.org/10.3189/1998AoG26-1-221-224.

Frauenfelder, R., Salazar, S., Dahle, H., Humstad, T., Solbakken, E., McCormack, E., ... Lorand, P. (2022). Field test of UAS to support avalanche monitoring. Geohazard Survey from Air (GEOSFAIR) - Report from field test at Fonnbu March 2022. (873). https://hdl.handle.net/11250/3031897.

Gibson, P., et al. (2013). *Introductory remote sensing principles and concepts*. Routledge.

Haddad, A., Hendrikx, J., Humstad, T., Solbakken, E., Johnson, J., & Sproles, E. A. (2023). Quantifying the impact of new data streams in avalanche forecasting. In *Proceedings of the International Snow Science Workshop (ISSW)*.

Hall, D. K., Riggs, G. A., Salomonson, V. V., DiGirolamo, N. E., & Bayr, K. J. (2002). MODIS snow-cover products. *Remote sensing of Environment*, *83*(1-2), 181–194. https://doi.org/10.1016/S0034-4257(02)00095-0.

Hancock, H., Hendrikx, J., Eckerstorfer, M., & Wickström, S. (2021). Synoptic control on snow avalanche activity in central Spitsbergen. *The Cryosphere*, *15*(8), 3813–3837. https://doi.org/10.5194/tc-15-3813-2021.

Hao, J., Mind'je, R., Feng, T., & Li, L. (2021). Performance of snow density measurement systems in snow stratigraphies. *Hydrology Research*, *52*(4), 834–846. https://doi.org/10.2166/nh.2021.133.

Hopfinger, E., & Tochon-Danguy, J.-C. (1977). A model study of powder-snow avalanches. *Journal of Glaciology*, *19*(81), 343–356. https://doi.org/10.3189/S0022143000029373.

Huang, N., & Shi, G. (2017). The significance of vertical moisture diffusion on drifting snow sublimation near snow surface. *The Cryosphere*, *11*(6), 3011–3021. https://doi.org/10.5194/tc-11-3011-2017.

ISAW. (2024a). *FlowCapt sensor - FC4*. Retrieved from https://www.isaw-products.com/flowcapt-fc4/ (Accessed January 26, 2024)

ISAW. (2024b). *ISAW User Guide*. Retrieved from https://www.isaw-products.com/wp-content/uploads/2023/03/21-ISAW

_User_Guide_V2.18.pdf (Accessed January 26, 2024)

Issler, D., Gisnås, K. G., Gauer, P., Glimsdal, S., Domaas, U., & Sverdrup-Thygeson, K. (2023). NAKSIN - A New Approach to Snow Avalanche Hazard Indication Mapping in Norway. *Available at SSRN 4530311*. http://dx.doi.org/10.2139/ssrn.4530311.

Ito, Y., Naaim-Bouvet, F., Nishimura, K., Bellot, H., Thibert, E., Ravanat, X., & Fontaine, F. (2017). Measurement of snow particle size and velocity in avalanche powder clouds. *Journal of Glaciology*, *63*(238), 249–257. https://doi.org/10.1017/jog.2016.130.

Jaedicke, C. (2001). Acoustic snowdrift measurements: Experiences from the FlowCapt instrument. *Cold Regions Science and Technology*, *32*(1), 71–81. https://doi.org/10.1016/S0165-232X(01)00017-9.

Jaedicke, C., Studeregger, A., Monti, F., Dellavedova, P., Stoffel, L., Azzarello, S., ... Bellido, G. M. (2018). Local avalanche warning in Europe. In *Proceedings of the International Snow Science Workshop (ISSW), Innsbruck, Austria, 2018*. http://hdl.handle.net/11250/2583854.

Jaedicke, C., Syre, E., & Sverdrup-Thygeson, K. (2014). GIS-aided avalanche warning in Norway. *Computers & Geosciences*, *66*, 31–39. https://doi.org/10.1016/j.cageo.2014.01.004.

Jekich, B. M., Drake, B. D., Nacht, J. Y., Nichols, A., Ginde, A. A., & Davis, C. B. (2016). Avalanche fatalities in the United States: a change in demographics. *Wilderness & environmental medicine*, *27*(1), 46–52. https://doi.org/10.1016/j.wem.2015.11.004.

Judson, A., & Doesken, N. (2000). Density of freshly fallen snow in the central Rocky Mountains. *Bulletin of the American Meteorological Society*, *81*(7), 1577–1588. https://doi.org/10.1175/1520-0477(2000)081<1577:DOFFSI>2.3.CO;2.

Kapper, K. L., Goelles, T., Muckenhuber, S., Trügler, A., Abermann, J., Schlager, B., ... others (2023). Automated snow avalanche monitoring for Austria: State of the art and roadmap for future work. *Frontiers in Remote Sensing*, *4:1156519*. https://doi.org/10.3389/frsen.2023.1156519.

Klever, N. (1985). Air and water-vapour convection in snow. *Annals of glaciology*, *6*, 39–42. https://doi.org/10.3189/1985AoG6-1-39-42.

Kobayashi, D. (1972). Studies of snow transport in low-level drifting snow.

Contributions from the Institute of Low Temperature Science, *24*, 1–58. http://hdl.handle.net/2115/20236.

Kotlyakov, V. (1961). Results of a study of the processes of formation and structure of the upper layer of the ice sheet in eastern Antarctica. *IASH Publ*, *55*(88-99), 41.

Kronthaler, G., & Zenke, B. (2006). Schneedeckendiagnose-... zur beurteilung der lawinengefahr. *Bergundsteigen*, *4*(06), 56–64.

Lang, R., Leo, B., & Brown, R. (1984). Observations on the growth process and strength characteristics of surface hoar. In *Proceedings of the International Snow Science Workshop* (pp. 188–195).

Larsen, J. O. (1998). Snow-creep forces on masts. *Annals of Glaciology*, *26*, 19–21. https://doi.org/10.3189/1998AoG26-1-19-21.

Lehning, M., & Fierz, C. (2008). Assessment of snow transport in avalanche terrain. *Cold Regions Science and Technology*, *51*(2-3), 240–252. https://doi.org/10.1016/j.coldregions.2007.05.012.

Lehning, M., Naaim, F., Naaim, M., Brabec, B., Doorschot, J., Durand, Y., ... Zimmerli, M. (2002). Snow drift: acoustic sensors for avalanche warning and research. *Natural Hazards and Earth System Sciences*, *2*(3/4), 121–128. https://doi.org/10.5194/nhess-2-121-2002.

Li, L., & Pomeroy, J. W. (1997). Estimates of threshold wind speeds for snow transport using meteorological data. *Journal of Applied Meteorology*, *36*(3), 205–213. https://doi.org/10.1175/1520-0450(1997)036<0205:EOTWSF>2.0.CO;2.

Li, W., Liu, G., Cui, X., & Lu, M. (2021). Feature-aided RTK/LiDAR/INS integrated positioning system with parallel filters in the ambiguity-position-joint domain for urban environments. *Remote Sensing*, *13*(10), 2013. https://doi.org/10.3390/rs13102013.

Libbrecht, K. G. (2005). The physics of snow crystals. *Reports on progress in physics*, *68*(4), 855. https://doi.org/10.1088/0034-4885/68/4/R03.

Libbrecht, K. G. (2007). The formation of snow crystals: subtle molecular processes govern the growth of a remarkable variety of elaborate ice structures. *American Scientist*, *95*(1), 52–59. https://www.jstor.org/stable/27858900.

Lied, K. (1976). Snøskred og vurdering av snøskredfare (Avalanches and assessment of avalanche danger). *NGI Articles*. https://hdl.handle.net/11250/3100062.

Lied, K. (1998). Snow avalanche experience through 25 years at NGI. *NGI Articles*. https://hdl.handle.net/11250/3082351.

Lied, K., & Bakkehøi, K. (1980). Empirical calculations of snow–avalanche run–out distance based on topographic parameters. *Journal of Glaciology*, *26*(94), 165–177. https://doi.org/10.3189/S0022143000010704.

Lied, K., & Kristensen, K. (2003). *Snøskred: Håndbok om snøskred (Avalanches: Handbook on avalanches)*. Norwegian Geotechnical Institute (NGI).

Liu, X. (2008). Airborne LiDAR for DEM generation: some critical issues. *Progress in physical geography*, *32*(1), 31–49. https://doi.org/10.1177/0309133308089496.

Margreth, S. (2007). *Defense Structures in Avalanche Starting Zones. Technical Guideline as an Aid to Enforcement* (No. 0704). Federal Office for the Environment, Bern; WSL Swiss Federal, Institute for Snow and Avalanche Research SLF, Davos. 134 pp.

Mason, B. (1961). The growth of snow crystals. *Scientific American*, *204*(1), 120–133. https://www.jstor.org/stable/24940745.

McClung, D. (2016). Avalanche character and fatalities in the high mountains of Asia. *Annals of Glaciology*, *57*(71), 114–118. https://doi.org/10.3189/2016AoG71A075.

McClung, D., & Schaerer, P. A. (2006). *The avalanche handbook*. The Mountaineers Books.

McCormack, E., Dahle, H., Dupuy, B., Frauenfelder, R., Hellandsvik, A., Hendrikx, J., ... Vaa, T. (2024). Avalanche Hazard Assessment Supported by UAS. *NPRA Reports*. https://hdl.handle.net/11250/3117653.

Mellor, M. (1965). Blowing snow. https://doi.org/10.21236/AD0630328.

Mellor, M. (1974). *A review of basic snow mechanics*. US Army Cold Regions Research and Engineering Laboratory Hanover, NH. http://hdl.handle.net/11681/2625.

Michaux, J., Naaim-Bouvet, F., & Naaim, M. (2000). The acoustic snowdrift

sensor: interests, calibration and results. In *International Snow Science Workshop Big Sky, Montana, USA, 1-6. October 2000* (pp. 390–395). https://hal.inrae.fr/hal-02579576.

Müller, K., Techel, F., & Mitterer, C. (2024). An updated EAWS matrix to determine the avalanche danger level: derivation, usage, and consistency. *Natural Hazards and Earth System Sciences Discussions*, *2024*, 1–44. https://doi.org/10.5194/nhess-2024-48.

Müller, K., Techel, F., Mitterer, C., Feistl, T., Sofia, S., Roux, N., . . . Bertranda, L. (2023). The EAWS Matrix, A Look-up Table for Regional Avalanche Danger Level Assessment, and its Underlying Concept. In *Proceedings, International Snow Science Workshop, Bend, Oregon, 2023* (p. 7).

Naaim, M., Faug, T., Thibert, E., Eckert, N., Chambon, G., Naaim, F., & Bellot, H. (2008). Snow avalanche pressure on obstacles. In *Proceedings whistler 2008 international snow science workshop september 21-27, 2008* (p. 740).

NCCS. (2024). *Norwegian Centre for Climate Services - Observations and Weather Statistics.* Retrieved from https://www.xgeo.no/ (Accessed February 25, 2024)

Nemoto, M., & Nishimura, K. (2004). Numerical simulation of snow saltation and suspension in a turbulent boundary layer. *Journal of Geophysical Research: Atmospheres*, *109*(D18). https://doi.org/10.1029/2004JD004657.

Nolin, A. W. (2010). Recent advances in remote sensing of seasonal snow. *Journal of Glaciology*, *56*(200), 1141–1150. https://doi.org/10.3189/002214311796406077.

Norem, H. (1974). *Utforming av veger i drivsnøområder (design of roads in drift snow areas)* (Unpublished master's thesis). Norges Tekniske Høgskole, Trondheim.

Norem, H. (1975a). Utforming av veger i drivsnøområder (design of roads in drift snow areas). *Notes from the Road Directorate*(49).

Norem, H. (1975b). Utforming og lokalisering av snøskjermer (Design and placement of snow fences). *Notes from the Road Directorate*(49).

Norem, H., & Sandersen, F. (2012). Flom-og sørpeskred: Høringsutgave av veileder (Flood- and mudslides: Consultation edition of guidebook).

NVE. (2011). *Utvikling av regional snøskredvarsling - Rapport fra det første året*

(Development of regional snow avlanche warning - Report from the first year) (No. 12/2011). (Engeset, R., Bjørlien, J, Ekker, R, Humstad, T. Jaedicke, C., Kronholm, K., Müller, K., Rustad, B., Seierstad, I., Schuler, D, Taurisano, A.)

NVE. (2013). *Snøskredvarslingen - Evaluering av vinteren 2013 (Snow Avalanche Warning - Evaluation of the winter 2013)* (No. 65/2013). (Müller, K., Kosberg, S, Barfod, E., Rustad, B., Landrø, M.)

NVE. (2020a). *Assessment of Avalanche Safety in Steep Terrain - Assessment of Avalanche Danger in Planning and Building Cases.* Retrieved from https://veiledere.nve.no/utredning-av-sikkerhet-mot-skred-i-bratt-terreng/ (Accessed May 12, 2024)

NVE. (2020b). *Snøomvandling (Snow Metamorphism)* (No. 01/2020). https://publikasjoner.nve.no/faktaark/2020/faktaark2020_01.pdf. (Fact sheet)

NVE. (2021). Evaluering av Nordnorsk Skredovervåking (NNSO) (Evaluation of northern-Norway Avalanche monitoring (NNSO). (16/2021). (Bergbjørn, Karin and Gundersen, Jeanette)

NVE. (2024a). *NVE Atlas.* Retrieved from https://atlas.nve.no/ (Accessed February 22, 2024)

NVE. (2024b). *NVE - Map Catalog.* Retrieved from https://kartkatalog.nve.no/#kart (Accessed February 22, 2024)

NVE. (2024c). *NVE - Thematic Maps: Avalanche Events.* Retrieved from https://temakart.nve.no/tema/skredhendelser (Accessed February 22, 2024)

NVE. (2024d). *Skredregistrering.* Retrieved from https://www.skredregistrering.no/ (Accessed February 22, 2024)

Øien, K., & Albrechtsen, E. (2022). *Lokalt snøskredvarsel for Longyearbyen - Evaluering av nåværende system (Local snow avalanche warning for Longyearbyen - Evaluation of the current system)* (Tech. Rep.). https://hdl.handle.net/11250/3055189.

Powers, D., O'Neill, K., & Colbeck, S. (1985a). Theory of natural convection in snow. *Journal of Geophysical Research: Atmospheres*, *90*(D6), 10641–10649. https://doi.org/10.1029/JD090iD06p10641.

Powers, D., O'Neill, K., & Colbeck, S. (1985b). Thermal convection in snow. https://hdl.handle.net/11681/9395.

Prokop, A. (2008). Assessing the applicability of terrestrial laser scanning for spatial snow depth measurements. *Cold Regions Science and Technology*, *54*(3), 155–163. https://doi.org/10.1016/j.coldregions.2008.07.002.

Proksch, M., Rutter, N., Fierz, C., & Schneebeli, M. (2016). Intercomparison of snow density measurements: bias, precision, and vertical resolution. *The Cryosphere*, *10*(1), 371–384. https://doi.org/10.5194/tc-10-371-2016.

Radlwimmer, A. L. (2023). *Snow Depth around Longyearbyen, Svalbard* (Unpublished master's thesis). NTNU.

Ramseier, R. O., & Keeler, C. M. (1966). The sintering process in snow. *Journal of Glaciology*, *6*(45), 421–424. https://doi.org/10.3189/S0022143000019535.

Rango, A., & Itten, K. (1976). Satellite potentials in snowcover monitoring and runoff prediction. *Hydrology Research*, *7*(4), 209–230. https://doi.org/10.2166/nh.1976.0014.

Reutz, E. H., Frauenfelder, R., & Salazar, S. (2022). Consolidation of requirements - analysis of questionnaire. *NGI Reports*. https://hdl.handle.net/11250/3033519.

Rynning, E. K. (2019). *Snow measurements with drones* (Unpublished master's thesis). NTNU.

Salazar, S., Dahle, H., Dupuy, B., Frauenfelder, R., Grøver, A., Humstad, T., ... others (2023). Multisensor uas testing to support avalanche forecasting and monitoring. In *84th eage annual conference & exhibition* (Vol. 2023, pp. 1–5). https://doi.org/10.3997/2214-4609.2023101236.

Salazar, S. E., Frauenfelder, R., Humstad, T., & McCormack, E. (2023). Geohazard monitoring by uav: The future technology for remote decision support. *GeoStrata Magazine Archive*, *27*(2), 48–54. https://doi.org/10.1061/geosek.0000475.

Sasano, Y., & Browell, E. V. (1989). Light scattering characteristics of various aerosol types derived from multiple wavelength lidar observations. *Applied optics*, *28*(9), 1670–1679. https://doi.org/10.1364/AO.28.001670.

Sato, N., & Kikuchi, K. (1985). Formation mechanisms of snow crystals at low temperature. *Annals of Glaciology*, *6*, 232–234. https://doi.org/10.3189/1985AoG6-1-232-234.

Sato, T., Mochizuki, S., Kosugi, K., & Nemoto, M. (2005). Effects of particle shape on mass flux measurement of drifting snow by snow particle counter. *Journal of the Japanese Society of Snow and Ice*, *67*(6), 493–503. https://doi.org/10.5331/seppyo.67.493.

Schauer, A. R., Hendrikx, J., Birkeland, K. W., & Mock, C. J. (2021). Synoptic atmospheric circulation patterns associated with deep persistent slab avalanches in the western United States. *Natural Hazards and Earth System Sciences*, *21*(2), 757–774. https://doi.org/10.5194/nhess-21-757-2021 .

Schweizer, J. (1999). Review of dry snow slab avalanche release. *Cold Regions Science and Technology*, *30*(1-3), 43–57. https://doi.org/10.1016/S0165-232X(99)00025-7.

Schweizer, J., Bruce Jamieson, J., & Schneebeli, M. (2003). Snow avalanche formation. *Reviews of Geophysics*, *41*(4). https://doi.org/10.1029/2002RG000123.

Schweizer, J., & Jamieson, J. (2001). Snow cover properties for skier triggering of avalanches. *Cold Regions Science and Technology*, *33*(2-3), 207–221. https://doi.org/10.1016/S0165-232X(01)00039-8.

Schweizer, J., Kronholm, K., Jamieson, J. B., & Birkeland, K. W. (2008). Review of spatial variability of snowpack properties and its importance for avalanche formation. *Cold Regions Science and Technology*, *51*(2-3), 253–272. https://doi.org/10.1016/j.coldregions.2007.04.009.

Skred AS. (2022). *Fv. 53 Tyin-Årdal, kritiske skredstørrelser som kan nå veg (County Road 53 Tyin-Årdal, critical fracture heights that can reach the road)* (No. 21384-04-1). (Nordbrøden, H.)

Skred AS. (2023a). *Skredvarsel for Fv53 Tyin-Årdal, 12-13th Feb. (Avalanche warning for County Road 53 Tyin-Årdal, 12-13th Feb.)*. (Nordbrøden, H.)

Skred AS. (2023b). *Snødriftsensor – Snødrift som beslutningsverktøy for lokal skredvarsling (Snowdrift sensor - Snowdrift as a decision-making tool for local snow avalanche warning)* (No. 22503-02-1). (Walberg, N. A. and Wickström, S.)

Skred AS. (2024a). *Operativ drift av aktiv skredkontroll på Fv. 53 Tyin-Årdal (Operation of active avalanche control at County Road 53 Tyin-Årdal)*. Retrieved [February 23, 2024], from https://skred.as/prosjekter/operativ-drift-av-aktiv-skredkontroll-pa-fv-53-tyin-ardal/

Skred AS. (2024b). *Skredvarsel for Fv53 Tyin-Årdal, 5-6th Feb. (Avalanche warning for County Road 53 Tyin-Årdal, 5-6th Feb.)*. (Grue, H.)

Skred AS - Varsom Regobs. (2023a). *Overview Avalanche Control at Tyin and Tyinslinna 13 February*. Retrieved from https://www.regobs.no/?FromDate=2023-02-12T23:00:00.000Z&ToDate=2023-02-13T22:59:59.999Z&GeoHazards=10&NWLat=61.290714875573556&NWLon=7.9586097912585965&SELat=61.196238485226814&SELon=8.44063493774297 (Accessed January 28, 2024)

Skred AS - Varsom Regobs. (2023b). *Overview Avalanche Control at Tyin and Tyinslinna 21 February*. Retrieved from https://www.regobs.no/?FromDate=2023-02-20T23:00:00.000Z&ToDate=2023-02-21T22:59:59.999Z&GeoHazards=10&NWLat=61.28889653881&NWLon=7.927073444652591&SELat=61.19441467658618&SELon=8.409098591136967 (Accessed January 28, 2024)

Skred AS - Varsom Regobs. (2024). *Avalanche Event - Støl B*. Retrieved from https://www.regobs.no/registration/374190 (Accessed May 14, 2024)

Solbakken, E. (2019). *Snow surface mapping and change detection in avalanche release areas using a consumer-grade UAS and SfM photogrammetry* (Unpublished master's thesis). NTNU.

Sommerfeld, R., & LaChapelle, E. (1970). The classification of snow metamorphism. *Journal of Glaciology*, *9*(55), 3–18. https://doi.org/10.3189/S0022143000026757.

Sovilla, B., Kern, M., & Schaer, M. (2010). Slow drag in wet-snow avalanche flow. *Journal of Glaciology*, *56*(198), 587–592. https://doi.org/10.3189/002214310793146287.

Sovilla, B., McElwaine, J. N., Schaer, M., & Vallet, J. (2010). Variation of deposition depth with slope angle in snow avalanches: Measurements from vallée de la sionne. *Journal of Geophysical Research: Earth Surface*, *115*(F2). https://doi.org/10.1029/2009JF001390.

Statens Vegvesen. (2014a). *Veger og drivsnø: Veiledning (Roads and drifting snow: Guidelines)* (Vol. 137). http://hdl.handle.net/11250/2606233. Vegdirektoratet. (Manual)

Statens Vegvesen. (2014b). *Veger og snøskred (Roads and snow avalanches)* (Vol. N-V138). https://viewers.vegnorm.vegvesen.no/

product/859996?langUI=nb&filePath=f9489450-8ebb-4cb2-80dd-91e35a017d30.pdf&fileType=Pdf. Vegdirektoratet. (Manual)

Statens Vegvesen. (2021). *Lidar on UAS to support avalanche monitoring - Findings from demonstration in Trollstigen, October 2021* (Vol. 825). https://hdl.handle.net/11250/2999621. Norwegian Public Roads Administration (NPRA). (Solbakken, E., Humstad, T., Dahle, H., Vaa, T., Andreassen, D.T., Nilssen, K. M., Skjetne, C., Frauenfelder, R., Salazar, S.)

Stoffel, L., & Schweizer, J. (2008). Guidelines for avalanche control services: organization, hazard assessment and documentation–an example from Switzerland. In *Proceedings International Snow Science Workshop (ISSW)* (pp. 483–489). https://arc.lib.montana.edu/snow-science/objects/P__8134.pdf.

Swinbank, W. C. (1963). Long-wave radiation from clear skies. *Quarterly Journal of the Royal Meteorological Society*, *89*(381), 339–348. https://doi.org/10.1002/qj.49708938105.

Tabler, R. D. (1994). *Design guidelines for the control of blowing and drifting snow* (Vol. 364). Strategic Highway Research Program, National Research Council Washington, DC.

Tabler, R. D. (2003). *Controlling blowing and drifting snow with snow fences and road design* (Tech. Rep.).

Tabler, R. D., Pomeroy, J., & Santana, B. (1990). Drifting snow. *Cold Regions Hydrology and Hydraulics. American Society of Civil Engineers, New York. 1990. p 95-145, 12 fig, 3 tab, 122 ref*.

Tanaka, M., Girard, G., Davis, R., Peuto, A., & Bignell, N. (2001). Recommended table for the density of water between 0 c and 40 c based on recent experimental reports. *Metrologia*, *38*(4), 301. https://doi.org/10.1088/0026-1394/38/4/3.

Techel, F., & Pielmeier, C. (2011). Point observations of liquid water content in wet snow–investigating methodical, spatial and temporal aspects. *The Cryosphere*, *5*(2), 405–418. https://doi.org/10.5194/tc-5-405-2011.

Tedesco, M. (2015). Remote sensing and the cryosphere. *Remote Sensing of the Cryosphere*, 1–16. https://doi.org/10.1002/9781118368909.ch1.

Thordarson, S. (2002). *Wind flow studies for drifting snow on roads* (Doctoral dissertation, NTNU - Faculty of Engineering and Technology). http://

hdl.handle.net/11250/231332.

Trouvilliez, A., Naaim-Bouvet, F., Bellot, H., Genthon, C., & Gallée, H. (2015). Evaluation of the FlowCapt acoustic sensor for the aeolian transport of snow. *Journal of Atmospheric and Oceanic Technology*, *32*(9), 1630–1641. https://doi.org/10.1175/JTECH-D-14-00104.1.

Tveit, J. (2018). *Vurdering av snøskjermar ved Tyinstølen (Evaluation of snow fences at Tyinstølen)* (No. 30844-GEOL-1). (Note by the NPRA)

Upadhyay, A., Kumar, A., & Chaudhary, A. (2010). Velocity measurements of wet snow avalanche on the dhundi snow chute. *Annals of glaciology*, *51*(54), 139–145. https://doi.org/10.3189/172756410791386580.

Van Herwijnen, A., & Miller, D. A. (2013). Experimental and numerical investigation of the sintering rate of snow. *Journal of Glaciology*, *59*(214), 269–274. https://doi.org/10.3189/2013JoG12J094.

Varsom. (2024). *Avalanche problems.* Retrieved from https://www.varsom.no/en/avalanches/about-avalanches/avalanche-problems/ (Accessed February 20, 2024)

Varsom Regobs. (2024). *Varsom Regobs.* Retrieved from https://www.regobs.no/ (Accessed January 27, 2024)

Varsom Xgeo. (2024). *Varsom Xgeo.* Retrieved from https://www.xgeo.no/ (Accessed February 22, 2024)

Vera Valero, C., Wever, N., Christen, M., & Bartelt, P. (2018). Modeling the influence of snow cover temperature and water content on wet-snow avalanche runout. *Natural Hazards and Earth System Sciences*, *18*(3), 869–887. https://doi.org/10.5194/nhess-18-869-2018.

Vionnet, V., Guyomarc'h, G., Lafaysse, M., Naaim-Bouvet, F., Giraud, G., & Deliot, Y. (2018). Operational implementation and evaluation of a blowing snow scheme for avalanche hazard forecasting. *Cold Regions Science and Technology*, *147*, 1–10. https://doi.org/10.1016/j.coldregions.2017.12.006.

Wallace, L., Lucieer, A., Watson, C., & Turner, D. (2012). Development of a uav-lidar system with application to forest inventory. *Remote sensing*, *4*(6), 1519–1543. https://doi.org/10.3390/rs4061519.

Wasser, L. (2018). *Earth analytics course in the R programming language (r-earth-analytics)*. https://doi.org/10.5281/zenodo.1326873. Zenodo.

Wei, G., Shalei, S., Bo, Z., Shuo, S., Faquan, L., & Xuewu, C. (2012). Multi-wavelength canopy lidar for remote sensing of vegetation: Design and system performance. *ISPRS Journal of Photogrammetry and Remote Sensing*, *69*, 1–9. https://doi.org/10.1016/j.isprsjprs.2012.02.001.

Wise, S. (2018). *GIS basics*. CRC Press.

Wyssen Norge AS. (2020). *Sesongrapport 2019/2020 - Forebyggende skredkontroll Fv.53 Tyin-Årdal (Seasonal report 2019/2020 - Preventative avalanche control County Road 53 Tyin-Årdal)* (No. CPSO99-6).

Wyssen Norge AS. (2021). *Sesongrapport 2020/2021 - Forebyggende skredkontroll Fv.53 Tyin-Årdal (Seasonal report 2020/2021 - Preventative avalanche control County Road 53 Tyin-Årdal)* (No. CPSO130-6).

Wyssen Norge AS. (2023). *Remote Avalanche Control System for public road in Norway*. https://www.wyssenavalanche.com/wp-content/uploads/2023/05/NO_RACS-for-public-road-in-Norway_EN_V.2.pdf.

Zhang, W., He, J., Chen, A., Wu, X., & Shen, Y. (2022). Observations of Drifting Snow Using FlowCapt Sensors in the Southern Altai Mountains, Central Asia. *Water*, *14*(6), 845 pp. https://doi.org/10.3390/w14060845.

Zhou, J., Pomeroy, J. W., Zhang, W., Cheng, G., Wang, G., & Chen, C. (2014). Simulating cold regions hydrological processes using a modular model in the west of China. *Journal of Hydrology*, *509*, 13–24. https://doi.org/10.1016/j.jhydrol.2013.11.013.

Appendix A

The following Tables A.1, A.2, and A.2 present values used in this study for analysis (explained in Sections 4.2.1 & 4.2.2) of snow surface change, volume change, and corrections regarding additional precipitation and FC4 data extrapolation. Important note: Values are measured between intervals (e.g. 19.02.2023 17:50−21.02.2023 09:08), and are *not* cumulative sums for previous measurements. Datasets are however later manipulated in plotting to be cumulative for given intervals.

Table A.1: Calculated mean snow surface change [m] for the defined PRAs (Results Section 5), with standard deviations (σ). Derived from LiDAR-data and subsequent GIS-analysis and python scripting. Method described in Section 4.2.1.

Date	Galden Skavl	Galden Brattheng	Støl A	Støl B	Støl C	Støl D
15.02.2023 16:31	-	-	-	-	-	-
17.02.2023 17:35	**−0.283** σ=0.373	**0.151** σ=0.141	**0.179** σ=5.044	**0.111** σ=0.143	**−0.040** σ=0.257	**−0.124** σ=0.109
19.02.2023 17:50	**0.119** σ=0.337	**0.237** σ=0.197	**0.251** σ=4.465	**0.455** σ=0.367	**0.222** σ=0.290	**0.334** σ=0.204
21.02.2023 09:08	**0.567** σ=0.400	**0.778** σ=0.462	**0.425** σ=7.027	**1.010** σ=0.505	**0.230** σ=0.354	**0.670** σ=0.284

Table A.2: Measured snow volume change [m^3] for the defined PRAs (Results Section 5). Derived from LiDAR-data and subsequent GIS-analysis. Method described in Section 4.2.2.

Date	Galden Skavl	Galden Brattheng	Støl A	Støl B	Støl C	Støl D
15.02.2023 16:31	-	-	-	-	-	-
17.02.2023 17:35	585.13	699.82	1850.89	1215.59	1090.52	1753.72
19.02.2023 17:50	1588.75	300.45	1409.81	3429.26	750.87	3333.44
21.02.2023 09:08	2471.91	2256.57	2755.91	5560.83	1871.59	5278.53

Table A.3: Measured precipitation [mm] and cumulated snowdrift [g/m^2] in intervals between measurements - *not* cumulative sum for all measurements. Precipitation measurements derived from weather station FV53 Tyinosen (Section 4.3).

Date	Precipitation [mm]	Measured snowdrift, cumulative sum [g/m^2]
15.02.2023 16:31	-	-
17.02.2023 17:35	12.3	3531.62
19.02.2023 17:50	6.6	12934.04
21.02.2023 09:08	32.6	109 651.55

Appendix B

In the following pages, plotted data of measured snowdrift from the FlowCapt 4 (FC4) and the measured deposited volume and mean surface change for each PRA are shown. Methods for deriving mean snow surface change, volumes, corrections for additional precipitation, as well as extrapolation of FC4-data are described in Sections 4.2.1, 4.2.2, and 4.4.1.

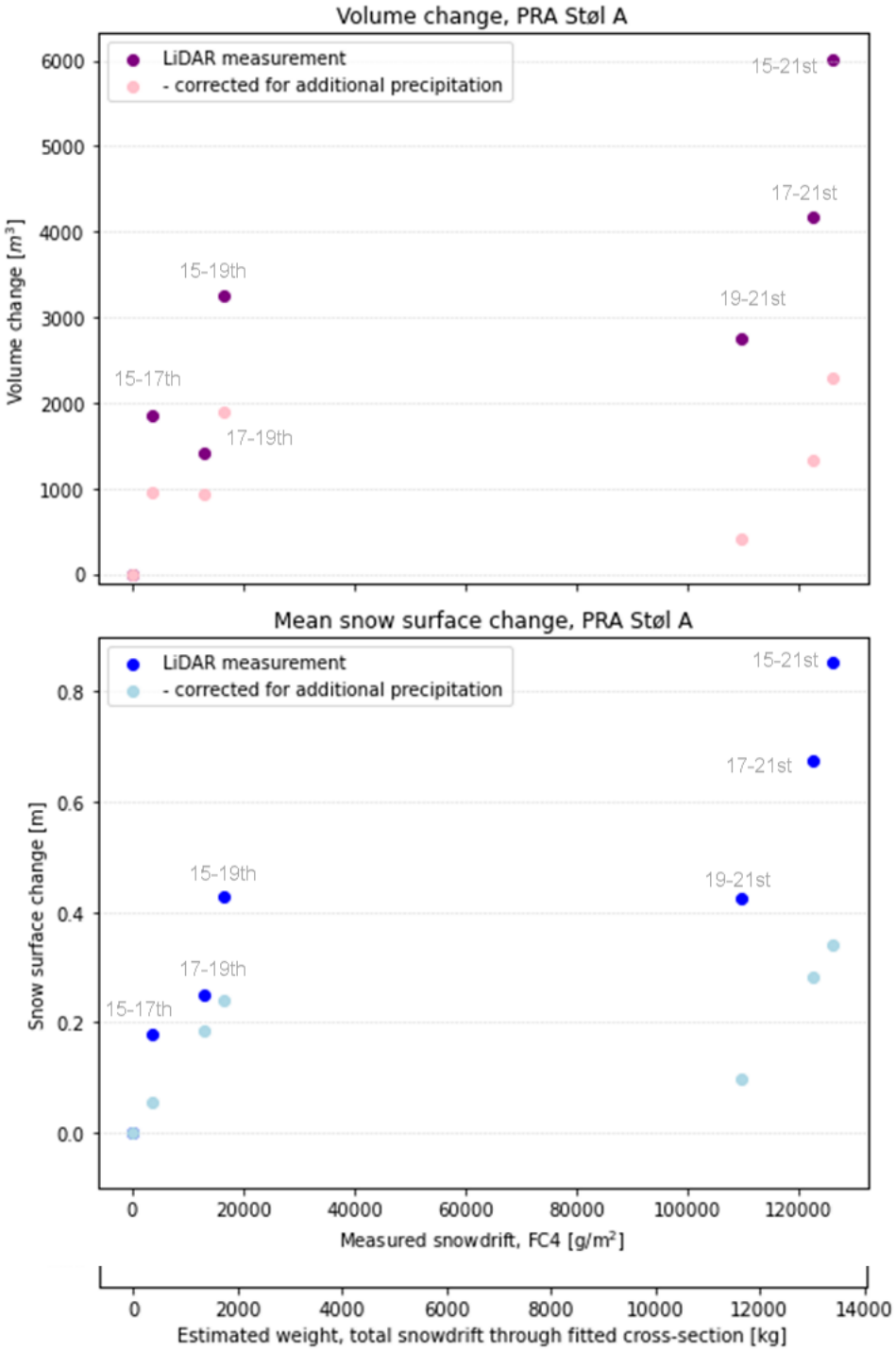

Figure B.1: First subplot: Measured volume changes and corresponding corrections for additional precipitation. **Second subplot:** Measured mean snow surface changes and corresponding corrections for additional precipitation. Data from both subplots correspond to both x-axes presented at the bottom. Data values are presented in Tables A.1 & A.2 in Appendix A.

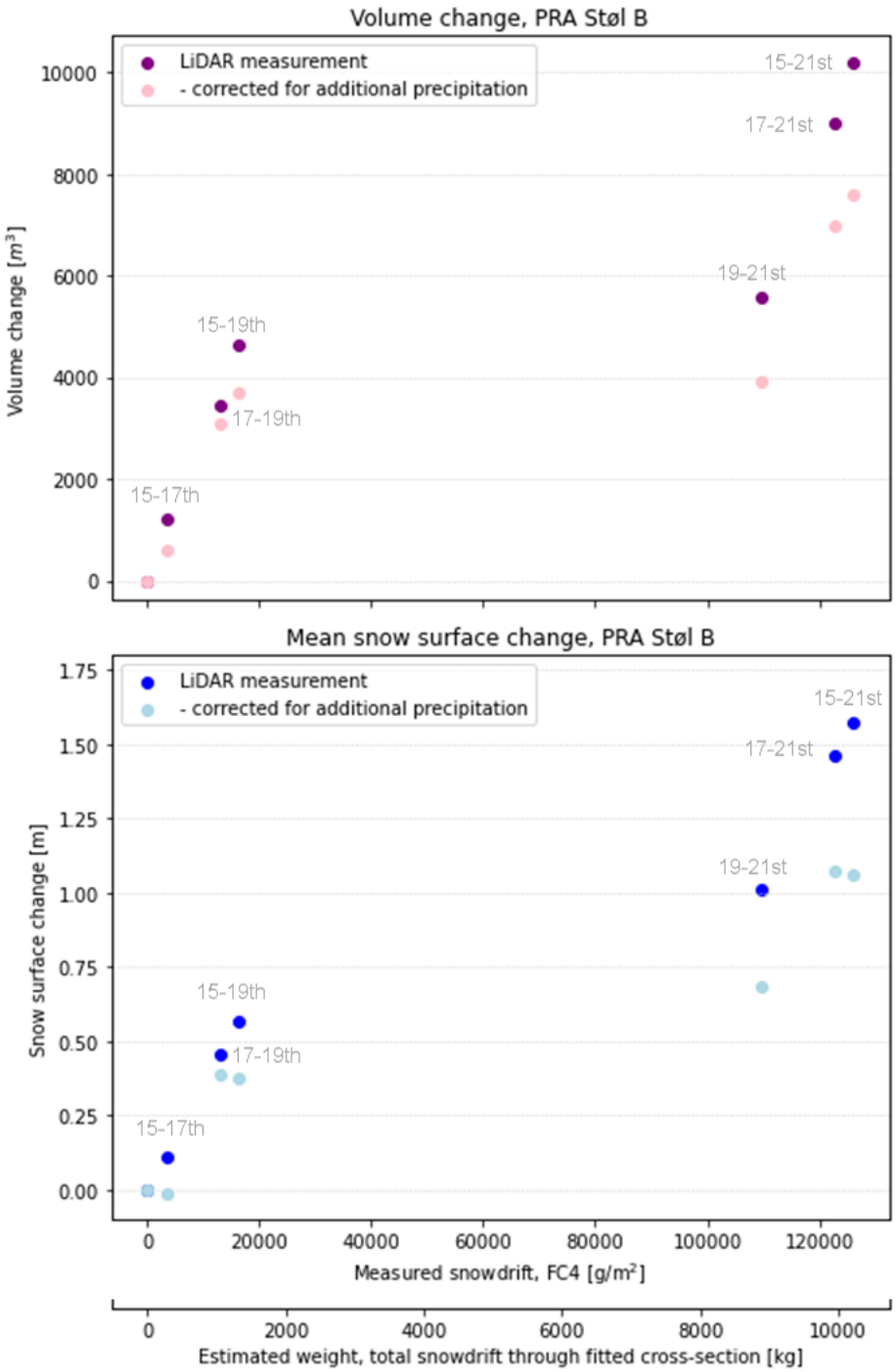

Figure B.2: First subplot: Measured volume changes and corresponding corrections for additional precipitation. **Second subplot:** Measured mean snow surface changes and corresponding corrections for additional precipitation. Data from both subplots correspond to both x-axes presented at the bottom. Data values are presented in Tables A.1 & A.2 in Appendix A.

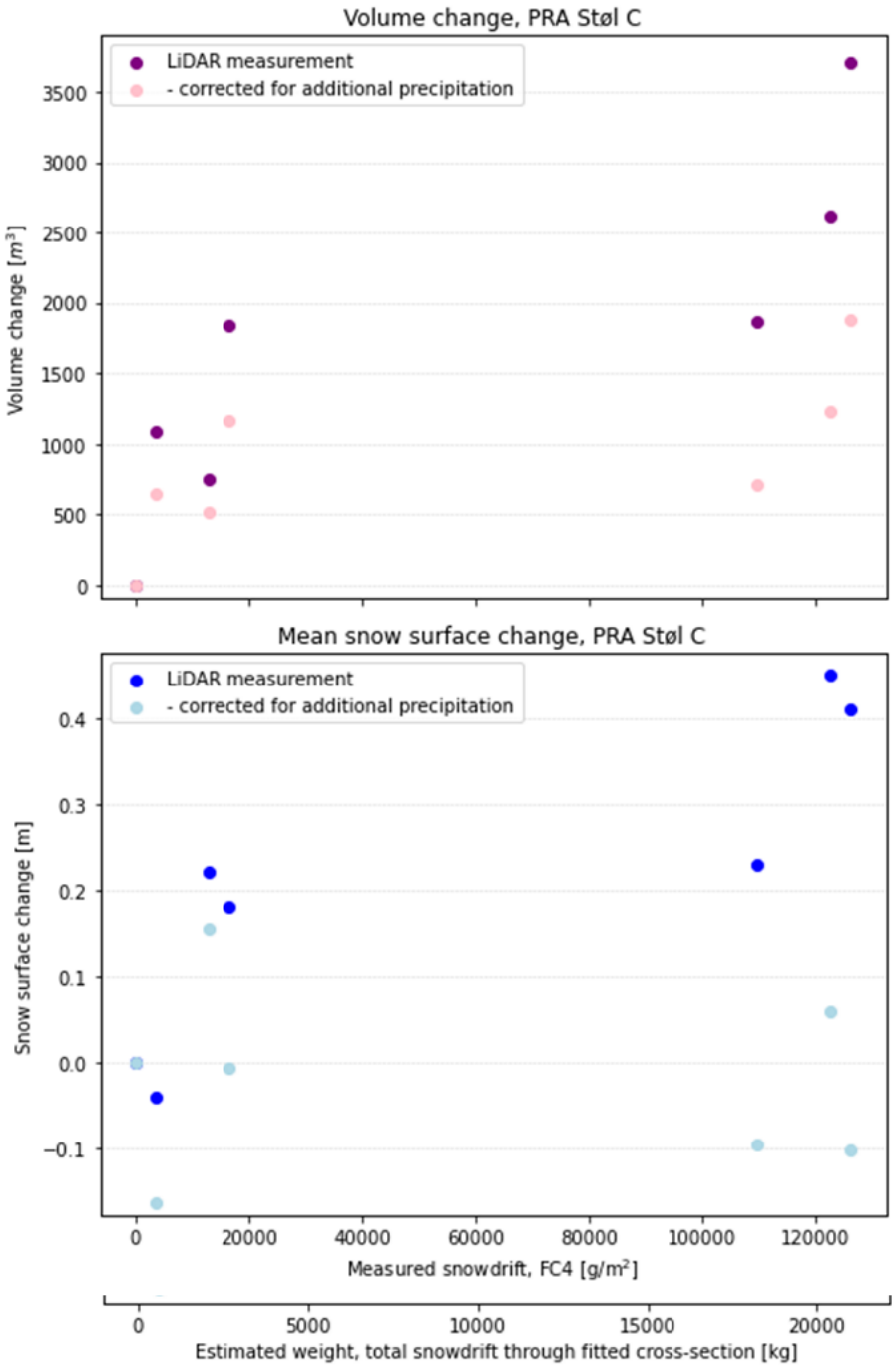

Figure B.3: First subplot: Measured volume changes and corresponding corrections for additional precipitation. **Second subplot:** Measured mean snow surface changes and corresponding corrections for additional precipitation. Data from both subplots correspond to both x-axes presented at the bottom. Data values are presented in Tables A.1 & A.2 in Appendix A.

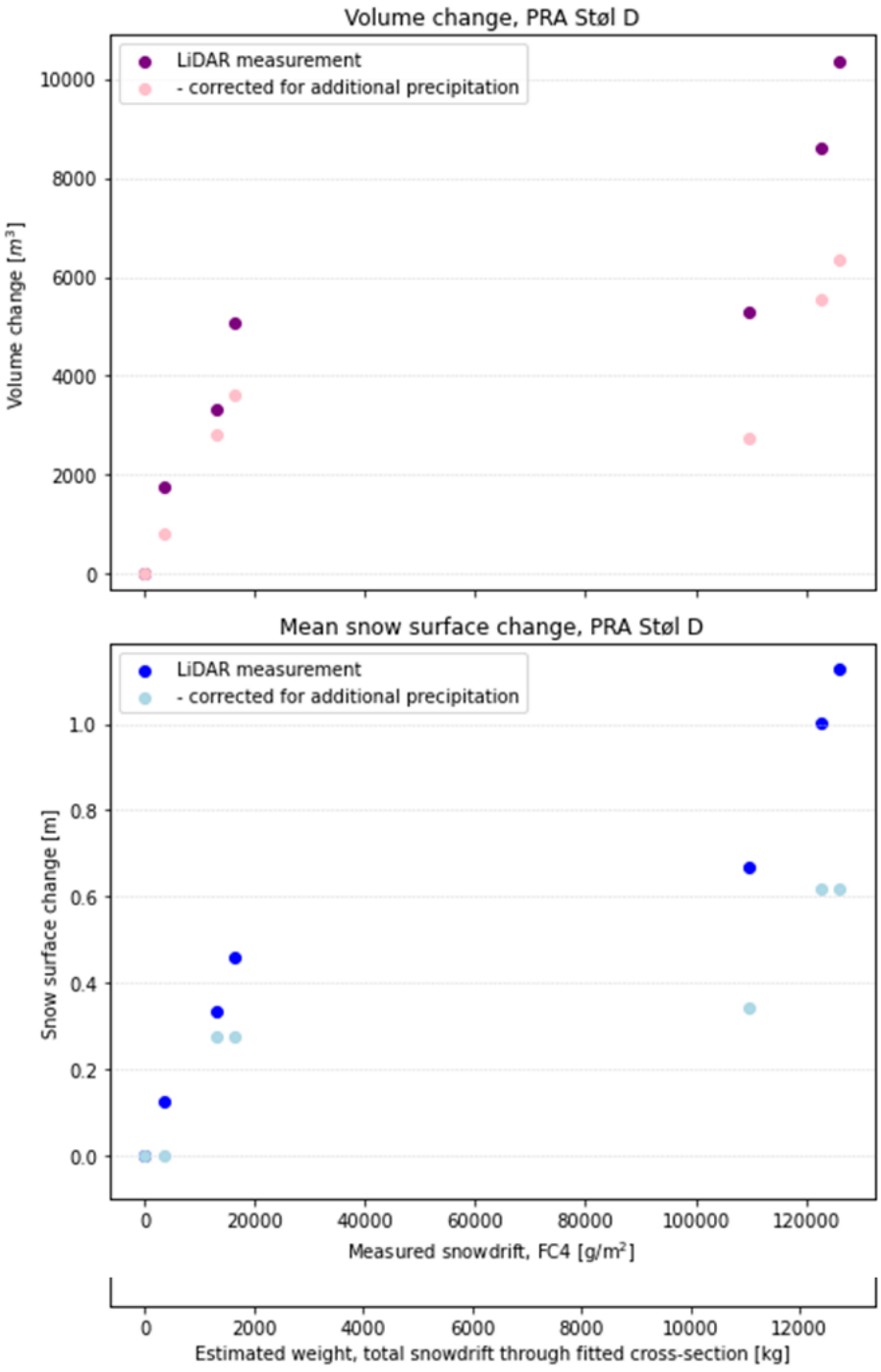

Figure B.4: First subplot: Measured volume changes and corresponding corrections for additional precipitation. **Second subplot:** Measured mean snow surface changes and corresponding corrections for additional precipitation. Data from both subplots correspond to both x-axes presented at the bottom. Data values are presented in Tables A.1 & A.2 in Appendix A.

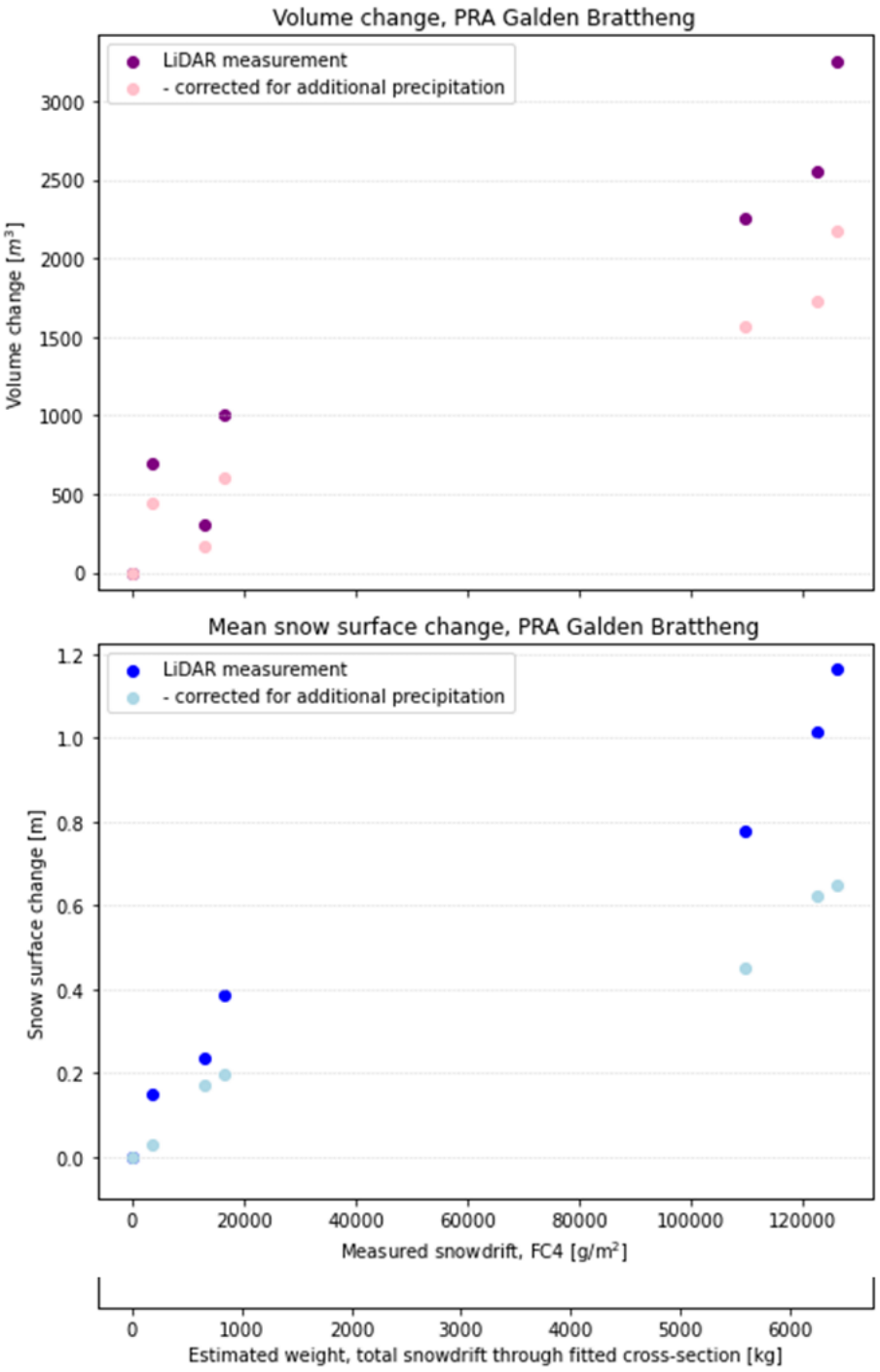

Figure B.5: First subplot: Measured volume changes and corresponding corrections for additional precipitation. **Second subplot:** Measured mean snow surface changes and corresponding corrections for additional precipitation. Data from both subplots correspond to both x-axes presented at the bottom. Data values are presented in Tables A.1 & A.2 in Appendix A.

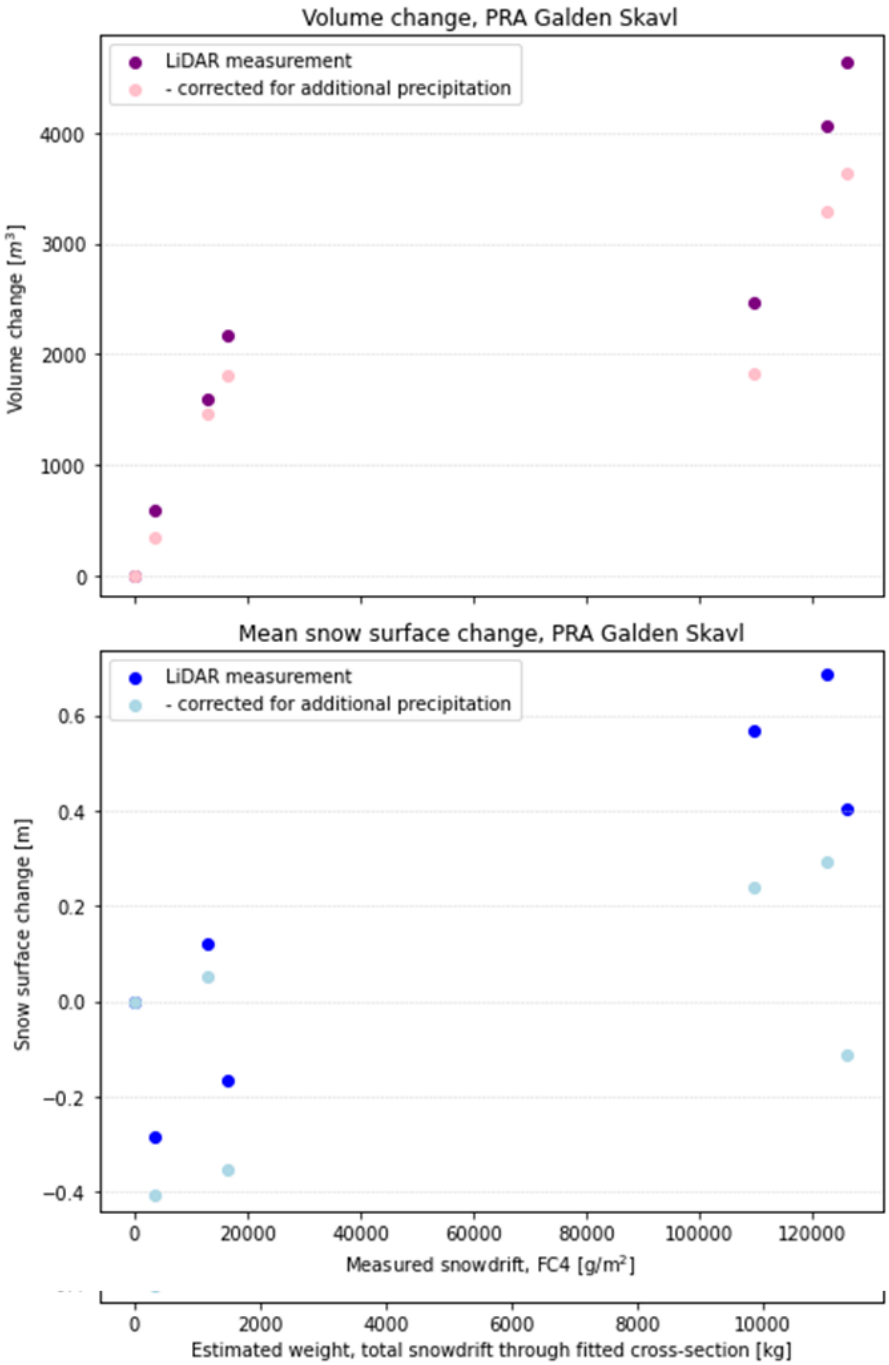

Figure B.6: First subplot: Measured volume changes and corresponding corrections for additional precipitation. **Second subplot:** Measured mean snow surface changes and corresponding corrections for additional precipitation. Data from both subplots correspond to both x-axes presented at the bottom. Data values are presented in Tables A.1 & A.2 in Appendix A.

Appendix C

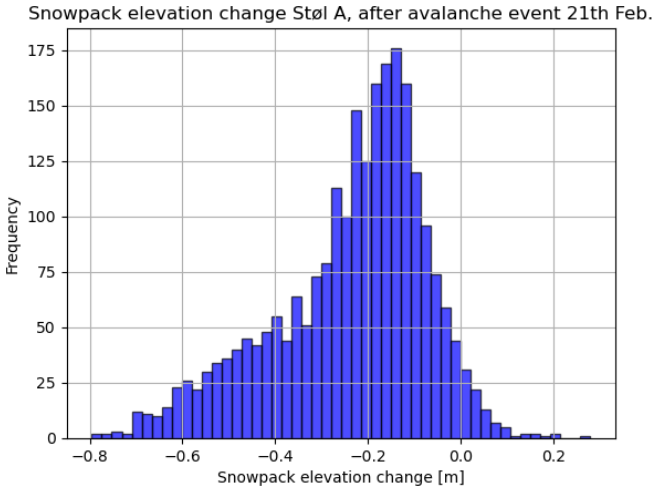

Figure C.1: Snow surface change in the released area at Støl A after avalanche control 21 February. Calculated by delineating and converting LiDAR data to ASCII files (in ArcGIS PRO) to be processed in Python - here, subtraction of values between the two LiDAR-measurements were made.

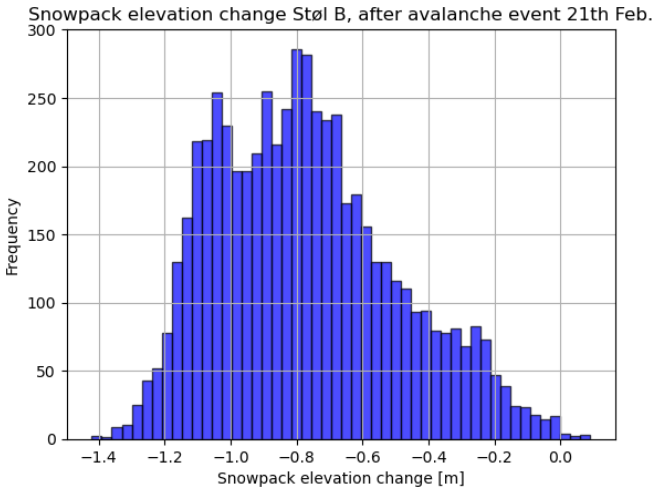

Figure C.2: Snow surface change in the released area at Støl B after avalanche control 21 February. Calculated by delineating and converting LiDAR data to ASCII files (in ArcGIS PRO) to be processed in Python - here, subtraction of values between the two LiDAR-measurements were made.

Appendix D

Table D.1 shows the registered fracture heights from winter seasons 2022-2023 and 2023-2024. The data from late in the winter season 2022-2023 (Period 18.03.22 - 30.04.23) had avalanches releasing on facets, and thus is not included in the table as this study focuses on wind slab problems.

The measured snowdrift data (86 969 g/m^2) prior to avalanche control 31.01.23 has data holes during the storm 29.01.23 - 31.01.23, thus showing a less snowdrift value than reality. Mel D, Støl D, and Tørv B are excluded columns in this presentation as registrations were only zero values. Fracture heights are approximations based on visual assessment from the road.

Table D.1: Registered fracture heights from winter seasons 2022-2023 and 2023-2024. Red cells: Avalanche crossed the road, Underline: Released at the ground. ☐: Released on facets (else: released within wind slabs). Fracture heights are given in meters. The measured snowdrift are cumulative sums within the specified period (exact period between time of last avalanche control and the current one). Data extracted from the Varsom Regobs [2024] platform.

FC4 (g/m2)	Precip. (mm)	Period	Varden	Mel C	Mel B	Mel A	Støl E	Støl C	Støl B	Støl A	Langø	Langø Sør	Skog D	Skøg C	Skog B	Skog A	Tørv F	Tørv E	Tørv D	Tørv C	Tørv A
8812.0	19.0	31.01.23-08.02.23	0.03	0	0	0	0	0	0	0	0.03	0	0	0	0	0	0	0	0	0	0
17705	37.1	28.12.22-10.01.23	0.25	0	0	0	0	0	0	0	0	0	0	0	0	0	0	0	0	0	0
17769	20.2	18.12.23-27.12.23	0.1	0	0	0	0	0.4	0.3	0.5	0.2	0	0	0.1	0.05	0.05	0	0	0	0.1	0
18669	44.8	28.12.22-12.01.23	0	0	0	0	0	0.5 ☐	0	0	0	0.5 ☐	0	0	0	0	0	0	0	0	0
39719	93.3	18.03.22-30.04.23	0.6 ☐	0.8 ☐		0.5 ☐	0	0	1.2 ☐	0.8 ☐	0.6 ☐	0	0	0	0	0	0	0	0	0	0.5 ☐
55363	26.7	27.12.23-23.01.24	0.3	0.5	0	0	0	0	0.5	0	0.3	0	0.2	0.2	0.5		0.5	0.5		0.4	0.5
76849	33.6	21.02.23-18.03.23	0.15	0.5	0.5	0.5	0	0	0	0.2	0.2	0	0.2	0.3	0.1	0.1	0.5	0.5	0.5	0.5	0.5
86969	47.9	12.01.23-31.01.23	0.3	0	0	0	0	0.3	0.2	0	0.3	0	0	0	0	0	0	0	0.2	0	0.2
126127	65.6	13.02.23-21.02.23	0.8	0.2	0	0.4	0	0	0.4	0.2	0.5	0	0.3	0.3	0.2	0.2	0.2	0.2	0.3	0.4	0.8
246348	70.9	23.01.24-05.02.24	0.2	0.2		0.2	1.0	0	2.0	0	0.7	0	0	0	0.1	0.1	0.1	0.5 ☐			0.5
369118	24.9	08.02.23-13.02.23	0.2	0.2	0	0.4 ☐	0	0	0	1.5 ☐	0.1	0	0	0	0	0	0.1	0.2	0.2	0.2	0.1